Thermochemical Modeling of Nonequilibrium Oxygen Flows

by

Kevin Joseph Neitzel

A dissertation submitted in partial fulfillment
of the requirements for the degree of
Doctor of Philosophy
(Aerospace Engineering)
in The University of Michigan
2017

Doctoral Committee:

Professor Iain D. Boyd, Chair
Professor John R. Barker
Associate Professor Krzysztof J. Fidkowski
Associate Professor Mirko Gamba

"Roads? Where we're going, we don't need roads."

-Doc Brown

"It is the mark of an educated mind to be able to entertain a thought without accepting it."

-Aristotle

"No discipline seems pleasant at the time, but painful. Later on, however, it produces a harvest of righteousness and peace for those who have been trained by it."

-Hebrews 12:11

To Infinity And Beyond

TABLE OF CONTENTS

DEDICATION ii

LIST OF FIGURES v

LIST OF ABBREVIATIONS x

ABSTRACT xii

CHAPTER

I. Introduction 1

1.1 Motivation 1
1.2 Scope of Dissertation 8
1.2.1 Overview 8
1.2.2 Outline 9

II. Nonequilibrium Flow Modeling 10

2.1 Nonequilibrium Flow Physics 10
2.2 Nonequilibrium Modeling: Vibrational Representation 20
2.3 Nonequilibrium Modeling: Two-Temperature Approach . . . 20
2.3.1 Background 20
2.3.2 Two-Temperature Model 22
2.4 Nonequilibrium Modeling: State-To-State Approach 30
2.4.1 Background 30
2.4.2 State-to-State Model 31
2.4.3 Modified Two-Temperature Model (2T-NENB) . . . 37
2.5 Flow Modeling 46
2.5.1 Unsteady Flow Solver 47

III. Oxygen-Argon Mixture Shock Tube Studies 52

3.1 Experimental Data 53

3.2 Computational Results and Comparisons 53
3.2.1 Test Case 1 53
3.2.2 Test Case 2 57
3.2.3 Detailed Rate Comparison 62
3.2.4 Detailed State-to-State Rate Comparison 67
3.3 Summary 74

IV. Pure Oxygen Shock Tube Studies 76

4.1 Experimental Data Overview 76
4.2 Results and Comparison 77
4.2.1 Two-Temperature Model 78
4.2.2 State-to-State Model 94
4.2.3 Nonequilibrium Relaxation Influence on the Flow State Variables 96
4.2.4 Reduced Order Model 111
4.3 Summary 115

V. Double-Cone Investigation 117

5.1 LeMANS CFD Flow Solver 117
5.2 State-to-State CFD Modeling 118
5.3 Experimental Setup 119
5.4 Results and Comparison 121
5.5 Summary 128

VI. Summary and Conclusions 129

6.1 Summary 129
6.2 Unique Contributions 131
6.3 Future Work 132

APPENDICES 134

BIBLIOGRAPHY 138

LIST OF FIGURES

Figure

1.1	NASA's Orion capsule: an example of a hypersonic re-entry vehicle	3
1.2	The X-51A: an example of a scramjet-powered, hypersonic cruise vehicle	4
1.3	Nonequilibrium Modeling Capability Study: Solid Line - Model, Dots - Experimental Data	5
1.4	Shock Tube Flow Description	7
2.1	Primary Energy Modes for a Generic Molecule (Translational, Rotational, Vibrational, and Electronic)	11
2.2	Post Normal Shock Translational Temperature for Various Mach Numbers (Altitude of 150,000 feet)	14
2.3	Notional Energy Potential and Vibrational Energy Levels	15
2.4	Vibrational Energy States: Dunham and Varandas	17
2.5	Cumulative Vibrational Population for Several Temperatures	18
2.6	Cumulative Vibrational Energy for Several Temperatures	19
2.7	Vibrational relaxation parameter obtained from various models	26
2.8	C_{VD} Data and Curve Fits for Oxygen Systems	29
2.9	O-Ar Potential Energy Surface for QCT Analysis	35
2.10	O-O Potential Energy Surface for QCT Analysis	35
2.11	Electronically Excited Oxygen Population Evaluation	36

2.12 O_2-O Total Dissociation Rate for Combinations of Translational and Vibrational Temperatures (Boltzmann) 39

2.13 O_2-O Total Dissociation Rate from QCT Analysis and Park Nonequilibrium Model 40

2.14 O_2-O Total Dissociation Rate from QCT Analysis and Presented Nonequilibrium Model 42

2.15 Vibrational population distribution evolution, sample 43

2.16 Vibrational state population evolution, sample 44

2.17 Total Dissociation Rate from QCT Analysis for an Overpopulated Boltzmann Distribution 45

2.18 Total Dissociation Rate from QCT Analysis for an Underpopulated Boltzmann Distribution 46

2.19 Unsteady Solver Grid Setup 47

2.20 Pressure Contours for Shock Tube Flow: Argon 48

2.21 Comparison between Unsteady Simulation and Analytical Solution . 49

2.22 Pressure Contours for Shock Reflection at Shock Tube End Wall . . 49

2.23 Post Reflected Shock Temperature Near End Wall 50

2.24 Flow Solver Comparison: Run 109 51

3.1 Temperature profiles obtained with different relaxation models for Test Case 1: T1=298K, P1=7.125 torr, Ms=3.57 (incident shock) . 55

3.2 Comparison of normalized vibrational distributions for Test Case 1 . 56

3.3 Temperature profiles obtained with different relaxation models for Test Case 2: T1=295K, P1=1.0 torr, Ms=5.9 (incident shock) . . . 58

3.4 Oxygen mole-fraction profiles obtained with different relaxation models for Test Case 2: T1=295K, P1=1.0 torr, Ms=5.9 (incident shock) 59

3.5 Vibrational population distribution comparison for Test Case 2 (FHO) 60

3.6 Vibrational population distribution comparison for Test Case 2 (QCT) 61

3.7 Vibrational relaxation parameter as a function of temperature . . . 63

3.8 Profiles of vibrational temperature for Test Case 2 in the absence of chemistry 65

3.9 Rates of vibrational energy lost through dissociation (Test Case 2) . 66

3.10 QSS dissociation rate as a function of temperature for O_2-Ar with experimental data sets 67

3.11 Net STS rate comparison at 5,000K for O_2-Ar: v = 0-30 69

3.12 Net STS rate comparison at 5,000K for O_2-Ar: v = 0-10 70

3.13 Net STS rate comparison at 10,000K for O_2-Ar: v = 0-30 71

3.14 Net STS rate comparison at 10,000K for O_2-Ar: v = 0-10 72

3.15 Macroscale time to equilibrium sensitivity due to a STS rate perturbation of 50% for O_2-Ar 73

4.1 Temperature profiles, C1 case 79

4.2 Composition profiles, C1 case 79

4.3 Temperature profiles, C2 case 80

4.4 Composition profiles, C2 case 81

4.5 Temperature profiles, C3 case 82

4.6 Composition profiles, C3 case 83

4.7 Temperature-dependent C_{VD} Influence: Case C1 84

4.8 Temperature-dependent C_{VD} Influence: Case C2 85

4.9 Temperature-dependent C_{VD} Influence: Case C3 86

4.10 Temperature profiles, C1 case 88

4.11 Composition profile, C1 case 89

4.12 Temperature profiles, C2 case 90
4.13 Composition profile, C2 case 91
4.14 Temperature profiles, C3 case 92
4.15 Composition profile, C3 case 93
4.16 Temperature profiles evaluating the effect of α, C1 case 95
4.17 Temperature profiles evaluating the effect of α, C2 case 95
4.18 Temperature profiles evaluating the effect of α, C3 case 96
4.19 Pressure profile during post normal shock relaxation, C1 case 97
4.20 Velocity profile during post normal shock relaxation, C1 case 98
4.21 Density profile during post normal shock relaxation, C1 case 98
4.22 Pressure profile during post normal shock relaxation, C2 case 99
4.23 Velocity profile during post normal shock relaxation, C2 case 99
4.24 Density profile during post normal shock relaxation, C2 case 100
4.25 Pressure profile during post normal shock relaxation, C3 case 100
4.26 Velocity profile during post normal shock relaxation, C3 case 101
4.27 Density profile during post normal shock relaxation, C3 case 101
4.28 Temperature profiles, C1 case 103
4.29 Composition profile, C1 case 103
4.30 Vibrational population distribution evolution, C1 case 105
4.31 Vibrational state population evolution, C1 case 105
4.32 Temperature profiles, C2 case 106
4.33 Composition profile, C2 case 107
4.34 Vibrational population distribution evolution, C2 case 107

4.35 Vibrational state population evolution, C2 case 108
4.36 Temperature profiles, C3 case 109
4.37 Composition profile, C3 case 109
4.38 Vibrational population distribution evolution, C3 case 110
4.39 Vibrational state population evolution, C3 case 110
4.40 Temperature profiles, C1 case 112
4.41 Composition profile, C1 case 112
4.42 Temperature profiles, C2 case 113
4.43 Composition profile, C2 case 114
4.44 Temperature profiles, C3 case 114
4.45 Composition profile, C3 case 115
5.1 Double-cone data points 120
5.2 Double-cone dimensions 121
5.3 CFD Grid: 250,000 cells 122
5.4 Pressure contour plot for nominal conditions 123
5.5 Translational temperature contour plot for nominal conditions . . . 124
5.6 Vibrational Temperature contour plot for nominal conditions . . . 125
5.7 Pressure distribution on double cone body 126
5.8 Heat transfer distribution on double cone body 127

LIST OF ABBREVIATIONS

2T Two-Temperature

CFD Computational Fluid Dynamics

FHO Forced Harmonic Oscillator

HH Hulbert-Hirshfelder

MW Millikan-White

NENB Nonequilibrium, Non-Boltzmann

PES Potential Energy Surface

QCT Quasi-Classical Trajectory

ROM Reduced Order Model

SSH Schwartz, Slawsky, and Herzfeld

STS State-To-State

TPS Thermal Protection System

- -

A,B Millikan-White Relaxation Equation Coefficients

C_{VD} Vibrational-Dissociation Coupling Coefficient

c Mean Particle Velocity

d Gas Particle Diameter

e_i Specific Energy for "i" Mode

E_i Energy for "i" Mode

h Specific Enthalpy

k Boltzmann Constant

k_D Dissociation Rate Coefficient

k_{VD} Bound-Bound Rate Coefficient

Kn Knudsen Number

L Characteristic Vehicle Length

M Generic Gas Particle

n Number Density

N Population

p Pressure

Q Partition Function

r Internuclear Separation

T **or** T_t Translational Temperature

T_a Average Temperature

T_v Vibrational Temperature

u Bulk Flow Velocity

v Vibrational State

V Potential Energy

ABSTRACT

Thermochemical Modeling of Nonequilibrium Oxygen Flows

by

Kevin Neitzel

Chair: Iain D. Boyd

The development of hypersonic vehicles leans heavily on computational simulation due to the high enthalpy flow conditions that are expensive and technically challenging to replicate experimentally. The accuracy of the nonequilibrium modeling in the computer simulations dictates the design margin that is required for the thermal protection system and flight dynamics. Previous hypersonic vehicles, such as Apollo and the Space Shuttle, were primarily concerned with re-entry TPS design. The strong flow conditions of re-entry, involving Mach numbers of 25, quickly dissociate the oxygen molecules in air. Sustained flight, hypersonic vehicles will be designed to operate in Mach number ranges of 5 to 10. The oxygen molecules will not quickly dissociate and will play an important role in the flow field behavior. The development of nonequilibrium models of oxygen is crucial for limiting modeling uncertainty.

Thermochemical nonequilibrium modeling is investigated for oxygen flows. Specifically, the vibrational relaxation and dissociation behavior that dominate the nonequilibrium physics in this flight regime are studied in detail. The widely used two-temperature (2T) approach is compared to the higher fidelity and more computation-

ally expensive state-to-state (STS) approach. This dissertation utilizes a wide range of rate sources, including newly available STS rates, to conduct a comprehensive study of modeling approaches for hypersonic nonequilibrium thermochemical modeling. Additionally, the physical accuracy of the computational methods are assessed by comparing the numerical results with available experimental data.

The numerical results and experimental measurements present strong nonequilibrium, and even non-Boltzmann behavior in the vibrational energy mode for the sustained hypersonic flight regime. The STS approach is able to better capture the behavior observed in the experimental data, especially for stronger nonequilibrium conditions. Additionally, a reduced order model (ROM) modification to the 2T model is developed to improve the capability of the 2T approach framework.

CHAPTER I

Introduction

1.1 Motivation

The development of hypersonic vehicles presents some unique challenges in terms of system design. Knowledge of the flow field and vehicle surface properties is needed to adequately develop the thermal protection system (TPS) and control system. Due to the high enthalpy flow experienced by a hypersonic vehicle, experimental investigation is expensive and technically challenging. This leads to a strong reliance on computational modeling for design development. The flight conditions and geometry do not always allow adequate time or distance for the flow to reach equilibrium before interacting with the vehicle. The chemistry and flow properties affecting the vehicle are governed by finite rate processes, and thus, nonequilibrium modeling is especially important. Computational modeling uncertainty has a large effect on the design process. Appropriate design margins are required in order to compensate for the modeling uncertainty.

Previous hypersonic vehicles, such as Apollo and the Space Shuttle, were primarily concerned with re-entry TPS design, see Figure 1.1 for a re-entry vehicle example. The strong flow conditions of re-entry into the Earths atmosphere, involving Mach numbers of 25, quickly dissociate the oxygen (O_2) molecules in air. Consequently, the re-entry modeling primarily focused on the behavior of molecular and atomic nitrogen.

The high velocities associated with re-entry lead to other thermodynamic phenomena to be relevant, such as radiation. A number of successful re-entry programs have demonstrated that the modeling capability at these strong flow conditions can capture the physics adequately enough for vehicle design.

The primary direction of hypersonic research has shifted recently. Sustained hypersonic flight vehicles are motivated by the push for faster passenger travel and for defense applications. Current and future cruise and boost-glide hypersonic vehicles designed to operate in Mach number ranges of 5 to 10 are subjected to sustained flight conditions that are milder than re-entry, see Figure 1.2 for an example flight vehicle. For this flight regime, the O_2 molecules will not quickly dissociate and will play a large role in the flow field behavior. In addition, atomic oxygen is highly reactive with vehicle surface materials. The development of nonequilibrium models of O_2 and its interactions with the other air species is crucial for limiting modeling uncertainty. The work presented in this thesis will focus specifically on the oxygen flow compositions.

The importance of hypersonic computer modeling is highlighted by recent experimental test programs. DARPA's HTV-2 project was driven by the goal to provide the United States the capability to reach any target in the world within an hour using an unmanned hypersonic vehicle. This goal necessitates a flight speed in the hypersonic regime. During a demonstration flight in 2011, the HTV-2 was able to maintain flight for about three minutes before it was prematurely plunged into the Pacific Ocean by its safety system. An investigation revealed that the vehicle skin peeled due to loads/stresses higher than predicted caused the termination of the flight. The outcome of this demonstration flight highlights the need for improved understanding and modeling capability for sustained flight hypersonic vehicle design.

Sustained hypersonic flight vehicles fly in a regime in which nonequilibrium is important. The characteristic flow time falls in the range near the vibrational relaxation

Figure 1.1: NASA's Orion capsule: an example of a hypersonic re-entry vehicle

time. As a consequence, the vibrational mode is in nonequilibrium around the flight vehicle. Depending on the details of freestream conditions and the vehicle size, the rotational energy mode can be in slight nonequilibrium as well. Additionally, the flight speeds in the hypersonic regime lead to high enough post shock translational temperatures, that molecular dissociation is prevalent in the flow field. The presented work will focus on the vibrational energy mode and chemistry.

The accuracy of the physics modeling dictates the design margin that is required for the thermal protection system. Modeling this nonequilibrium thermochemistry is one of the main sources of simulation uncertainty. Recent advances in computational chemistry methods has made it possible to investigate the use of high fidelity modeling for hypersonic vehicle analysis.

A study was performed in 2010 by Holden et al [1] to review the state of the art modeling capability against experimental data. The flow over a double-cone geometry

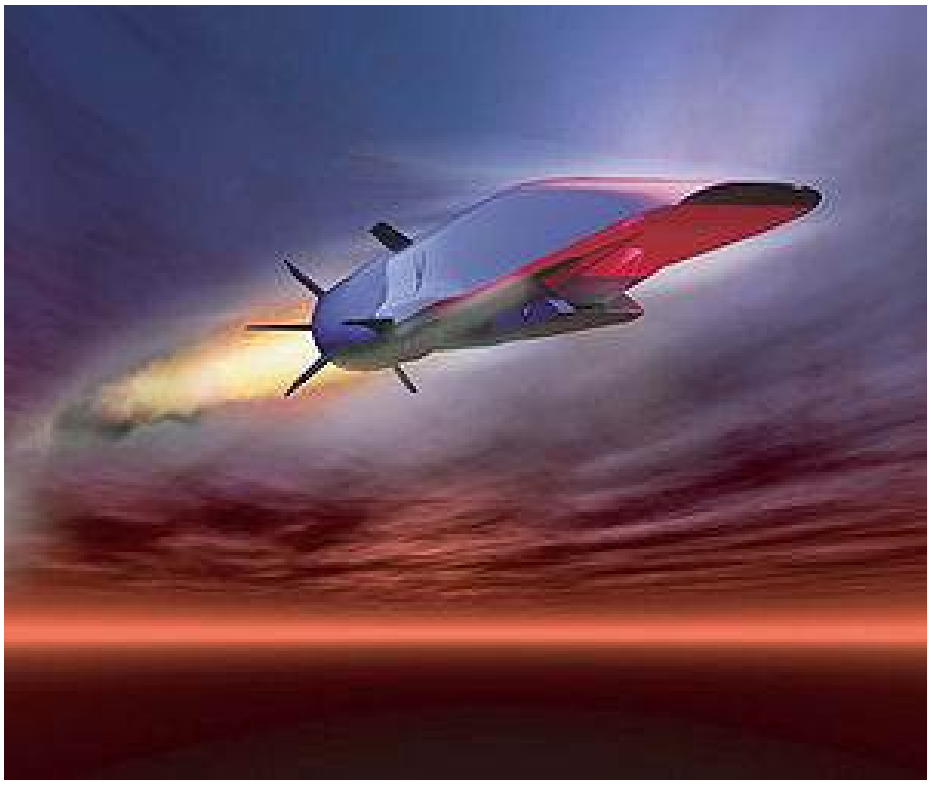

Figure 1.2: The X-51A: an example of a scramjet-powered, hypersonic cruise vehicle

was utilized. The state of the art, two-temperature model was used to model the thermochemical nonequilibrium behavior. The results highlight the need for a better understanding of nonequilibrium flows containing oxygen. Figure 1.3 presents the results for two different Mach numbers as the surface quantities, pressure and heat transfer.

The results show that as the Mach number increases, and nonequilibrium is stronger, the model predict deviates further from the experimental data.

The two-temperature model is the widely used approach for hypersonic vehicle analysis[2]. For vibrational relaxation, the approach relies on a relaxation time that is a function of temperature and pressure to solve the Landau-Teller equation for vibrational energy. The Millikan-White (MW) formula for vibrational relaxation time is generally used, and correlates well with experimental data for many molecular systems [3]. One of the exceptions is the O_2–O system that does not correlate well

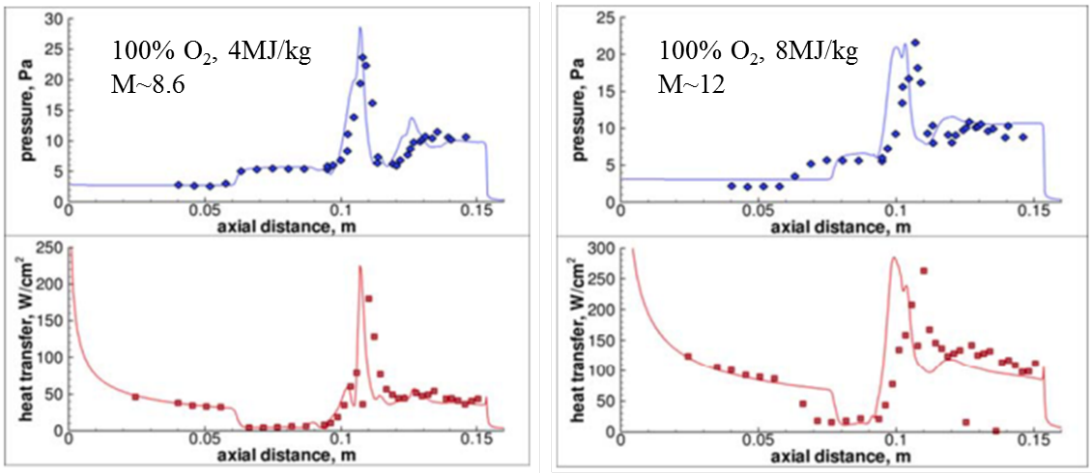

Figure 1.3: Nonequilibrium Modeling Capability Study: Solid Line - Model, Dots - Experimental Data

with experimental data[4, 5]. The O_2-O system violates many of the assumptions that are present in the underlying Landau-Teller theory that dictates the temperature dependence of the Millikan-White formula. Park and others have adjusted the Millikan-White coefficients for O_2-O to correlate better with experimental data[6]. However, the previous work has still assumed the temperature dependence dictated by the Landau-Teller theory. The vibrational relaxation of O_2-O is studied in this work using recently developed rates from a detailed quasi-classical trajectory (QCT) analysis[7]. The vibrational relaxation times obtained using the extensive quasi-classical trajectory analysis coupled to the set of master equations indicated that relaxation is the most effective at low temperatures, which is opposite to the temperature dependence assumed in the MW equation. Also in the two-temperature model, chemistry is captured by reaction rates that use Arrhenius-type rate coefficients. Additionally, the Arrhenius form uses the geometrically averaged temperature of the translational and vibrational temperature ($T_a = \sqrt{T_t T_v}$) in order to capture nonequilibrium, thermochemical coupling.

The state-to-state (STS) approach is a higher-fidelity model for describing the nonequilibrium energy transfer that has been used sparingly for decades, but has be-

come more popular recently due to advances in computational power [8, 9, 10, 11, 12, 13, 14, 15, 16]. The STS model is computationally expensive since it directly simulates the population of each vibrational state. These populations are governed by the system of master equations that employ state-specific rates obtained by quasi-classical trajectory (QCT) simulations or simpler models [17]. This approach allows for multi-quantum transitions and non-Boltzmann distributions to be captured [11, 18, 8]. There are three widely used methods for deriving the required transition rate coefficients: the Schwartz, Slawsky, and Herzfeld (SSH) theory based on first-order perturbation, the forced harmonic oscillator (FHO) model of Adamovich [17] and the QCT analysis[19]. The presented work will focus on the FHO and QCT methods. The SSH model is more restrictive in its methodology than the FHO method, but is the same computational cost. The FHO model is a semi-classical analytical method that was developed from nonperturbative analytic theory assuming that the interaction of target and projectile particles is governed by a strong repulsive potential. The closed form of the FHO rate coefficients makes it very attractive due to the low computational expense required to generate transition rates. However, the assumptions including the form of the potential energy surface (PES) puts a limitation on the systems that are described well by the FHO methodology. Even though the FHO approach is widely used for all systems, the FHO model is not formally applicable for molecular systems that have open-shell atoms and molecules, such as for the O_2-O collisions. The QCT method is a more general approach and the transition rates can be obtained for any PES. The QCT method employs Monte-Carlo methods of statistical sampling of kinetic and internal energy of particles to accumulate a large-scale database of transition event probabilities. The QCT method is computationally expensive, but the recent increase in computational power has made it tractable for atom-diatom interactions.

STS rates allow for detailed information about the vibrational-translational en-

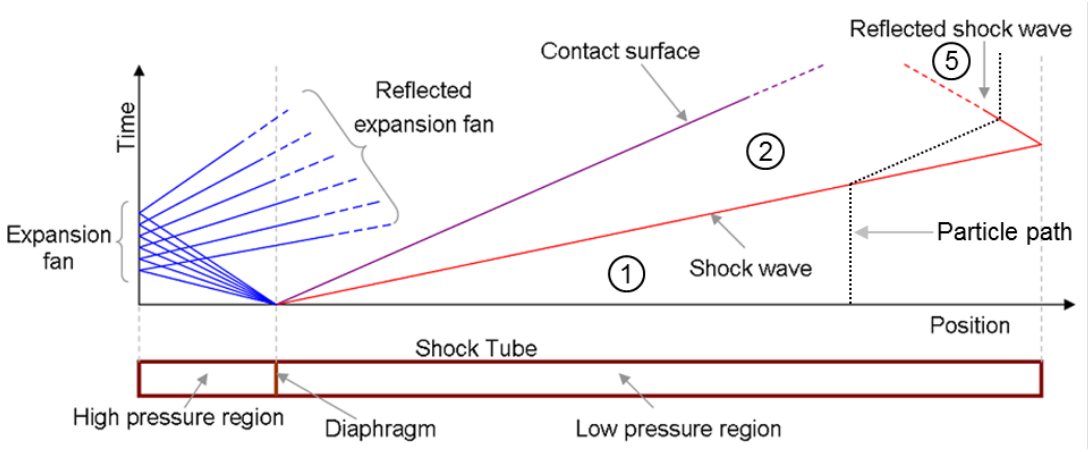

Figure 1.4: Shock Tube Flow Description

ergy transfer and dissociation. Specifically, an evaluation can be made for arbitrary combinations of translational temperature and vibrational temperatures or population distributions. This detailed understanding from high fidelity STS rates allows for a reduced order model to be developed. It is desired to retain the framework of the 2T model due to its widespread use. The presented work will develop a modified version of the 2T model named the 2T-NENB (nonequilibrium, non-Boltzmann) model. The goal is to have a 2T-type model that is able to provide results that closely mimic the full STS analysis. This is extremely advantageous for multi-dimensional, hypersonic vehicle design work that can not currently handle the computational expense of full STS analysis.

The shock tube is a popular experimental setup for studying hypersonic flow conditions. A high pressure region is separated from a low pressure region by a diaphragm. The diaphram is then ruptured (on its own or broken intentionally). This sends an incident shock wave through the low pressure region, and then reflects off the end wall of the shock tube. The simple setup allows for hypersonic flow conditions to be created through an incident and reflected shock. The gas that the two shocks go through can be high enthalpy and useful for studying nonequilibrium behavior. Figure 1.4 presents the setup of a shock tube.

In addition to shock tube flow comparisons, experimental data from CUBRC[42] (shock tunnel facility) will be used for evaluation of the nonequilibrium models for hypersonic flow over a double-cone configuration. This experimental data set only contains surface data so it will be a good evaluation of a hypersonic vehicle design scenario.

1.2 Scope of Dissertation

1.2.1 Overview

The purpose of this dissertation is to examine the thermochemical nonequilibrium modeling methodologies for hypersonic flow conditions containing oxygen. The nonequilibrium behavior of oxygen in hypersonic, sustained flight conditions has not been well investigated and has a significant effect on the flow field around the vehicle. The vibrational-translational energy transfer and dissociation will be the primary focus of the work. Numerical results for low fidelity (2T model) and high fidelity (STS model) modeling approaches will be compared to experimental measurements. The post normal shock thermal relaxation and chemistry is measured experimentally in shock tubes. Recent advances in computing resources and newly available STS rates from QCT analysis allow highly accurate and computational expensive analyses to be run. These high fidelity results will be utilized in two ways. First, they will allow modeling guidelines to be established. The results will highlight the flow conditions that require high fidelity modeling for an accurate simulation, and the flow conditions that allow the lower fidelity modeling to be used in order to reduce computational cost. Second, the high fidelity modeling will guide the development of a modification to the low fidelity modeling. The goal is to present an alternative to the computationally expensive STS modeling that is able to accurately capture the nonequilibrium behavior.

1.2.2 Outline

Chapter II provides a comprehensive overview of nonequilibrium flow physics. Specifically, the vibrational-translational energy transfer and dissociation are discussed in detail. The chapter presents the details for numerical modeling of the vibrational energy mode and dissociation. Two prominent models are described and implemented for modeling vibrational and dissociation nonequilibrium. Next, the rates required for nonequilibrium modeling are presented. There are various potential sources for the rate, so each source is described in detail.

Chapters III and IV present an investigation of the modeling approaches, as well as a comparison to post normal shock, shock tube experimental measurements. First, a highly diluted O_2-Ar composition is investigated. Next, a set of pure oxygen simulations and experiments are studied. The chapter provides a description of the experimental approach for both setups. The chapter than compares the results for the various modeling approaches and experimental measurements. The chapter concludes with a summary of the investigation and some intermediate conclusions.

Chapter V describes the extension of nonequilibrium modeling to the 3D, finite volume CFD solver, LeMANS. The chapter focuses on the STS modeling implementation. The chapter concludes with a numerical and experimental investigation of hypersonic flow over a double-cone geometry in an expansion tunnel. The chapter starts with a description of the experimental setup before investigating the results and measurements. The chapter finishes with some intermediate conclusions.

The dissertation concludes with Chapter VI. First, the chapter summarizes the work presented in this dissertation and provides conclusions. Finally, the chapter provides a description of the unique contributions of the presented work and the future work that would extend from this dissertation.

CHAPTER II

Nonequilibrium Flow Modeling

This chapter presents the complete details about the nonequilibrium flow modeling used in this dissertation. The chapter starts by presenting the underlying physics involved with hypersonic flow and nonequilibrium behavior. Next, the various aspects of the nonequilibrium modeling approaches, specifically, the formulation and source of rate data, are discussed.

2.1 Nonequilibrium Flow Physics

A gas is comprised of many atoms and molecules (referred to as gas particles as a general term) that are constantly moving around and colliding with each other. Collisions are the mechanism by which the state of a gas changes within a flow and interacts with the surface of a vehicle. These individual collisions govern how the flow at the macroscale level behaves, specifically, acceleration/deceleration, heating/cooling, and chemical reactions as examples. Due to the high freestream energy and conditions, hypersonic, nonequilibrium flow modeling is primarily concerned with capturing how energy is transferred between the different energy modes of the gas particles. The collisional nature of the flow physics makes it important to understand the time and length scales involved in the collisions, flow, and vehicle geometry.

The mean-free-time (τ_C) is a parameter that quantifies the average time between

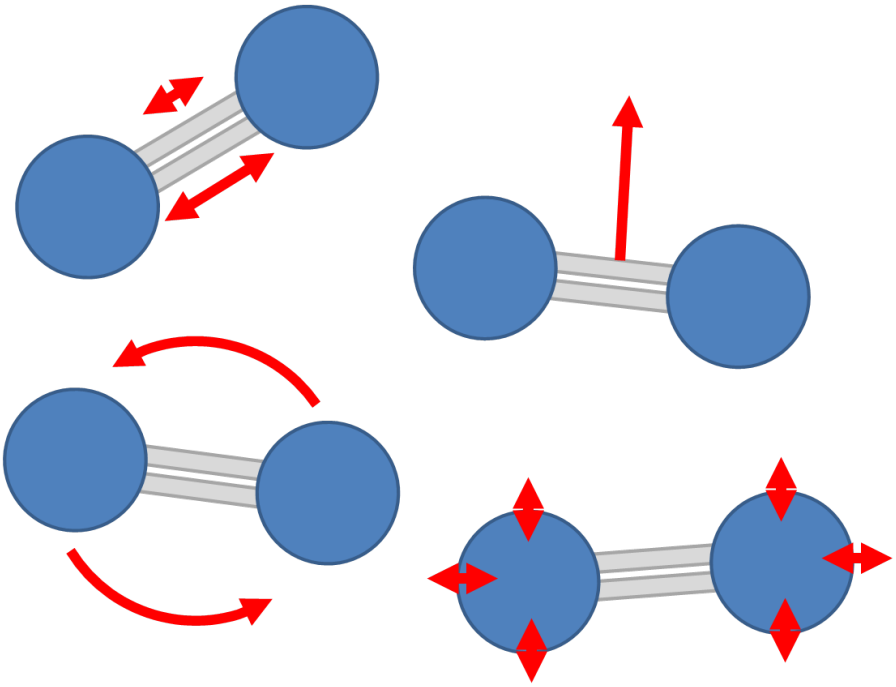

Figure 2.1: Primary Energy Modes for a Generic Molecule (Translational, Rotational, Vibrational, and Electronic)

particle collisions in a flow. Additionally, there are characteristic time scales associated with the various energy modes for the gas particles. The atoms contain translational energy and electronic energy, while the molecules contain translational, rotational, vibrational, and electronic energy. The rotational, vibrational, and electrical energy modes are collectively described as internal energy modes. All of these energy modes can become important for high speed flight or re-entry. Figure 2.1 shows the energy modes.

It is important to understand how these various time scales compare to each other. In a typical flow, the time scales compare as shown in Equation 2.1.

$$\tau_c \simeq \tau_{trans} < \tau_{rot} < \tau_{vib} < \tau_{chem} \tag{2.1}$$

Hypersonic flows have very high speed freestream conditions for the gas particles. These high speed gas particles are slowed down because of the flight vehicle through

a shock wave. The shock wave is a very thin region where only a few collisions are required for the high speed freestream particles to convert this uniform bulk flow, translational energy into random, thermal translational energy with a slower bulk flow velocity. This process corresponds to the notion that the characteristic time of the flow (shock) and translational energy are very similar ($\tau_c \simeq \tau_{trans}$), since it only takes a few collisions to convert the translational energy. The number of collisions needed to change and characteristic time scales are related. As a reference, for this case of thermal energy increase, it takes approximately 10 collisions to increase the rotational energy to uniformity and approximately 1000 collisions to increase the vibrational energy to uniformity [20].

Additionally, it is important to evaluate the characteristic flow time (τ_{flow}). This characteristic flow time corresponds to the time it takes for spatial changes in the flow properties around the flight vehicle. These spatial changes in flow properties are related to the flow property gradients in the flow field. The degree of nonequilibrium can be evaluated by comparing τ_{flow} with the other time scales, specifically, the τ_{flow} is faster than the energy mode time scales. Another common, high level approach to understanding the degree of nonequilibrium is to look at the length scales. Specifically, the Knudsen number is the ratio of the mean-free-path (λ) and characteristic length of the vehicle, which is defined as the average distance between particle collisions. The Knudsen number is a useful macroscopic parameter to understand the regime that the flight vehicle is flying in.

$$Kn = \frac{\lambda}{L}, \qquad \lambda = \frac{1}{\sqrt{2}\pi d^2}\frac{1}{n} = \frac{1}{\sqrt{2}\pi d^2}\frac{kT}{p} \tag{2.2}$$

Nonequilibrium modeling is critical in the transition regime between the regime in which so many collisions occur that the flow is always in equilibrium ($Kn << 1$) and the regime in which there are no collisions for energy transfer ($Kn >> 1$). The regime of interest in nonequilibrium modeling is when $Kn \sim 1$.

The presented work is primarily interested in sustained hypersonic flight vehicles. The operational conditions of these vehicles are particularly interesting due to nonequilibrium behavior for two reasons. First, the characteristic flow time is on the order of the characteristic time of the vibrational energy mode. This means that the vibrational mode is the primary energy mode that experiences strong nonequilibrium behavior. Second, the flight conditions are more mild than the well studied re-entry flows. The milder flight conditions differ from the re-entry flows largely in how the oxygen in the flow behaves. The molecular oxygen in a re-entry flow quickly dissociates from the high temperature conditions after the strong bow shock. This leaves molecular nitrogen as the only species that undergoes vibrational relaxation behavior. The milder thermal conditions (12,000K and less) associated with sustained hypersonic flight allow significant molecular oxygen to be present in the flow field around the vehicle. The differences in post normal shock translational temperature can be seen in Figure 2.2. As mentioned, re-entry vehicles will be traveling in the Mach 20-25 range, while sustained hypersonic flight vehicles will travel in the Mach 5-10 range. This fundamental difference drives the focus on oxygen vibrational nonequilibrium behavior in this dissertation. The presented work will focus on the vibrational energy mode and chemistry.

Before focusing in on the vibrational mode, the other relevant energy modes are discussed briefly. The hypersonic regime of interest corresponds to a temperature range around 3,000K - 12,000K. The translational and rotational energy modes are considered fully activated at these temperatures and the energy level spacing is sufficiently small to treat the energy levels as a continuum. Moreover, the translational and rotational thermodynamic specific internal energy scales linearly with temperature as shown in Equations 2.3 and 2.4.

$$e_t = \frac{3}{2}RT \tag{2.3}$$

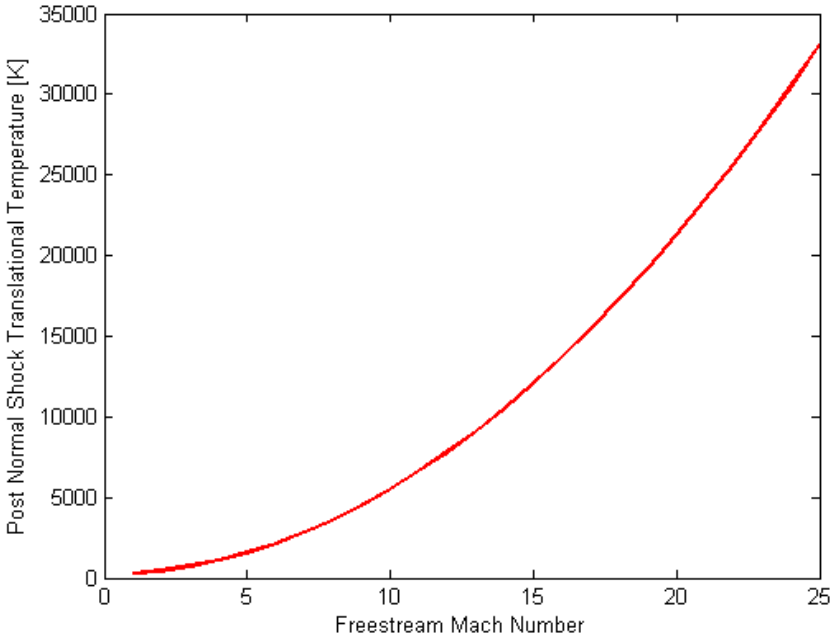

Figure 2.2: Post Normal Shock Translational Temperature for Various Mach Numbers (Altitude of 150,000 feet)

$$e_r = RT \tag{2.4}$$

The electronic energy mode is primarily frozen, but starts to become activated in the temperature range of interest. The electronic characteristic temperature for the first electronically excited state for O_2 is 11,390K[20]. The mode starts becoming activated when the temperature reaches the characteristic temperature and beyond. As a reference, the rotational characteristic temperature is 2.1K and the vibrational characteristic temperature is 2,270K [20].

The vibrational energy mode is fundamentally available due to the interaction of the two atoms within the molecular structure. Energy is stored in the oscillation (or vibration) of the atoms along the line of connection. The interaction is governed by the potential between the atoms. Figure 2.3 shows the notional potential energy as a function of the internuclear distance. The figure also shows two representations of

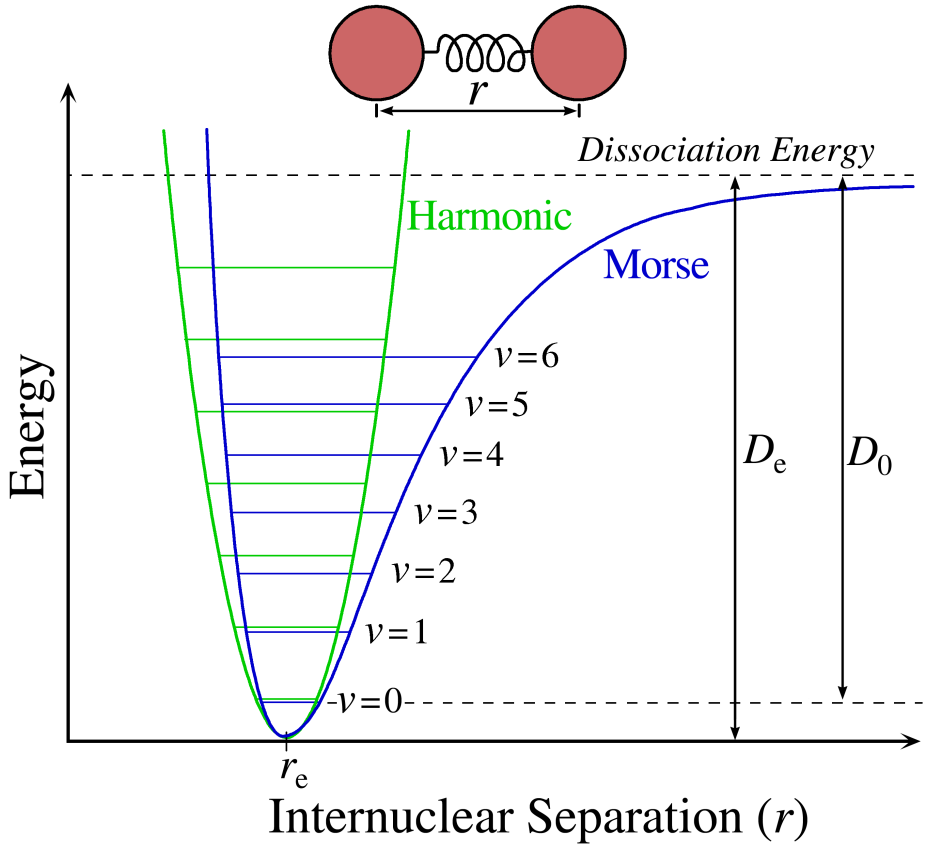

Figure 2.3: Notional Energy Potential and Vibrational Energy Levels

the potential.

The most basic vibrational representation of a molecule is the harmonic oscillator (shown in green). From quantum mechanics, the harmonic oscillator assumption leads to equally spaced, permissible vibrational energy states:

$$\epsilon_v = \left(v + \frac{1}{2}\right) h\nu \tag{2.5}$$

where h is Planck's constant and ν is the harmonic oscillator frequency. The harmonic oscillator is a good approximation for gaining understanding about vibrational behavior due to the relatively simple relations that follow from the assumption. However, the atom interaction does not have a perfectly harmonic oscillator behavior and a more detailed representation is required for precise modeling. Figure 2.3 shows an

example of the Morse potential that captures the more realistic anharmonic behavior. Accounting for a more realistic potential leads to non-equal spacing of the vibrational energy states.

A popular model for the vibrational energy states is known as the Dunham expansion. Specifically, the first two terms are generally retained to represent the vibrational energy states (see Equation 2.6). The equation form clearly shows the harmonic and anharmonic effects being accounted for. More terms in the expansion can be retained, but these first two terms are the widely used terms. The Dunham expansion coefficients for oxygen are $\omega_e = 1580\ cm^{-1}$ and $\omega_e x_e = 12\ cm^{-1}$[17].

The relative magnitudes of these coefficients allude to how well the harmonic oscillator assumption captures the true behavior of the vibrational behavior. The anharmonic, $\omega_e x_e$ coefficient is much smaller than the leading, harmonic coefficient. This suggests that the harmonic term will dominate at the low vibrational states. However, at the higher vibrational states, the anharmonic term will become more and more important. The $O_2 - Ar$ STS work will utilize the Dunham expansion for vibrational energy states.

$$\epsilon_v = \omega_e \left(v + \frac{1}{2} \right) - \omega_e x_e \left(v + \frac{1}{2} \right)^2 \tag{2.6}$$

Vibrational energy states can also be deduced from any potential energy surface (PES). The STS work for the $O_2 - O_2$ and $O_2 - O$ investigations will use the vibrational energy states from the Varandas PES. For comparison, the Dunham expansion has a maximum vibrational state of v = 36, while for the PES of Varandas, it is v = 46. Figure 2.4 shows the comparison of the energy states. Additionally, the vibrational energy levels are presented in Appendix A. The states are very similar up to approximately v = 30 and then there is strong deviation. The Varandas PES contains many more vibrational states near the dissociation energy level. It should be noted that the Dunham expansion only retains two terms. Future work could investigate

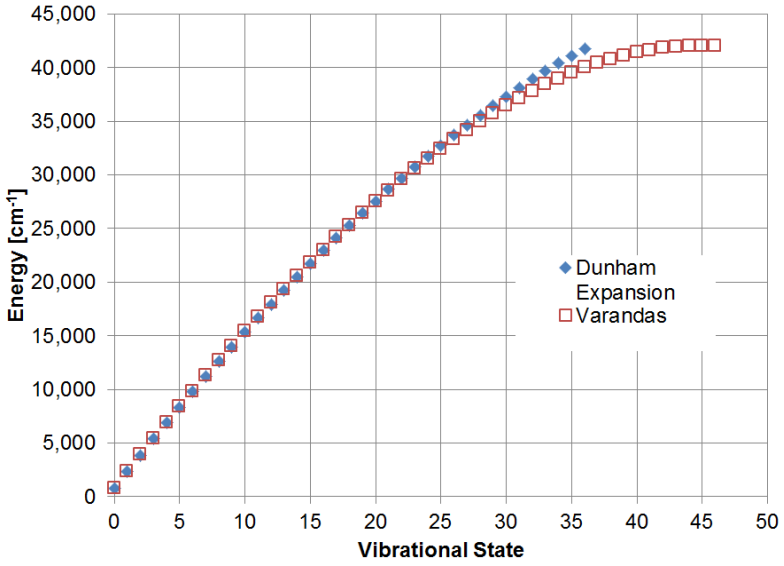

Figure 2.4: Vibrational Energy States: Dunham and Varandas

including additional terms to perhaps capture the high state behavior.

The population of the vibrational energy states is important for properly capturing the vibrational behavior. In general, the molecular population can be spread across the energy levels in any arbitrary fashion. However, it is important to understand the equilibrium distribution associated with the vibrational energy mode. The Boltzmann distribution describes the populations as a function of the vibrational state and energy (v,ϵ_v), temperature (T), and Boltzmann constant (k). It is conveniently written in terms of the discrete partition function (Q) that accounts for the ensemble of energy states. The Boltzmann distribution can be calculated using Equations 2.7 through 2.9 where N_v is the population of molecules at vibrational energy state, v, and N is the total population of molecules.

$$q_v\left(v\right) = e^{-\frac{\epsilon_v}{kT}} \tag{2.7}$$

$$Q_v = \sum_v q_v\left(v\right) \tag{2.8}$$

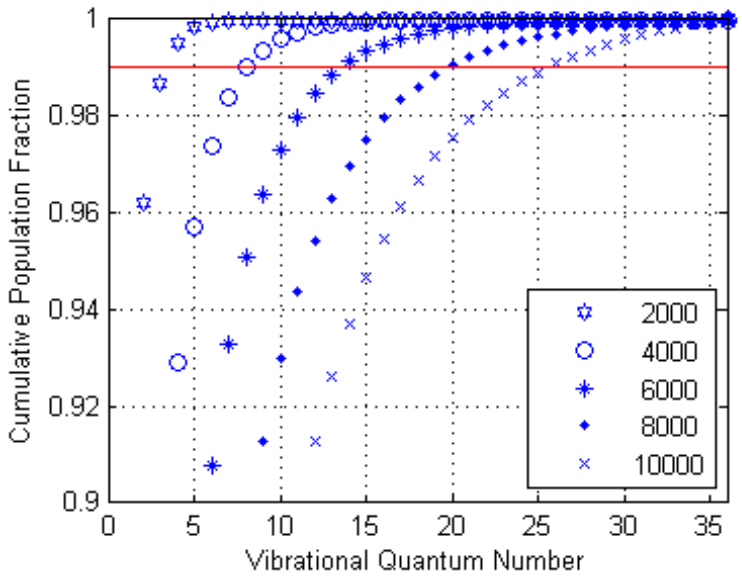

Figure 2.5: Cumulative Vibrational Population for Several Temperatures

$$\frac{N_v}{N} = \frac{q_v\left(v\right)}{Q_v} \tag{2.9}$$

The 2T model only has the single T_V parameter to describe the vibrational mode so an assumption is implied in the formulation. Specifically, the Boltzmann distribution is assumed. The impact of this assumption is evaluated later in the dissertation by comparing the calculated vibrational population distributions with the STS method and comparing them with the Boltzmann distribution.

The vibrational energy levels from the Dunham expansion and the Boltzmann distribution allow one to evaluate the population fractions for each vibrational state and associated energy. Figures 2.5 and 2.6 present the accumulated population fraction and energy fraction for a number of different values of temperature. In another sense, the figures show how many vibrational states need to be accounted for to account for a certain fraction of the total value. For example, a red line is placed at the 99% value. As the temperature increases, the high vibrational state populations become more influential.

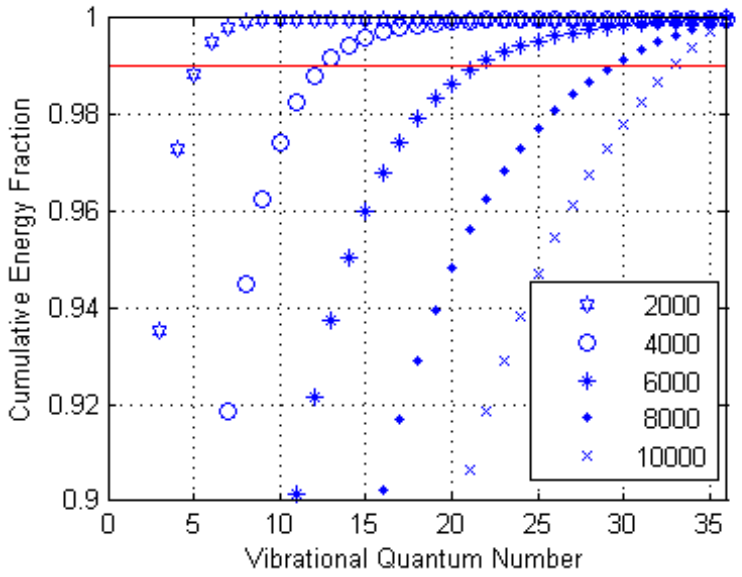

Figure 2.6: Cumulative Vibrational Energy for Several Temperatures

As discussed previously, collisions are the mechanism by which gas particles exchange energy and change chemical state. The details about rates will be discussed in subsequent sections. The primary collisions of interest in this dissertation are shown below:

$$O_2(v) + M \rightarrow O_2(v') + M \tag{2.10}$$

$$O_2(v) + O_2(w) \rightarrow O_2(v') + O_2(w') \tag{2.11}$$

$$O_2(v) + M \rightarrow O + O + M \tag{2.12}$$

Equation 2.10 represents vibrational-translational energy transfer. Equation 2.11, in the most general terms, represents vibrational-vibrational-translational energy transfer. However, depending on the before and after collision states, it could be vibrational-vibrational or vibrational-translational energy transfer. The final equa-

tion, Equation 2.12, displays the dissociation collision for molecular oxygen with a generic gas particle.

2.2 Nonequilibrium Modeling: Vibrational Representation

The vibrational energy mode must be represented in the model separate from the translational energy mode in order to capture nonequilibrium behavior. The two main approaches for vibrational energy mode representation are the two-temperature (2T) model and the state-to-state (STS) model. The 2T model represents the vibrational energy mode with a single quantity, the vibrational temperature, T_v. The STS model uses the vibrational state populations to represent the vibrational energy mode. The 2T model is simple and computationally efficient. However, it is restricted by it's use of a single parameter for the energy mode. The STS model can describe an arbitrary vibrational state distribution that might deviate from the Boltzmann distribution assumption of the 2T model. The STS model also has a significant computational expense, potentially prohibitive in some cases.

2.3 Nonequilibrium Modeling: Two-Temperature Approach

2.3.1 Background

The two-temperature model is the widely used approach for hypersonic vehicle analysis[2]. As the name suggests, the method uses two temperatures to describe the thermodynamic energy behavior. These temperatures correspond to the translational and vibrational energy modes. These modes cannot be described by a single temperature in the hypersonic regime due to the differences in time scales for the activation and relaxation of the various energy modes. For vibrational relaxation, the approach relies on a relaxation time that is a function of temperature and pressure to solve the Landau-Teller equation for vibrational energy. The Millikan-White

(MW) formula for vibrational relaxation time is generally used, and correlates well with experimental data for many molecular systems [3]. The good correlation with experimental data is observed for both the O_2-Ar and O_2-O_2 systems. One of the exceptions is the O_2–O system that does not correlate well with experimental data[4, 5]. The O_2-O system violates many of the assumptions that are present in the underlying Landau-Teller theory that dictates the temperature dependence of the Millikan-White formula. Specifically, the O_2-O system differs in that it contains a molecule and an open-shell atom. This attribute leads to additional mechanisms that are not included in the Landau-Teller theory, such as non-adiabatic transitions and the possibility of atom exchange. Park and others have adjusted the Millikan-White coefficients for O_2-O to correlate better with experimental data[6]. However, the previous work has still assumed the temperature dependence dictated by the Landau-Teller theory. The vibrational relaxation of O_2-O is studied in this work using recently developed rates from a detailed quasi-classical trajectory (QCT) analysis[7]. The vibrational relaxation times obtained using the extensive quasi-classical trajectory analysis coupled to the set of master equations indicated that relaxation is the most effective at low temperatures, which is opposite to the temperature dependence assumed in the MW equation. Chemistry is captured by reaction rates that use Arrhenius-type rate coefficients. Additionally, the Arrhenius form uses the geometrically averaged temperature of the translational and vibrational temperature ($T_a = \sqrt{T_t T_v}$) in order to capture nonequilibrium, thermochemical coupling.

The post normal shock calculations presented in this chapter use the jump conditions derived from the Rankine–Hugoniot relations. The derivation assumes that the electronic and vibrational modes are frozen across the shock wave. The flow downstream of the shock wave is calculated by solving the one-dimensional compressible flow equations combined with the conservation equations associated with the

vibrational energy mode. The compressible flow equations are shown in (2.13).

$$\frac{\partial}{\partial x}\begin{pmatrix} \rho_s\, u \\ \rho\, u^2 + p \\ \rho\, u\,(h + u^2/2) \end{pmatrix} = \begin{pmatrix} \omega_s \\ 0 \\ 0 \end{pmatrix}, \tag{2.13}$$

where ρ and ρ_s are the densities of the local flow and of the species s, u, P, h are the local flow velocity, pressure and enthalpy, ω_s is the production rate of species s due to chemical reactions. The system of Euler equations (2.13) is closed by the ideal gas law and enthalpy equation. Enthalpy is defined as $h_s = h_0 + 2.5RT + (e_r + e_v)$ and is multiplied by the molar concentration of the species to close the system.

The conservation equations for vibrational energy are formulated individually for the 2T and STS models and given in the following sections.

2.3.2 Two-Temperature Model

In the two-temperature (2T) model, nonequilibrium in the energy transfer is described by separating the trans-rotational energy, $e_t(T)$, and the vibration-electronic energy, $e_v(T_v)$. The present work accounts for only the ground electronic state. The conservation equation for vibrational energy has the following appearance:

$$\frac{\partial\,(\rho e_v)}{\partial x} = \rho_{O_2}\frac{e_v^\star - e_v}{\tau_v\,(T_a)} + \dot{\omega}_{O_2} C_{VD}\,(T)\,D_e, \tag{2.14}$$

where $\dot{\omega}_{O_2} = R\,(T_a)\,n_O^3 - D\,(T_a)\,n_{O_2} n_O$, D and R are the global dissociation and recombination rate coefficients evaluated at some effective temperature T_a defined below, n is the number density, e_v and $e_v^\star$ are the specific internal vibrational energies evaluated at translational (T) and vibrational (T_{vib}) temperatures, respectively, C_{VD} is the vibration-dissociation coupling coefficient that indicates the average loss of vibrational energy in a collision of particles that leads to dissociation, τ_v is the

relaxation time of the entire vibrational manifold, and D_e is the classical dissociation energy of diatomic O_2. It should be noted that the experimental comparisons in the presented work are performed in the time domain. A transformation from the post shock position domain into the time domain was done is employed using the local velocity and shock velocity.

The present work will study three aspects of the two temperature modeling: vibrational-translational energy relaxation, dissociation rate, and vibrational energy loss due to dissociation. The available QCT data for the O_2–Ar and O_2–O systems allow for modifications to be made to the 2T model. The results section will demonstrate the isolated and combined effect of these modifications relative to the 2T model implementation.

2.3.2.1 Vibrational-Translational Energy Transfer

The relaxation time, τ_v, in Equation 2.14 can be obtained from various methods. The most widely accepted method is the Millikan-White relaxation time shown in (2.15). The values for A and B are unique for each interaction of colliding species, and can be calculated based on the reduced mass, μ, and vibrational characteristic temperature, θ_V, as follows, A=$0.00116\mu^{\frac{1}{2}}\theta^{\frac{4}{3}}$ and B = $0.015\mu^{\frac{1}{4}}$ [3].

$$P\tau_v = exp(A(T^{-1/3} - B) - 18.42), [atm - sec] \tag{2.15}$$

The Millikan-White relaxation time is modified with the collision-limited correction term shown in (2.16) and (2.17). It is also referred to as the high temperature correction (HTC). The correction terms include the number density, n, and the mean particle thermal velocity, c. In this work, σ_v^* is set to 3.0×10^{-21} m^2 as proposed by Park [6].

$$\tau_{Park} = 1/\left(n\sigma_v c\right), [sec] \tag{2.16}$$

	A	B
$O_2 - Ar$	165.0	0.031
$O_2 - O_2$	135.91	0.030
$O_2 - O$	47.7	0.0271

Table 2.1: Millikan-White Relaxation Parameter Equation Coefficients[2]

$$\sigma_v = \sigma_v^* \left(50,000/T\right)^2, \left[m^2\right] \tag{2.17}$$

The present work adopts the Millikan-White relaxation time for the O_2–Ar and O_2–O_2 systems[6, 17]. However, the assumptions inherent in this model do not apply well to a system containing a molecule and an open shell atom, like the O_2–O system[21, 22]. These types of systems deviate from these model assumptions due to the effect of additional mechanisms such as non-adiabatic transitions and the possibility of atom exchange. The experimental data for the O_2–O system has been shown to not follow the Millikan-White suggested behavior. Park[6] proposed Millikan-White coefficients for O_2–O based on the data from Ref. [5], however, the temperature dependence was still assumed to be consistent with the MW empirical correlations for τ_v. Table 2.1 summarizes the coefficients used for the Millikan-White version of the 2T model.

One of the main areas of focus for this work is to utilize the newly available QCT calculated transition rates for O_2–O from Andrienko and Boyd[23]. Two sets of state-to-state transition rates are constructed in the QCT work. First, a simplified, pairwise Hulbert-Hirshfelder (HH) PES [24] is applied. The PES supports a maximum of 36 vibrational states and 223 rotational levels for the electronic ground-state O_2. This simplified HH PES is computationally less expensive than a more accurate PES. Second, an accurate many-body PES is adopted. The Varandas and Pais PES [25] generates 47 vibrational states and a maximum of 236 rotational levels for electronic ground-state molecular oxygen. More details about the QCT and PES approaches are presented in the STS section of this chapter. These QCT results have been integrated

	a	b	c	d
2T HH PES	-4.407 $\times 10^{-6}$	-0.005662	0.5433	0.08702
2T Varandas PES	2.304×10^{-3}	-0.07254	1.245	1.70

Table 2.2: $O_2 - O_2$ Vibrational relaxation curve fit coefficients obtained from QCT analyses

in order to create a vibrational relaxation parameter relation that is in the form of the Landau-Teller theory formulation. Equation (2.18) presents the curve fit form of the vibrational relaxation parameter for the QCT based results[26]. Table 2.2 lists the curve fit coefficients for each PES.

$$P\tau_{vib} = (ax^3 + bx^2 + cx + d) \times 10^{-8} \quad [atm - sec],\ x = T/10,000 \tag{2.18}$$

Figure 2.7 compares the O_2–O vibrational relaxation times from different methods. The O_2–O_2 vibrational relaxation time is also shown for reference. The O_2–O Park curve fit of the MW dependence to experimental data[5] matches up well with the data by Breen[4] only in the temperature range between 1000 and 3500 K. Above this temperature, the O_2–O MW relaxation time significantly underestimates the QCT data. In fact, the QCT results deviate from the Landau-Teller temperature dependence. The O_2–O system does not adhere to the STS transition assumptions of Landau-Teller theory, however using a vibrational relaxation time to represent the internal energy evolution can capture the behavior appropriately[7]. The vibrational relaxation time, derived from the QCT rates based on the HH PES slightly underestimates Breen's data. This is due to the crude representation of potential well in the HH PES, which appears to be too deep and wide, compared to that of the Varandas PES. However, each PES demonstrates a similar tendency in vibrational relaxation time behavior.

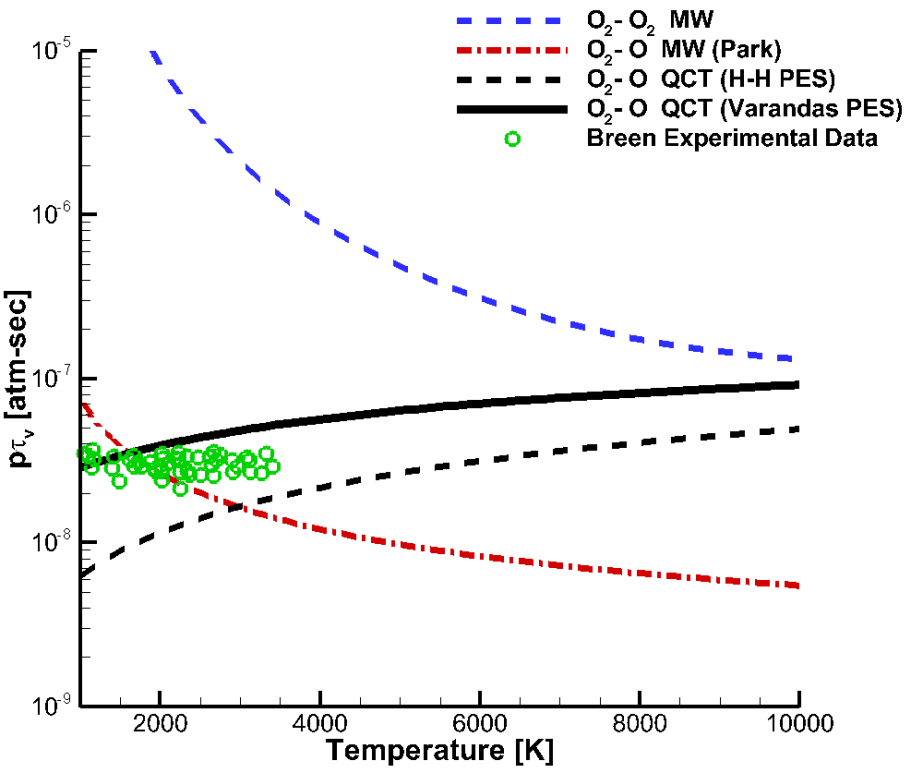

Figure 2.7: Vibrational relaxation parameter obtained from various models

	C	n	θ_d
O_2-Ar (Park)	1.80×10^{18}	-1.0	59360
O_2-O_2 (Park)	2.00×10^{21}	-1.5	59360
O_2-O (Park)	1.00×10^{22}	-1.5	59360
O_2-O (HH)	1.17×10^{18}	-0.52	60540
O_2-O (Varandas)	1.73×10^{18}	-0.40	60540
O_2-O (QSS)	9.00×10^{22}	-2.2	65000

Table 2.3: Arrhenius parameters of dissociation reaction, pre-exponential factor is in cm^3/s/mole and $theta_d$ is in degrees Kelvin

2.3.2.2 Dissociation Rate Coefficient

In the 2T model, the dissociation process is generally represented by the Arrhenius-type temperature dependence. The Arrhenius form is shown in (2.19). The effect of vibrational nonequilibrium is modeled by changing the controlling temperature to the geometrically averaged temperature of the translational and vibrational temperature ($T_a = \sqrt{TT_v}$) as proposed by Park. The inclusion of the vibrational temperature implicitly defines the effect that vibrational nonequilibrium has on the dissociation behavior. The QCT results of Andrienko and Boyd [23] suggest that utilizing the quasi-steady state (QSS) dissociation rate could be a more accurate way to model the dissociation process for O_2–O. The final dissociation model investigated in this work is the QCT based QSS dissociation rate. As a note, this method is controlled by the translational temperature because of the QSS derivation[23] of the rates and QSS is defined as the state at which the population rate of change is equal to zero. Additionally, the Arrhenius coefficients associated with the various models are summarized in Table 2.3.

$$k_d = C\, T_a^n exp\left(-\frac{\theta_d}{T_a}\right) \qquad \left[\frac{cm^3}{s}\right] \tag{2.19}$$

One would expect that the vibrational-translational energy transfer and the dissociation would depend on the vibrational population distribution. It should be noted that the 2T methodology assumes that the vibrational population follows a Boltzmann distribution. This assumption is embedded in the formulation of the Landau-Teller equation and the dissociation model.

2.3.2.3 Vibrational Energy Loss Due To Dissociation

When a molecule dissociates, its vibrational energy is removed as part of the process of breaking the chemical bond, and the loss of internal energy must be accounted for in the model. Since the dissociating molecule could be at a low vibrational state or a high vibrational state, an assumption must be made as to an average vibrational energy loss due to dissociation. It is customary to use a fraction (C_{VD}) of the dissociation energy to describe this vibrational energy loss. Physically, the average loss of vibrational energy is a complex function of translational temperature and instantaneous population of the vibrational manifold. The 2T model typically assumes that C_{VD} is constant, generally near 0.45. The constant value for C_{VD} will be used for the $O_2 - Ar$ system. For $O_2 - O$ and $O_2 - O_2$, the work of Andrienko and Boyd[23] has presented the temperature dependence for C_{VD} based on master equation analysis. The C_{VD} temperature dependence has been curve fit to the form of (2.20) with the coefficients presented in Table 2.4. See Figure 2.8 for the data points from the master equation analysis and the curve fits. Note that the work assumes that the governing temperature for this quantity is the translational temperature. This assumption does not capture the vibrational population effects on C_{VD}, however the full dependence on vibrational temperature and population has not been captured in a compact form. Additionally, the C_{VD} parameter does not change much during intensive dissociation phases[23]. The presented work focuses on post normal shock conditions that contain significant dissociation, so the translational temperature formulation of C_{VD} is an

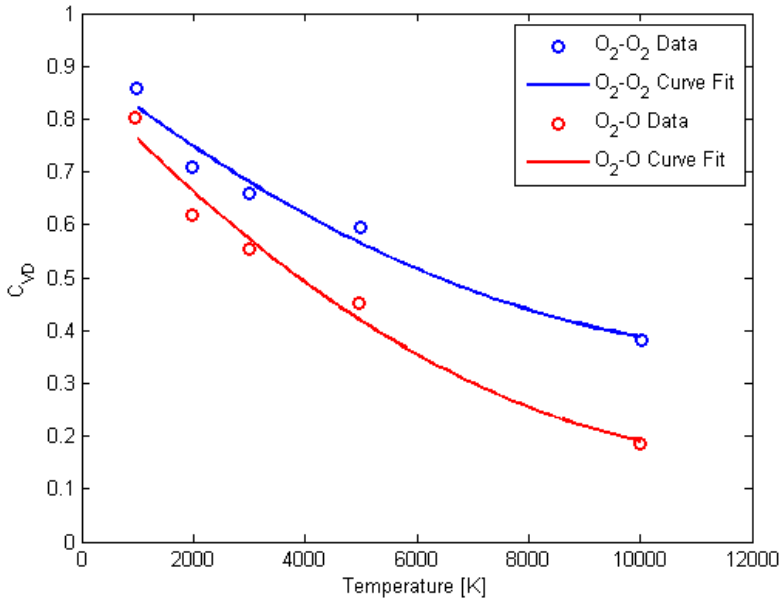

Figure 2.8: C_{VD} Data and Curve Fits for Oxygen Systems

	A	B	C
O_2–O_2	0.3216	-0.8362	0.9020
O_2–O	0.4505	-1.1294	0.8699

Table 2.4: Curve fit parameters for vibrational energy loss coefficient due to dissociation

acceptable assumption.

$$C_{VD} = Ax^2 + Bx + C, \; x = T/10000, \tag{2.20}$$

An investigation is performed in the results section to understand the impact of the temperature dependent C_{VD} modeling approach against the standard assumption of a constant C_{VD} value.

2.4 Nonequilibrium Modeling: State-To-State Approach

2.4.1 Background

The state-to-state (STS) approach is a higher fidelity model for describing the nonequilibrium energy transfer that has been used sparingly for decades, but has become more popular recently due to advances in computational power [8, 9, 10, 11, 12, 13, 14, 15, 16]. The STS model is computationally expensive since it directly simulates the population of each vibrational state. These populations are governed by the system of master equations that employ state-specific rates obtained by quasi-classical trajectory (QCT) simulations or simpler models [17]. This approach allows for multi-quantum transitions and non-Boltzmann distributions to be captured [11, 18, 8]. There are three widely used methods for deriving the required transition rate coefficients: the Schwartz, Slawsky, and Herzfeld (SSH) theory based on first-order perturbation, the forced harmonic oscillator (FHO) model of Adamovich [17] and the QCT analysis[19]. The presented work will focus on the FHO and QCT methods. The FHO model is a semi-classical analytical method that was developed from nonperturbative analytic theory assuming that the interaction of target and projectile particles is governed by a strong repulsive potential. The closed form of the FHO rate coefficients makes it very attractive due to the low computational expense required to generate transition rates. However, the assumptions including the form of the potential energy surface (PES) put a limitation on the systems that are described accurately by the FHO methodology. The FHO model is not applicable for molecular systems that have open-shell atoms and molecules, and in particular for the O_2-O collisions. The QCT method is a more general approach and the transition rates can be obtained for any PES. The QCT method employs Monte-Carlo methods of statistical sampling of kinetic and internal energy of particles to accumulate a large-scale database of transition event probabilities. The QCT method is computationally

expensive, but the recent increase in computational power has made it tractable for atom-diatom interactions. As an example the QCT work of Andrienko and Boyd[23] computational expense on the order of weeks using 100s of cores.

2.4.2 State-to-State Model

The conservation of vibrational energy in the STS model is formulated for each vibrational energy level. This approach significantly increases the number of equations to be solved, however it eliminates highly-averaged parameters such as τ_v and C_{VD} that can vary drastically for each vibrational energy level.

$$\frac{\partial}{\partial x}\begin{pmatrix} \rho_s\, u \\ \rho\, u^2 + p \\ \rho\, u\,(h + u^2/2) \end{pmatrix} = \begin{pmatrix} \omega_s \\ 0 \\ 0 \end{pmatrix}, \tag{2.21}$$

The system of equations for the STS model in this case accounts for the conservation of momenta and trans-rotational energy as well as for number density of individual vibrational states. The latter has the following appearance:

$$\frac{\partial n_v}{\partial x} = \sum_s \left(R_{v,s} n_O^2 n_s - D_{v,s} n_v n_s\right) + \sum_s \left(K_{v',v} n'_v n_s - K_{v,v'} n_v n_s\right),\ v = 0...v_{max} \tag{2.22}$$

The evolution of the master equation system is straightforward and does not have any inherent uncertainty in the method. The model demands a set of STS rates to account for vibrational state transitions, and the STS rates are where the uncertainty is introduced. These vibrational state transitions are separated into two types. First, bound-bound transitions are simply a change of vibrational state, such as going from v = 1 to v =3. Second, bound-free transitions represent a dissociation event. Two different methods for calculating a set of STS rates are evaluated in the present work.

2.4.2.1 STS Rates: Forced Harmonic Oscillator (FHO)

The forced harmonic oscillator (FHO) method is an analytic, nonperturbative, semiclassical method for developing a set of STS rates. The standard application of the FHO model utilizes a purely repulsive potential that is governed by the exponential potential parameter α shown in Equation 2.23. This simple form of the potential allows for an analytical form of the transition probabilities, and consequently STS rates, to be possible.

$$V(r) \sim \exp(-\alpha r) \tag{2.23}$$

The entire formulation for the FHO rates is presented in Equations 2.24 through 2.30, where Z is the collision frequency, $\tilde{m}$ and μ are the reduced masses, k is the Boltzmann constant, $\hbar$ is the Planck's constant, and κ is the molecule/atom indicator (1 for molecule collision partner, 0 for atom collision partner) . It should be noted that the equation for C_{VT} (Equation 2.28) is in implicit form. This requires an iterative solver scheme (Newton's method, secant method, etc.). The FHO formulation is rather cumbersome, but the primarily algebraic, closed form allows computationally inexpensive generation of a set of STS rates.

$$k(v \to v', T) = Z\left(\frac{2\pi}{3+\delta}\right)^{\frac{1}{2}} \frac{\left(n_s S_{VT} \frac{\theta'}{\theta}\right)^s}{(s!)^2} C_{VT} \left(\frac{s^2\theta'}{T}\right)^{\frac{1}{6}} \times exp\left[-\left(\frac{s^2\theta'}{T}\right)^{\frac{1}{3}} (1-\phi_m)^{\frac{2}{3}} \times \left(\frac{C_{VT}^2}{2} + \frac{1}{C_{VT}}\right) - s\left(1 - C_{VT}^3\right)\right] exp\left(\frac{\theta s}{2T}\right) \tag{2.24}$$

$$\theta' = \frac{8\pi^2\omega^2\left(\frac{\tilde{m}^2}{\mu}\right)\gamma^2}{\alpha^2 k}, \quad \theta = \frac{\hbar\omega}{k} \tag{2.25}$$

$$\delta = \frac{1 - C_{VT}^3}{C_{VT}^3} \frac{2\pi\omega}{\alpha v_{m0} C_{VT}}, \quad \phi_m = \frac{2}{\pi} tan^{-1}\left[\left(\frac{2E}{\tilde{m} v_{m0}^2}\right)^{\frac{1}{2}}\right] \tag{2.26}$$

$$v_{m0} = \left(\frac{2\pi\omega skT}{\alpha\tilde{m}} \right)^{\frac{1}{3}} \tag{2.27}$$

$$C_{VT} = \frac{v_m}{v_{m0}} \cong \left[1 - \frac{1}{s} \left(\kappa + \frac{2n_s}{(s+1)} \right) S_{VT} \frac{\theta'}{\theta} exp \left(- \frac{2\pi\omega}{\alpha v_{m0} C_{VT}} \right) \right] \tag{2.28}$$

$$s = |v - v'|, \quad n_s = \left[\frac{max\,(v, v')!}{min\,(v, v')!} \right]^{\frac{1}{s}} \tag{2.29}$$

$$\omega = \frac{\epsilon_v - \epsilon_{v'}}{s} \frac{k}{\hbar} \tag{2.30}$$

Previous FHO[17] work for oxygen has shown that the value of α is near 4.0 Angstroms^{-1}. This value is based on the comparison of vibrational relaxation time in pure oxygen obtained by means of the master equations with the experimental data. The present work will investigate the sensitivity of the FHO α parameter used in the O_2–O_2 STS rates. α parameters of 3.8, 4.0, and 4.2 Angstroms^{-1} are studied. The O_2–O_2 state-specific dissociation rates are available in the FHO methodology, however, the present work determines the dissociation rates by scaling the O_2–O rates using the global dissociation rates of Bortner [23, 27]. Previous work by Kim has proven the scaling approach for dissociation rates.

The VT transition rates for the O_2–O_2 system are taken from FHO analysis[23, 17]. These rates are used in a post-normal shock calculation using the master equation approach.

2.4.2.2 STS Rates: Quasi-Classical Trajectory (QCT)

Quasi-classical trajectory analysis is a technique for numerically simulating the collision between gas particles. The analysis starts with two particles moving toward

each other, and then evolves the particle trajectories based on the attractive/repulsive forces that the particles impart on each other. Once the particles have interacted and leave the domain, the simulation terminates. Thousands and millions of simulations are computed with different initial conditions that correspond to translational temperature, rotational state, and vibrational state. Each simulation has a corresponding initial state and final state. Probabilities are calculated from these simulation results, and these probabilities are integrated to provided STS rates.

The forces between the gas particles are defined by the potential energy surface (PES). The QCT analysis can be performed on any arbitrary PES. The work in this dissertation focuses on the STS results based on QCT analysis for both the $O_2 - Ar$ and $O_2 - O$ systems. Currently, the $O_2 - O_2$ system does not have an accurate, well supported PES, so FHO STS rates are used instead of QCT analysis based rates.

Potential Energy Surfaces

The $O_2 - Ar$ system uses a PES with the form shown in Equation 2.31. The O-O potential uses the Hulbert-Hirshfelder (HH) potential energy, and uses potential parameters from Rydberg-Klein-Rees (RKR) and the National Institute of Standards and Technology (NIST) database. The O-Ar potential uses the Buckingham equation and potential parameters from Kroes and Rettschnick and Gross and Billing. The two potentials are shown visually in Figures 2.9 and 2.10.

$$V_{O-O-Ar}\left(r_a, r_b, r_c\right) = V_{O-O}\left(r_a\right) + \sum_{i=a,b} V_{O_i-Ar}\left(r_i\right) \tag{2.31}$$

The $O_2 - O$ system uses two PES options for the QCT analysis. First, a simplified, pair-wise Hulbert-Hirshfelder (HH) PES [24] is applied. The PES supports a maximum of 36 vibrational states and 223 rotational levels for the electronic ground-state O_2. This simplified HH PES is computationally less expensive than a more accurate PES. Second, an accurate many-body PES is adopted. The Varandas and Pais PES [25] generates 47 vibrational states and a maximum of 236 rotational levels

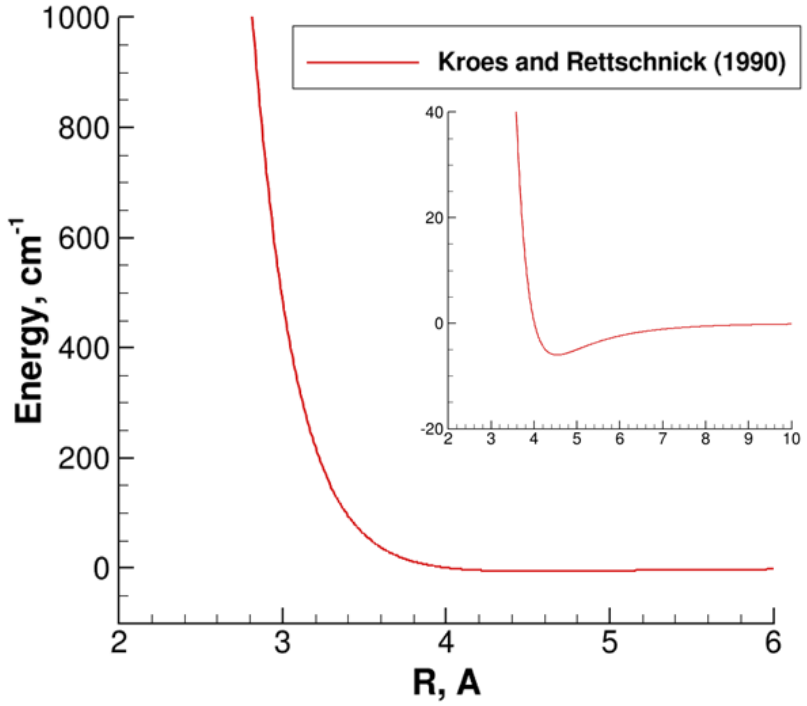

Figure 2.9: O-Ar Potential Energy Surface for QCT Analysis

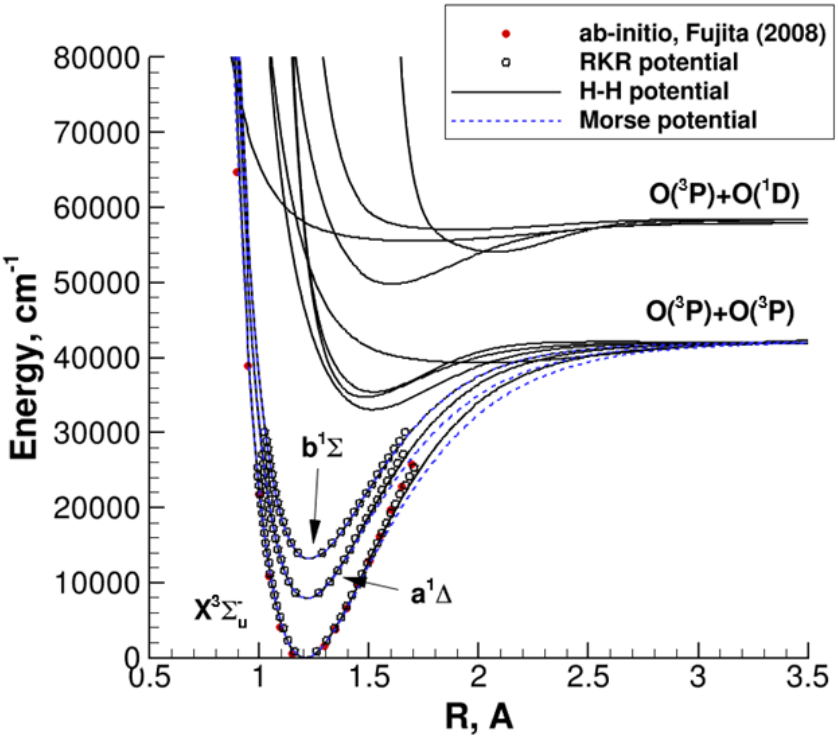

Figure 2.10: O-O Potential Energy Surface for QCT Analysis

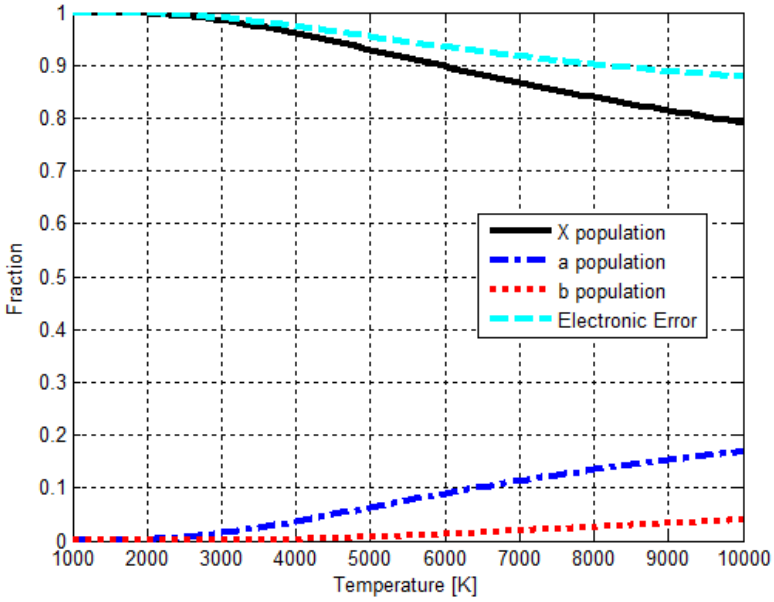

Figure 2.11: Electronically Excited Oxygen Population Evaluation

for electronic ground-state molecular oxygen.

It should be emphasized that the work in this dissertation only models electronic ground-state molecular oxygen. Figure 2.10 shows that there are two low lying excited states available ($a^1\Delta$ and $b^1\Sigma$). Figure 2.11 presents an evaluation of the electronically excited populations as a function of temperature. The results show that the effect of electronically excited oxygen is less that 10% for 8,000K and less. Future work will investigate the importance and influence of the electronically excited oxygen in nonequilibrium modeling.

The final results for STS rates are obtained from QCT analysis provided in a curve fit form as shown in (2.32) and (2.33) for bound-bound and bound-free transition rate coefficients.

$$K_{v,v'} = 10^{-12} \times \exp\left[A_{v,v'} + B_{v,v'}/\log(T/1000) + C_{v,v'}\log(T/1000)\right], \ \left[cm^3/s\right], \tag{2.32}$$

$$D_v = A_v T^{B_v} exp\left(-C_v/T\right), \ \left[cm^3/s\right] \tag{2.33}$$

It should be noted that vibrational temperature is used for experimental comparisons in the presented work. The vibrational temperature is calculated by taking the total vibrational energy from the STS simulation and using it to a Boltzmann equivalent vibrational temperature.

2.4.3 Modified Two-Temperature Model (2T-NENB)

A modified two-temperature model is presented that attempts to address some of the short comings of the standard two-temperature model. Previous work has shown that hypersonic oxygen flows can often contain vibrational nonequilibrium behavior and non-Boltzmann vibrational population distributions[28, 29, 30]. Both of these features have a strong effect on the flow field solution and cannot generally be captured with the standard 2T model.

In order for a thermochemical model to accurately represent hypersonic flows containing oxygen, it needs to account for vibrational nonequilibrium and non-Boltzmann vibrational population distribution effects. The 2T-NENB (NonEquilibrium, Non-Boltzmann) model is developed by investigating the state-to-state transition and dissociation rates. Specifically, the state resolved rates can be used to understand the influence that vibrational nonequilibrium and non-Boltzmann distributions have on the macroscopic level vibrational-translational energy transfer and the total dissociation rate. Formally, a complete master equation analysis is required to capture the exact behavior of the effects in question. However, the present work is strictly concerned with flows that are dominated by post shock relaxation behavior. This focus allows for a number of assumptions to be made and a useful model to be developed.

STS rates allow for detailed information about the vibrational-translational energy transfer and dissociation. Specifically, an evaluation can be made for arbitrary combinations of translational temperature and vibrational temperatures or population distributions. This detailed understanding from high fidelity STS rates allows

	C	n	θ_d
Varandas PES	1.725×10^{18}	-0.4037	60540.0

Table 2.5: Arrhenius parameters of dissociation reaction, pre-exponential factor is in $cm^3/s/mole$ and θ_D is in degrees Kelvin

for a reduced order model to be developed. It is desired to retain the framework of the 2T model due to its widespread use.

One of the main areas of focus for this work is to apply the QCT calculated transition rates for O_2-O from Andrienko and Boyd[26]. A set of state-to-state transition rates was constructed using an accurate many-body PES. The Varandas and Pais PES[26] generates 47 vibrational states and a maximum of 236 rotational levels for electronic ground-state molecular oxygen.

The equilibrium dissociation rate for O_2-O has also been extracted from the QCT data. The Arrhenius parameters are shown in Table 2.5.

The utilization of the state resolved rates is potentially very powerful. It allows any vibrational distribution to be evaluated for vibrational-translational energy transfer and total dissociation rate. The 2T-NENB model takes the form of the standard 2T model but has modification terms to account for nonequilibrium and non-Boltzmann effects. The dissociation behavior has a dominating influence on the overall solution. The development of these dissociation modifications are shown in detail below.

The dissociation portion of the 2T model uses Arrhenius-type rate coefficients. Generally, the nonequilibrium effect on the dissociation rate is captured by the use of a control temperature in the dissociation rate equation. The nonequilibrium 2T-NENB model will use the behavior from the detailed STS rates to guide the control temperature formulation. Various formulations of the control temperature have been utilized throughout the history of nonequilibrium modeling. The most popular control temperature formulation is by Park[2] ($T_a = \sqrt{T_t T_v}$). A generalized version of the Park formulation has been studied previously[37] ($T_a = T_t^{(a)} T_v^{(1-a)}$). Additionally, a

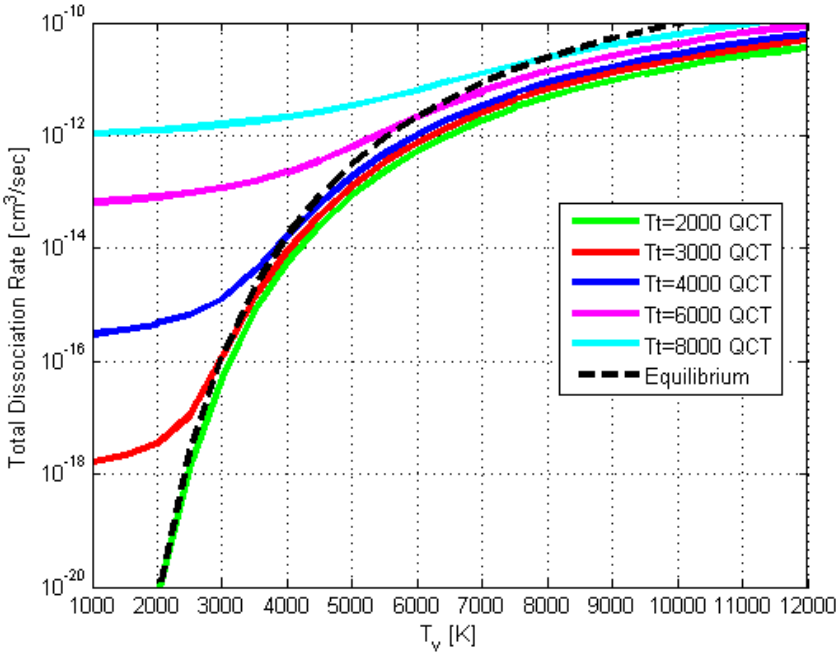

Figure 2.12: O_2-O Total Dissociation Rate for Combinations of Translational and Vibrational Temperatures (Boltzmann)

more complex and general formulation is suggested in the recent work of Fujita[31] and is presented in Equation 2.34. With accurate state-to-state rates from QCT for the O_2-O system and rates from FHO for the O_2-O_2 system, the best formulation can be selected. A range of translational and vibrational temperature combinations are used to determine the accurate total dissociation rate. The focus of this specific exercise is to study the nonequilibrium effect on total dissociation rate. All populations for this exercise are assumed to have a Boltzmann distribution. The effects of non-Boltzmann distribution will be investigated later in this section.

Figure 2.12 shows the QCT generated total dissociation rate for a number of translational temperature and vibrational temperature combinations for the O_2-O system. The equilibrium total dissociation rate is also plotted. The figure suggests that a non-symmetrical treatment of the control temperature is needed to capture both heating and cooling behaviors properly.

Additionally, Figure 2.13 compares the nonequilibrium effect predicted dissocia-

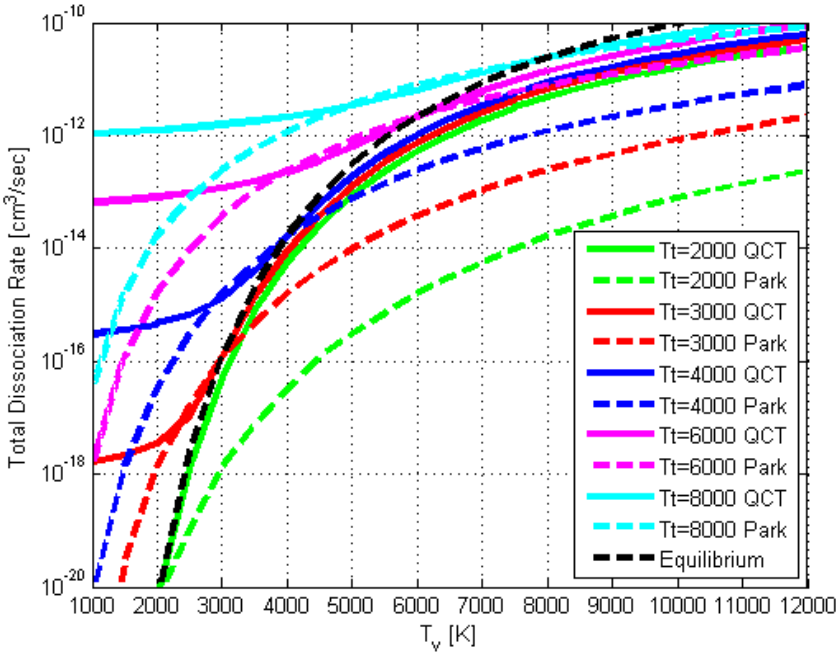

Figure 2.13: O_2-O Total Dissociation Rate from QCT Analysis and Park Nonequilibrium Model

tion rates by the Park model against the QCT based dissociation rates. The Park model captures the behavior near equilibrium for heating flow conditions. However, the Park model deviates from the QCT based dissociation rates for strong nonequilibrium conditions and cooling flows. The shape of the profiles differs between the QCT STS rate based behavior and the Park model. This difference suggests that a more complex form of the control temperature is required to properly capture the behavior.

The presented work aims to develop a reduced order model based on the understanding of the detailed QCT results. As previously mentioned, the developed model should fit within the 2T framework since it has widespread use. The most efficient way to implement the nonequilibrium effect on dissociation rate is to make a correction to the control temperature. The equation below presents the form of the control temperature that is being used.

$$T_a = T_t \left(A + (1 - A) \left(\frac{T_v}{T_t} \right)^B \right) \tag{2.34}$$

The parameters are determined using a curve fitting process using the selected control temperature form and the STS dissociation rate data. Specifically, an error function is introduced then the parameters will be calculated with the goal of minimizing the error value. The error function for this process is presented in Equation 2.35 and is a normalized formulation of error. The translational temperature and vibrational temperature space is discretized from 1000K-12,000K at increments of 500K.

$$error = \sum \frac{(k_{fit} - k_{STS})}{k_{STS}} \tag{2.35}$$

Figure 2.14 presents the final selection of the control temperature parameters. Specifically, during heating, A=0.65 and B=3.0 and during cooling, A=0.2 and B=1.0 for the O_2-O system. The same procedure is applied to the O_2-O_2 system resulting in A=0.65 and B=3.0, and A=0.1 and B=1.0 for heating and cooling, respectively. The presented model is able to capture the nonequilibrium effect on dissociation rate over a larger range than the Park form of the control temperature.

Next, the state resolved QCT rates are used to determine the effect of a non-Boltzmann vibrational distribution on the total dissociation rate. In principle, the vibrational distribution can be anything. However, in relevant hypersonic flow conditions, the distributions deviate from Boltzmann in very specific ways. The presented work will focus on post shock relaxation conditions to guide the study of non-Boltzmann distributions. Figures 2.15 and 2.16 show the typical evolution of the vibrational distribution after a shock. The distribution quickly becomes over-populated relative to the Boltzmann distribution after the shock. As the distribution evolves, the distribution becomes a Boltzmann for an instance before continuing to an

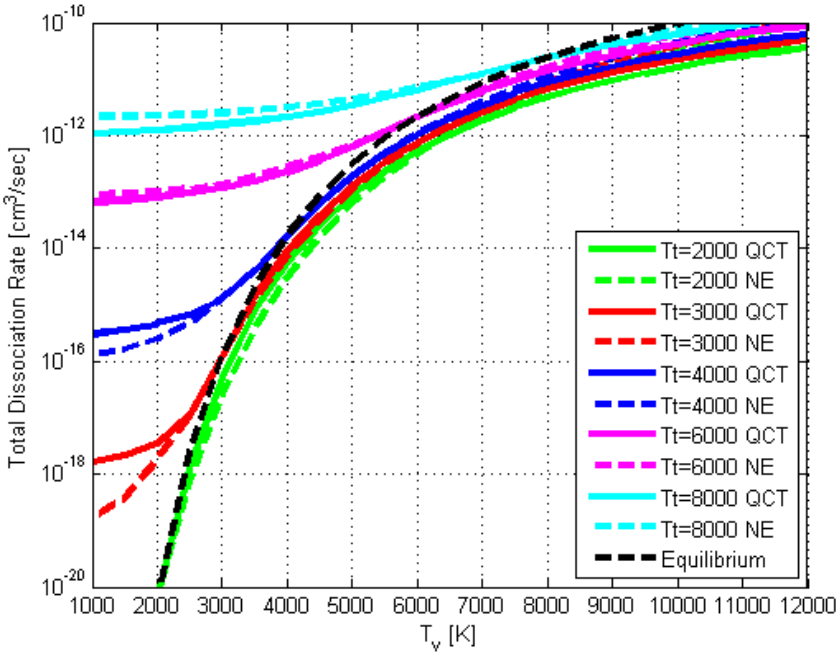

Figure 2.14: O_2-O Total Dissociation Rate from QCT Analysis and Presented Nonequilibrium Model

underpopulated tail distribution. This underpopulated tail distribution corresponds to a region of QSS or near QSS behavior. This evolutionary behavior of the population has been observed in other studies[28, 29] and with other species[30].

Now that the type and range of non-Boltzmann distributions have been identified, a model form must be selected. In general, the distribution at a given point in time or space depends on the evolutionary history of that particular set of molecules. The modifications proposed in this thesis aim to fit into the framework of the standard 2T model. With this restriction, the only information about the vibrational population history is in the form of the vibrational temperature. That means that an assumption about the population history must be made in order to be useful in this framework. This could be considered the largest concession in generality for this model. However, the loss in generality leads to more convenience and a much reduced computational expense. Using the QCT rate results and post shock relaxation information as a guide, a scale factor is placed on the total dissociation rate to account for non-

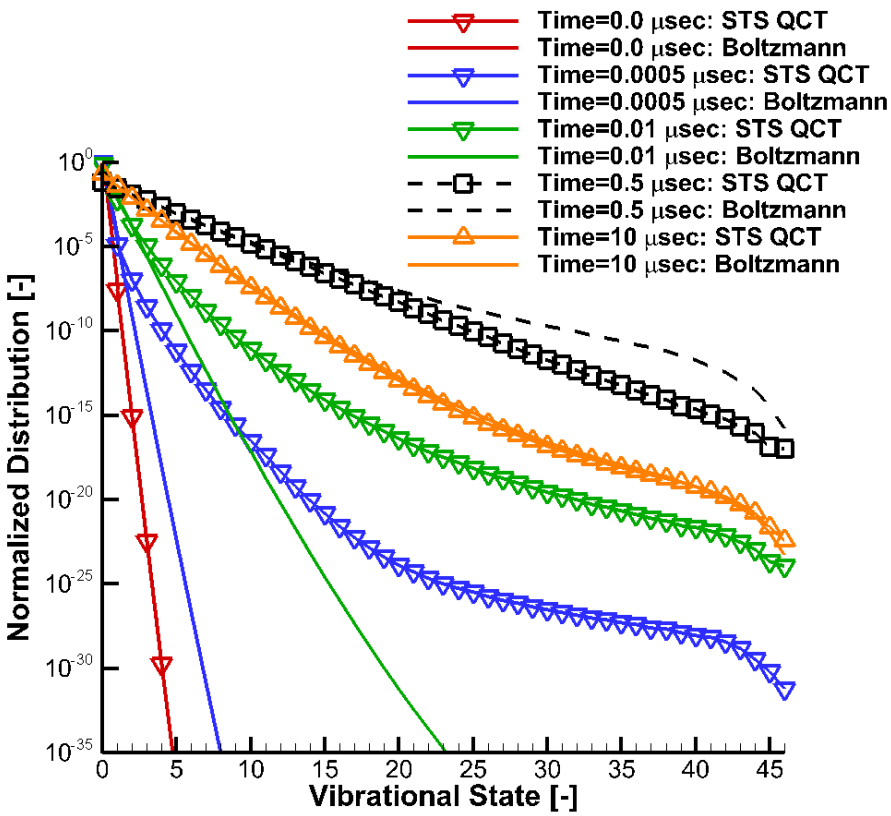

Figure 2.15: Vibrational population distribution evolution, sample

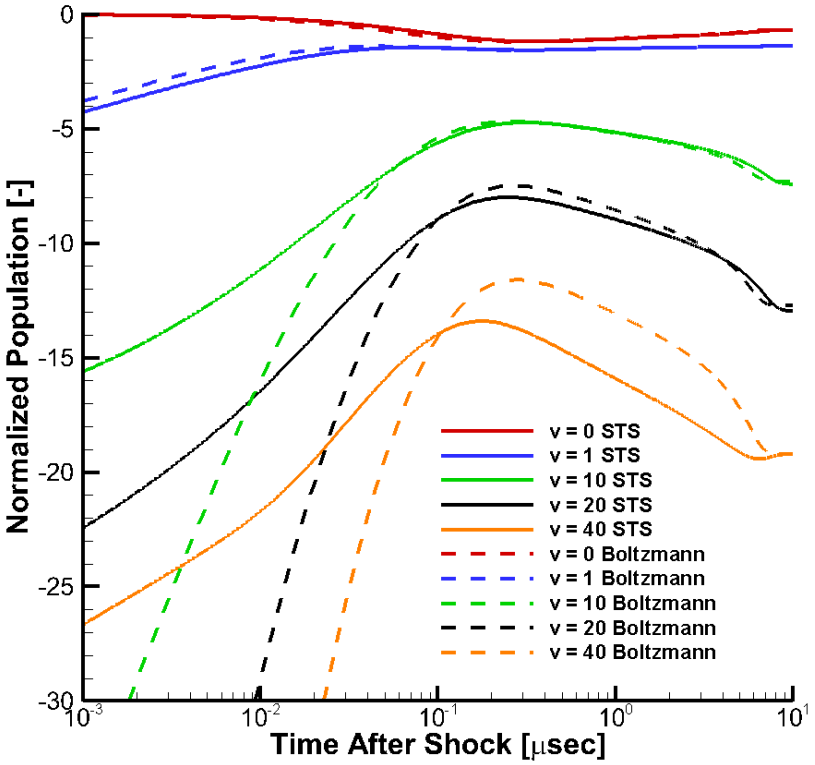

Figure 2.16: Vibrational state population evolution, sample

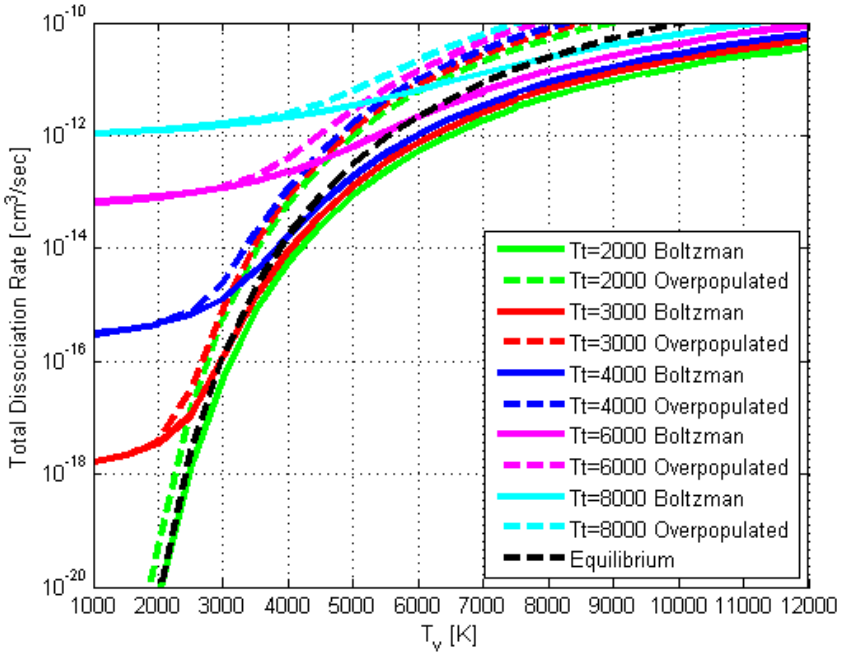

Figure 2.17: Total Dissociation Rate from QCT Analysis for an Overpopulated Boltzmann Distribution

Boltzmann distribution effects. Specifically, a scale factor of the form $(T_{v_{crit}}/T_v)^C$ is selected. This represents a temperature ratio raised to a power, where $T_{v_{crit}}$ is the critical vibrational temperature where the distribution switches from overpopulated to under populated and C is a constant parameter that controls the effect away from this critical temperature. Notionally, this scale parameter will act to increase the total dissociation rate for an overpopulated tail distribution and decrease it for an underpopulated tail distribution.

Figures 2.17 and 2.18 present the effect of both an overpopulated and underpopulated distribution. These results are used in the selection of the nonequilibrium model parameters.

The following values are selected $T_{v_{crit}}$=3500K and C=3.0 for both O_2-O and O_2-O_2 systems. The $T_{v_{crit}}$ parameter appears to be similar or be universal in some sense. These parameter values are selected with the assumption of using it for a post shock, heating type flow. Application to a cooling flow is not investigated in the presented

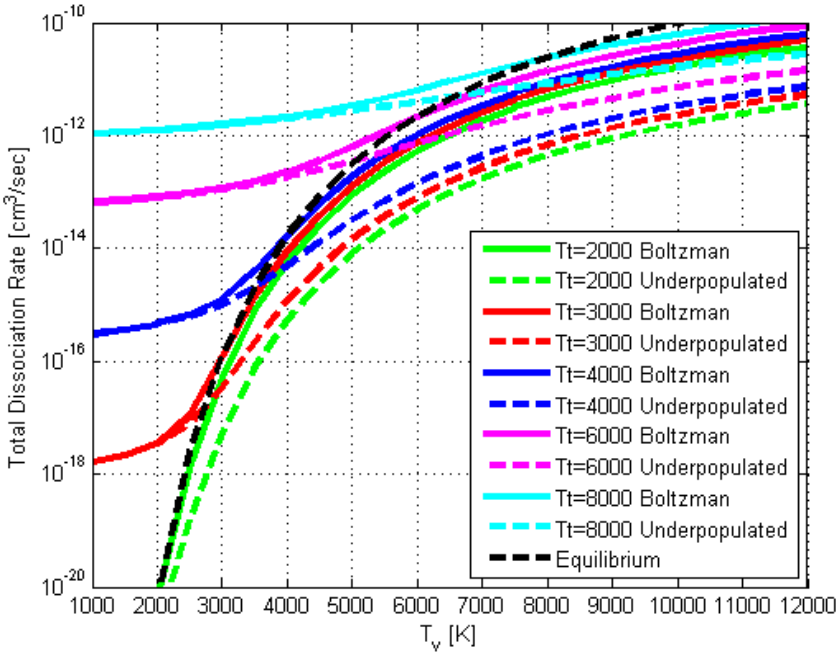

Figure 2.18: Total Dissociation Rate from QCT Analysis for an Underpopulated Boltzmann Distribution

work. The final form of the total dissociation rate is as follows.

$$K_{diss} = \left(\frac{T_{crit}}{T_v}\right)^C K_{diss,eq}(T_a) \tag{2.36}$$

2.5 Flow Modeling

The nonequilibrium modeling described above can be implemented into many different flow scenarios. The work in this thesis will focus on shock tube flows and flow over a double-cone geometry.

The shock tube flows will focus on the incident shock and reflected shock, and the consequential thermochemical relaxation that occurs behind the shock passages. There are two ways to model this shock tube flow. First, two sequential post normal shock calculations can be performed to simulate the passage of the incident shock and then the passage of the reflected shock. This modeling method is straightforward

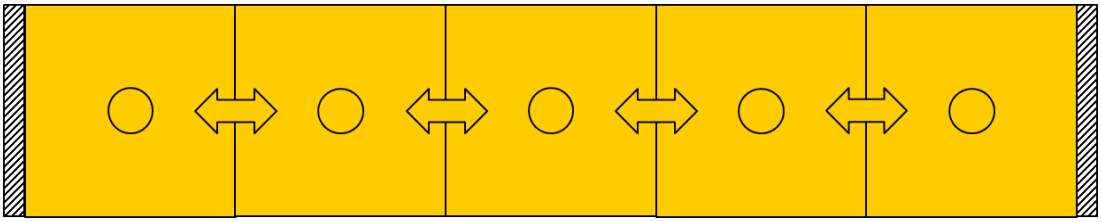

Figure 2.19: Unsteady Solver Grid Setup

and computationally efficient. However, it does require some assumptions about the flow properties in the shock tube regions. Primarily, that the shock wave is not curved due to nonuniform region flow properties in the shock tube flow. This is not necessarily true for flows with nonequilibrium behavior. The flow properties could be quite different due to the nonequilibrium behavior, and lead to curved shocks. Second, a 1D unsteady CFD solver can be used to model the shock tube behavior. The unsteady solver has no assumption about the shocks or region flow properties. The drawback is that the unsteady solver is more computationally expensive.

The following section presents the details of the unsteady solver and assesses the validity of the assumptions made in the sequential post normal shock methodology.

2.5.1 Unsteady Flow Solver

The unsteady shock tube flow solver evolves the 1D Euler equations with multi-species chemistry and nonequilibrium behavior (2T) in a time accurate fashion. Figure 2.19 depicts the grid setup for the solver. The solver uses a cell-center scheme with a Roe flux function formulation. Boundary conditions for the end walls are set using a ghost cell methodology. The equations are evolved in time using a Runge-Kutta in order to retain accuracy in time, while making implementation straightforward.

The first test case is a pure Argon condition that will be used to validate the post shock conditions that can be calculated analytically (no chemistry or nonequilibrium). The high pressure section is set to 300,000 Pa and the low pressure section is set to 50,000 Pa. Both sections have a temperature of 298K. The shock tube is 1 meter

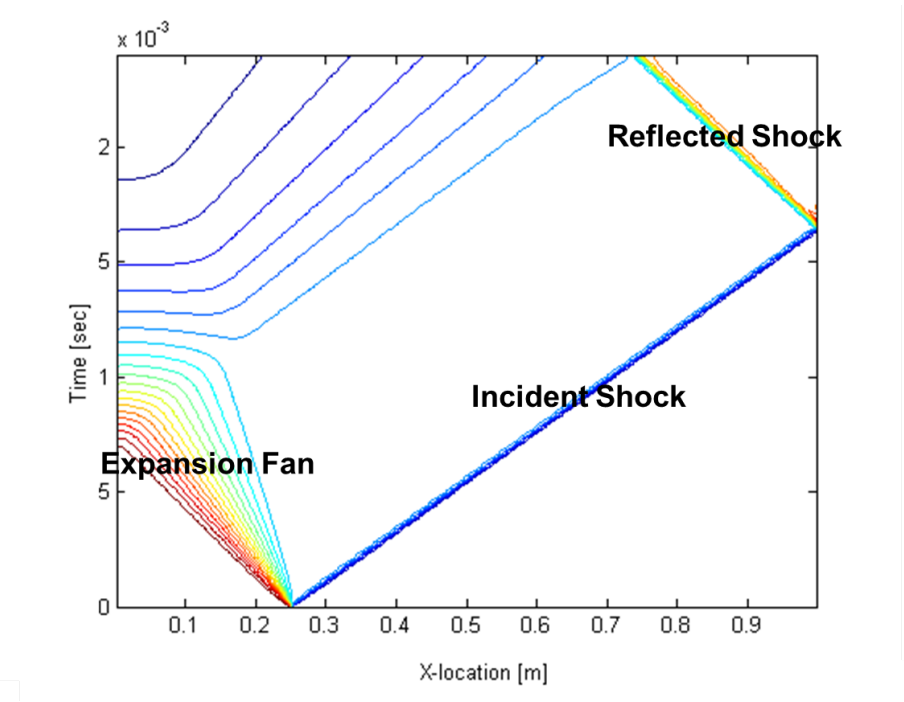

Figure 2.20: Pressure Contours for Shock Tube Flow: Argon

long, with the diaphragm set at the 0.25 location. The shock tube was divided into 200 cells and the solution run for 300 time steps. Figure 2.20 displays the pressure contours for the solution.

Figure 2.21 compares the unsteady solver results with the analytical solution. The comparison is good, and confirms the performance of the unsteady flow solver.

Figures 2.22 and 2.23 present results for a pure oxygen setup condition that leads to shock curvature near the end wall. The results show that the nonequilibrium behavior is strong enough to change the strength of the shock.

The unsteady solver has been shown to be able to simulate shock tube flows and capture shock curvature due to nonequilibrium behavior. The next simulation compares the results of the unsteady solver with the two sequential post shock calculations approach. The condition used is designated Run 109. Experimental data is also available from Stanford [32] for this condition. The condition is a 98% Argon / 2% Oxygen mixture with a starting temperature of 298K and an incident shock Mach

	Analytical	Unsteady Solver
P_2	112,877 Pa	112,915 Pa
T_2	419.7 K	419.8 K
U_2	171.2 m/s	171.3 m/s
P_5	226,297 Pa	226,450 Pa
T_5	560.2 K	560.4 K

Figure 2.21: Comparison between Unsteady Simulation and Analytical Solution

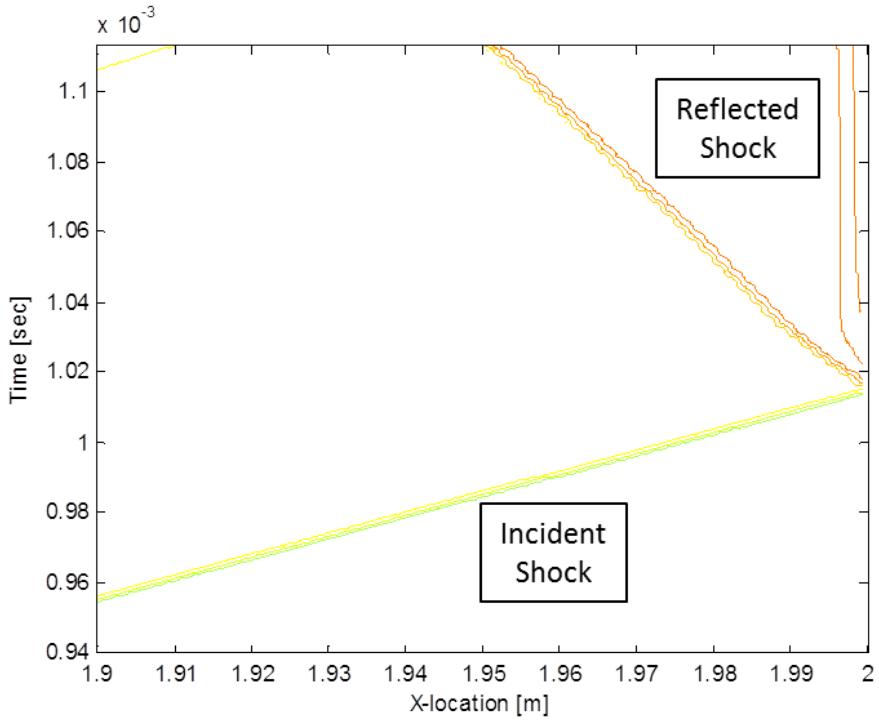

Figure 2.22: Pressure Contours for Shock Reflection at Shock Tube End Wall

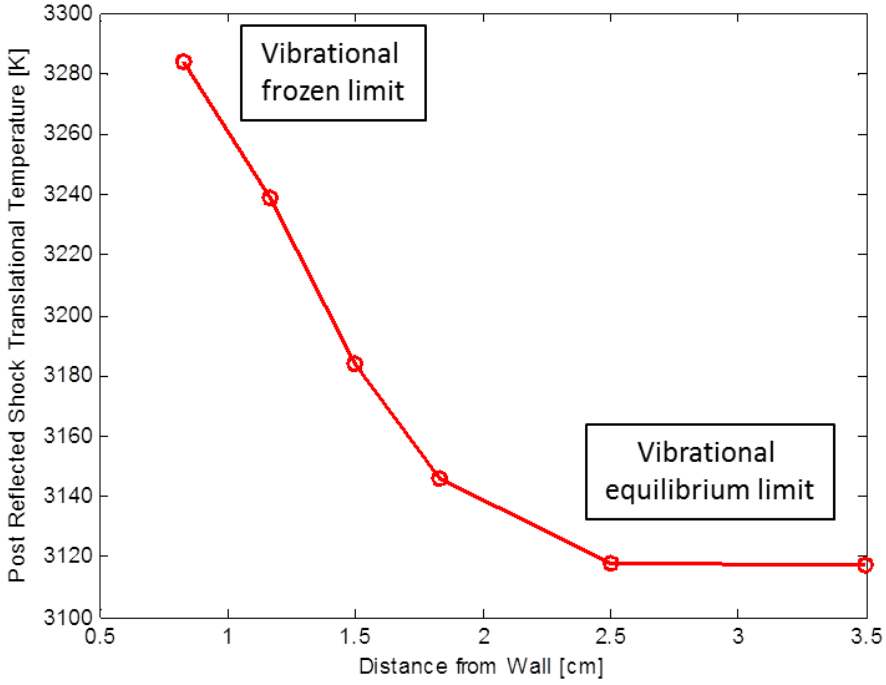

Figure 2.23: Post Reflected Shock Temperature Near End Wall

number of 3.57 Figure 2.24 shows the results for the experiment, two sequential post shock calculations (steady), and the unsteady solver (CFD). The results between the two solver methods are almost indistinguishable. This is a positive result by showing that the two sequential post normal shock calculation approach is accurate even with its assumptions. The shock tube calculations for the rest of the thesis work will utilize the sequential post normal shock approach.

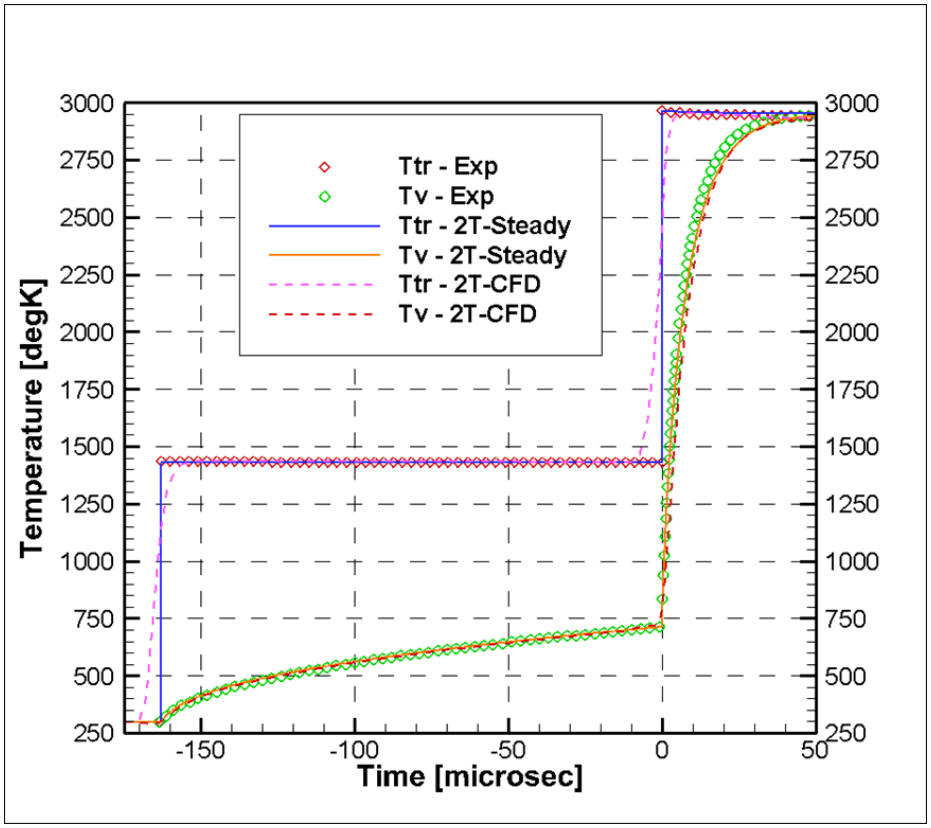

Figure 2.24: Flow Solver Comparison: Run 109

CHAPTER III

Oxygen-Argon Mixture Shock Tube Studies

An important goal of this dissertation is to compare numerical results to experimental measurements in order to assess the physical accuracy of the computational modeling methods in predicting the nonequilibrium behavior of conditions similar to those experienced in hypersonic flight. The numerical simulations can provide valuable understanding about how the nonequilibrium behavior (vibrational relaxation, dissociation, etc.) effects the flow field properties and their impact on a flight vehicle. However, due to the complexity of these flows and limited amount of experimental data, it is vital to first gain understand about the modeling fidelity required to accurately capture the physical behavior observed in experimental measurements. Additionally, the current computational capability does not allow high fidelity nonequilibrium modeling (STS) to be used for practical, 3D design efforts. The modeling fidelity comparison with experimental measurement is needed to ensure efficient use of computational resources in practical design efforts.

Therefore, this chapter compares the numerical results and experimental measurements for a post normal shock tube setup for conditions that will be encountered in hypersonic flight. The chapter first provides an overview of the experimental data available for hypersonic flows containing oxygen. The chapter then provides a brief description of the experimental method and presents the specific experimental cases

that will be used for comparison study. Next, the chapter presents comparisons between experimental measurements and numerical results for 2T and STS methods, and interrogating various aspects of nonequilibrium behavior including vibrational-translational relaxation and dissociation. The previously described reduced order model from this dissertation is then compared to the widely used 2T model and the STS model for accuracy and applicability. Finally, the chapter concludes with a summary of the important findings from the comparison study.

3.1 Experimental Data

The experimental data considered in the present study were obtained from a reflected shock tube facility at Stanford University[32]. The facility utilizes a laser absorption diagnostic for the measurements of the vibrational temperature.12 The method is based on molecular oxygen absorbance. The data collection point was 2 cm from the end wall of the shock tube. Since the absorption is the measured quantity in the facility, a model is required to recast the computational flow and thermodynamic quantities to and from absorption for direct comparison. The full details of the model and facility can be found in Ref. [33].

3.2 Computational Results and Comparisons

3.2.1 Test Case 1

The Test Case 1 conditions are chosen to focus on vibrational nonequilibrium. The mole fraction composition is 98% Argon and 2% O_2. The incident shock flow conditions are T_1=298K, P_1=7.125 torr, M_s=3.57. Figure 3 shows profiles of the translational and vibrational temperatures. Note that these quantities for the experimental data are deduced by utilizing an iterative method that matches the temperatures to the measured absorption profile by applying the absorption model described

in Ref. 13 that utilizes the measured pressure at the data collection point. The profiles show the passage of the incident shock (-165 microsec) and the subsequent vibrational relaxation (from -165 to 0 microsec). The convention of defining t = 0 at the passage of the reflected shock has been adopted.11 The vibrational relaxation after the reflected shock reaches equilibrium in approximately 50 microsec. The results reveal that all three models agree very well with each other and with the experimental data. This result is expected since the case is at relatively mild temperatures. The assumptions in the low-fidelity modeling are still valid for the test case flow conditions. Namely, Figure 3.1 shows that the vibrational population distribution remains Boltzmann during the reflected shock vibrational relaxation. It is also found that the multi-quantum transition rates are all at least one order of magnitude less than the single-quantum transition rates, and most are multiple orders of magnitude less. These findings indicate that the assumptions of the 2T approach are adequate for this relatively mild condition.

Figure 3.1 compares the vibrational state population distributions obtained directly in STS-FHO to the Boltzmann distribution that is implied by vibrational temperature solutions obtained in the 2-T approach. It is interesting to note that the STS-FHO distribution deviates from the Boltzmann distribution at higher vibrational levels during the post reflected shock relaxation before it reaches equilibrium. The temperature profiles do not show significant differences that suggest these deviations can be considered small in the sense that they do not have much influence on the overall solution. This notion can be rationalized by the fact that the deviations occur at high vibrational quantum states which have very low populations and the deviations are all less than an order of magnitude. The STS-QCT vibrational state populations show no appreciable difference from the STS-FHO results.

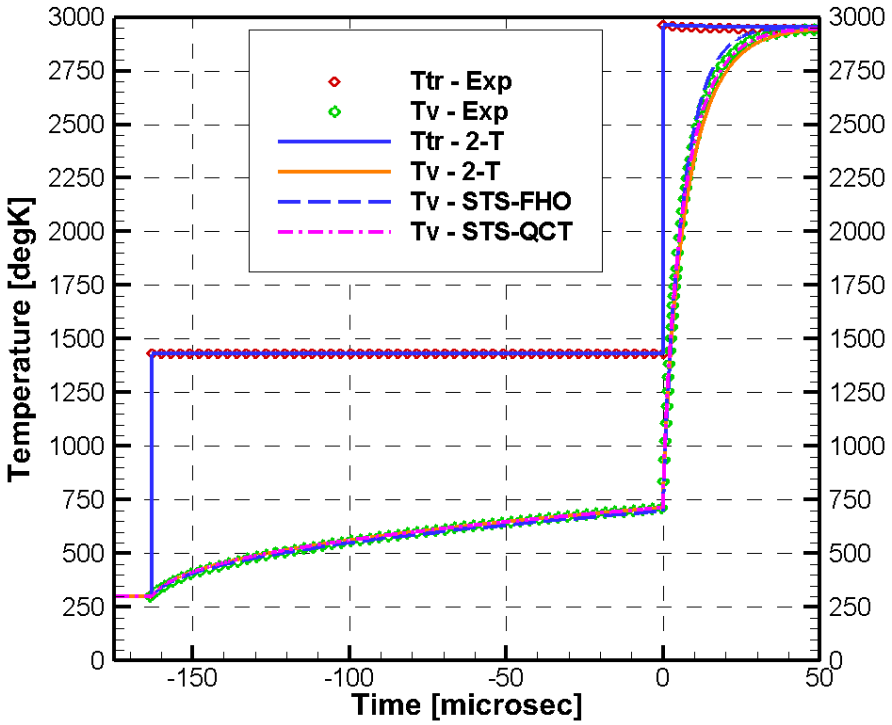

Figure 3.1: Temperature profiles obtained with different relaxation models for Test Case 1: T1=298K, P1=7.125 torr, Ms=3.57 (incident shock)

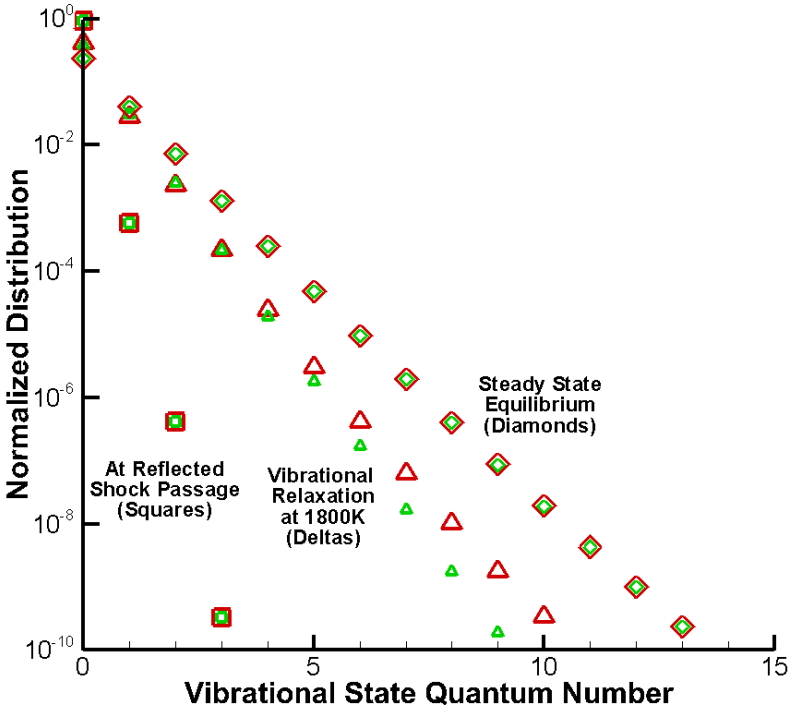

Figure 3.2: Comparison of normalized vibrational distributions for Test Case 1

3.2.2 Test Case 2

A stronger shock case is evaluated using the various thermochemical nonequilibrium models. The flow composition involves a mole fraction of 99.9% argon and 0.1% O_2. The flow conditions are T_1=295K, P_1=1.0 torr, M_s=5.9. The incident portion of the relaxation has essentially no dissociation so for clarity, this portion of the profiles is omitted to better focus on the reflected shock relaxation. Figure 3.3 shows the temperature behavior following the reflected shock (note there is no experimental data available for this case). The case is strong enough to produce the quasi-steady state (QSS) behavior in which the rates of vibrational energy input (VT process) and vibrational energy output (dissociation) are balanced. This is the reason for the period of constant vibrational temperature part way through the relaxation process. Under these conditions, there are clear differences between the results obtained with each of the modeling methods.

Profiles of the mole fraction of the oxygen species after the reflected shock passage are shown in Figure 3.4. The results for Test Case 2 show that vibrational nonequilibrium modeling fidelity does matter for these stronger conditions. Each method reaches equilibrium at different times. These relaxation differences may be important for hypersonic vehicle analysis. Figure 3.5 compares the vibrational state population distributions obtained directly from STS-FHO and the Boltzmann distribution that is implied by the vibrational temperature solution from the 2-T approach. The STS-FHO result deviates from the Boltzmann distribution during the QSS phase of the relaxation process. The distribution deviations are an order of magnitude or more for some of the high vibrational states. It has been shown that these two models produce very different temperature profiles. The conditions of this test case are stronger and involve a large amount of dissociation. The next section aims to better understand the effects of the vibrational modeling differences and dissociation modeling differences. Figure 3.6 provides a similar comparison using the STS-QCT results.

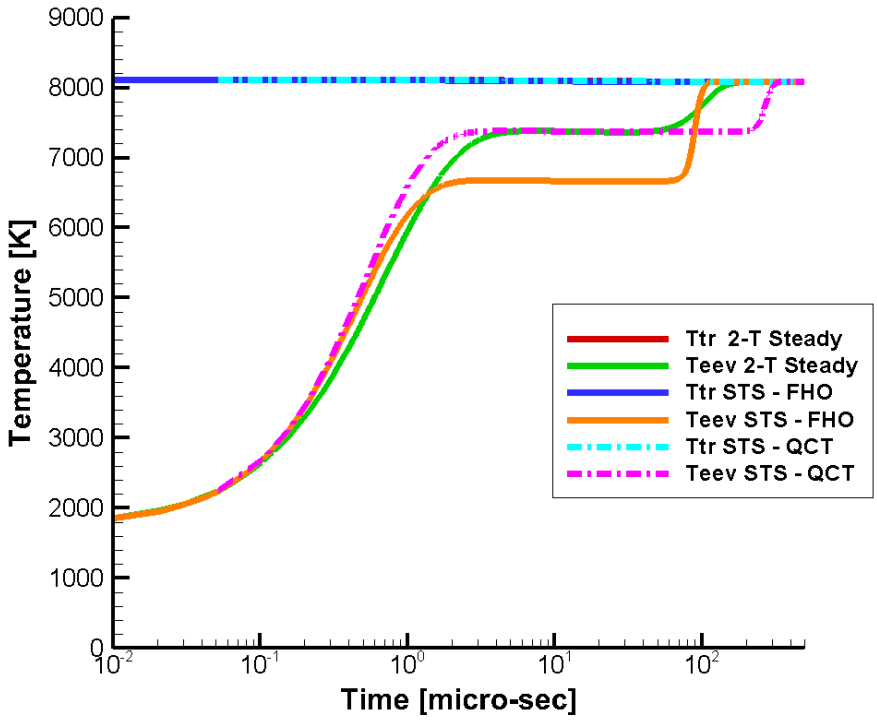

Figure 3.3: Temperature profiles obtained with different relaxation models for Test Case 2: T1=295K, P1=1.0 torr, Ms=5.9 (incident shock)

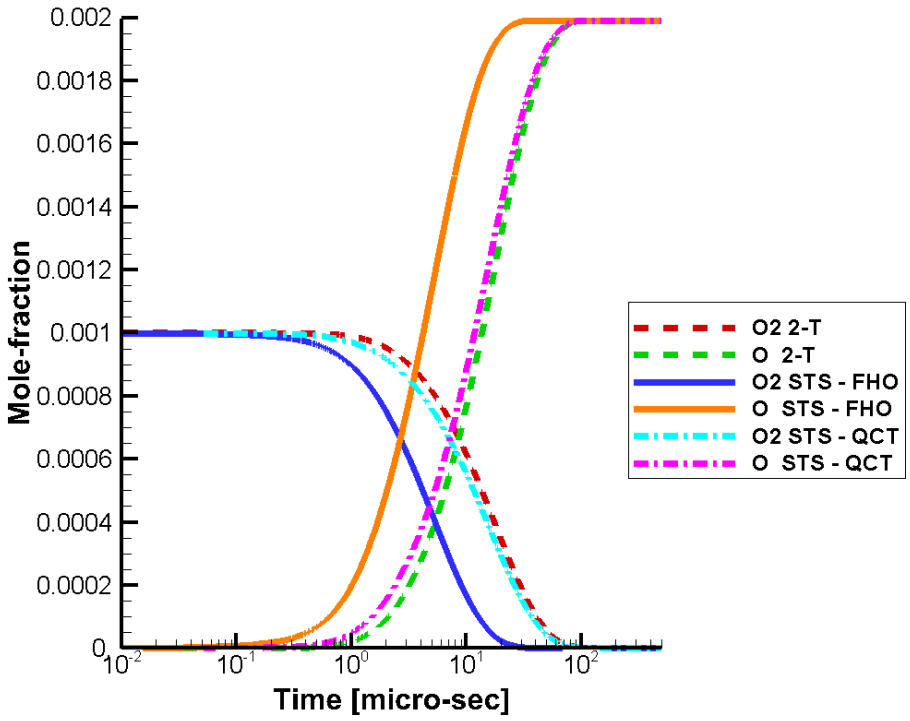

Figure 3.4: Oxygen mole-fraction profiles obtained with different relaxation models for Test Case 2: T1=295K, P1=1.0 torr, Ms=5.9 (incident shock)

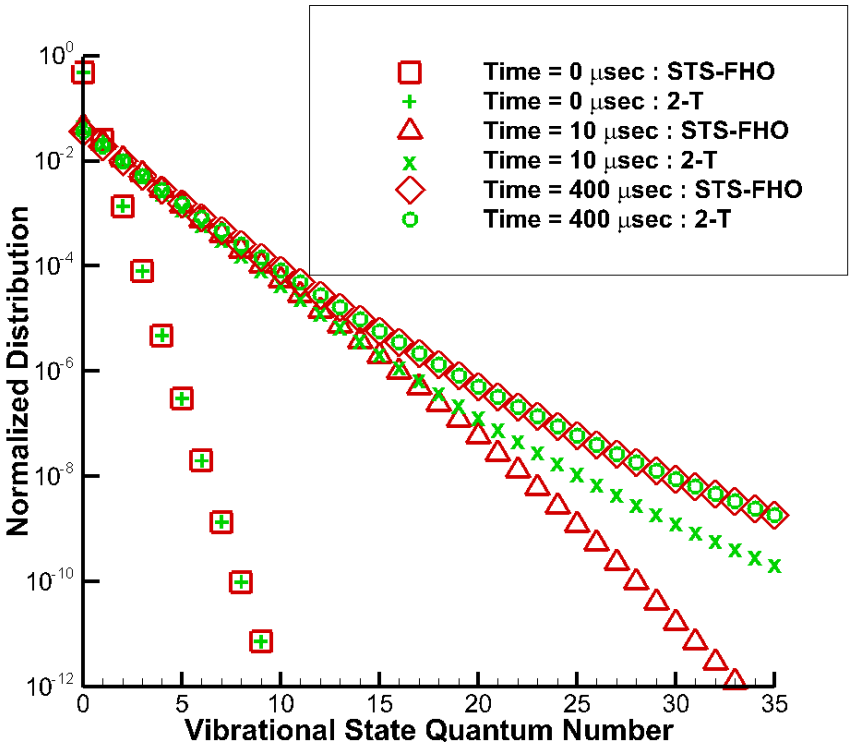

Figure 3.5: Vibrational population distribution comparison for Test Case 2 (FHO)

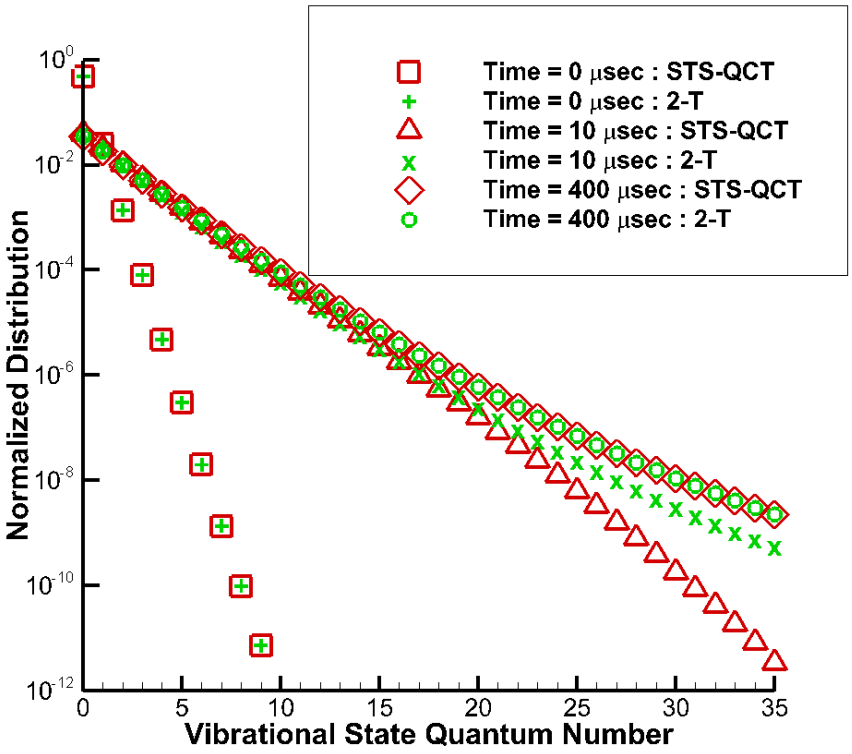

Figure 3.6: Vibrational population distribution comparison for Test Case 2 (QCT)

3.2.3 Detailed Rate Comparison

It has been shown that the models produce different results for stronger shock conditions. This section aims to investigate the differences in the vibrational and chemical modeling in order to provide an explanation for these differences. Figure 3.7 compares the vibrational relaxation parameter for each of the models employed in this study along with measurements taken from Ref. [3]. The vibrational relaxation parameter is the output of the Millikan-White curve fit, but must be calculated for the state-resolved approaches. The calculation of the vibrational relaxation parameter is performed through a master equation analysis using the state-to-state rates. The master equation analysis gives the evolution of vibrational energy over time. This information can then be recast as a relaxation parameter through the use of the Landau-Teller equation. As would be expected, the vibrational relaxation parameter values are very similar for lower temperatures where all of the assumptions for the models are valid. As the temperature increases (to the left), the rates obtained by the various models begin to deviate, and this is due to some of the assumptions becoming invalid. For example, around 4500K, multi-quantum transitions become more prevalent. The assumption of single-quantum transitions within the Landau-Teller formulation using the Millikan-White rates causes those results to begin deviating from the actual physics. The Millikan-White rates that are used in the 2-T model are shown in two forms: (1) the original Millikan-White rates; and (2) the rate that includes the high temperature correction that was suggested by Park.1 The correction has proven to be effective for other species interactions. However, the standard correction appears to not be adequate for the O_2-Ar interaction. Since this is an empirically based correction, there may be an opportunity to develop a better correction factor for this system. The STS-QCT model is considered the highest fidelity, and thus most accurate model investigated.

In order to fully isolate the VT modeling, chemistry is omitted in the following

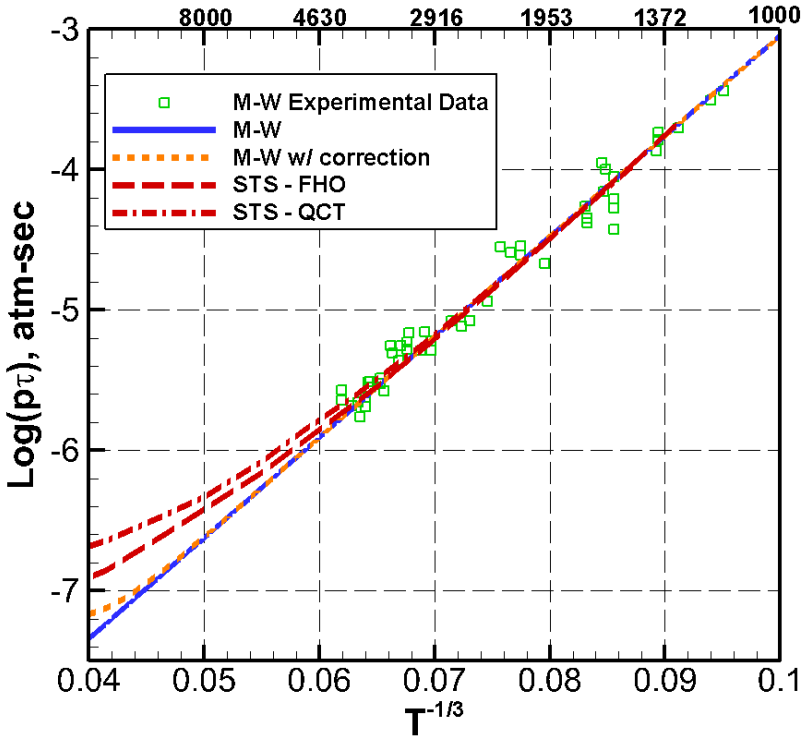

Figure 3.7: Vibrational relaxation parameter as a function of temperature

results for Test Case 2. Figure 3.8 shows the comparison of the models for vibrational temperature. The time scale has been normalized by the 2T relaxation time to QSS from the case that includes chemistry. The normalization aims to compare the effect of ignoring chemistry. Also, it highlights that this portion of the study is focused on model comparison, not physical accuracy of the time scale since chemistry is ignored. Figure 3.8 shows that there is a fundamental difference in the initial VT process between the QCT method and the other two models, 2T and FHO. The QCT method shows a delay in the VT process initially. Park[34] provided a possible physical explanation due to the initial vibrational state rate behavior just after a shock wave. The behavior is a combination of ladder-climbing through the vibrational states and multi-level transition processes. Park described the use of a diffusion factor in the 2T model, right after a shock wave, to account for those initial population and transition effects. An STS model does not require the use of this type of factor because the populations are accounted for explicitly. Figure 3.8 shows that the FHO model and QCT model have differences in this initial behavior, and thus, at least hypothetically, have a modeling difference in the ladder-climbing and multi-level transition behavior immediately after a shock. The detailed explanation of this difference is discussed in the following section.

In addition to initial behavior differences, the time to reach equilibrium differs between the models. Specifically, the time to equilibrium of the 2T model is slower and the relaxation profile is more uniform than the STS models. This difference is likely due to the ability of the STS models to capture non-Boltzmann behavior and account for multi-level transitions. The 2T model assumes a Boltzmann distribution and single quantum transitions. These modeling assumptions of the 2T model lead to more gradual changes in the slope of the temperature profile shown in Figure 3.8.

In addition to investigating only the VT transfer process, it is also useful to consider the effect of the chemistry modeling. Figure 3.9 compares the rates of vibrational

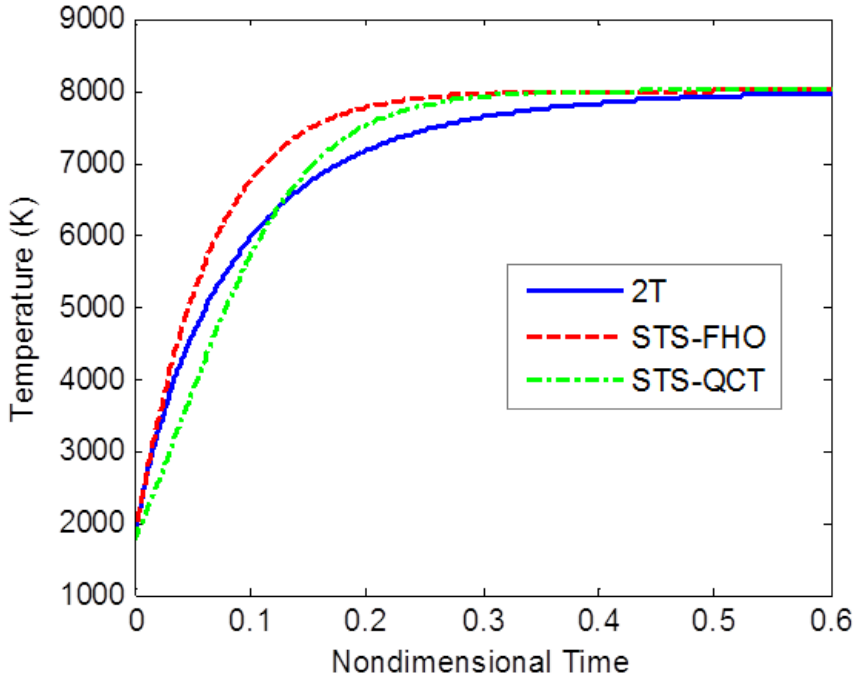

Figure 3.8: Profiles of vibrational temperature for Test Case 2 in the absence of chemistry

energy lost through dissociation as predicted by each of the methods for Test Case 2 including chemistry in which a significant amount of composition change occurs.

The profile from the STS-FHO model stands out as predicting a significantly higher rate of energy removal compared to the other models. This behavior explains the difference in vibrational temperature profiles seen in Figure 3.3 in which STS-FHO predicts lower Tv in the QSS period than the other models. However, the vibrational relaxation parameters agree within 10% for the STS-QCT and STS-FHO models at this temperature as shown in Fig. 3.7. This suggests that the vastly different QSS behavior arises not from the vibrational relaxation modeling, but rather from differences in the bound-free rates. Figure 3.10 compares the QSS dissociation rates for the various models. At the Test Case 2 conditions, the QCT rate is a factor of 2 and the FHO (Esposito) rate is almost a full order of magnitude larger than the 2T (Arrhenius) rate. This supports the notion that the difference in QSS

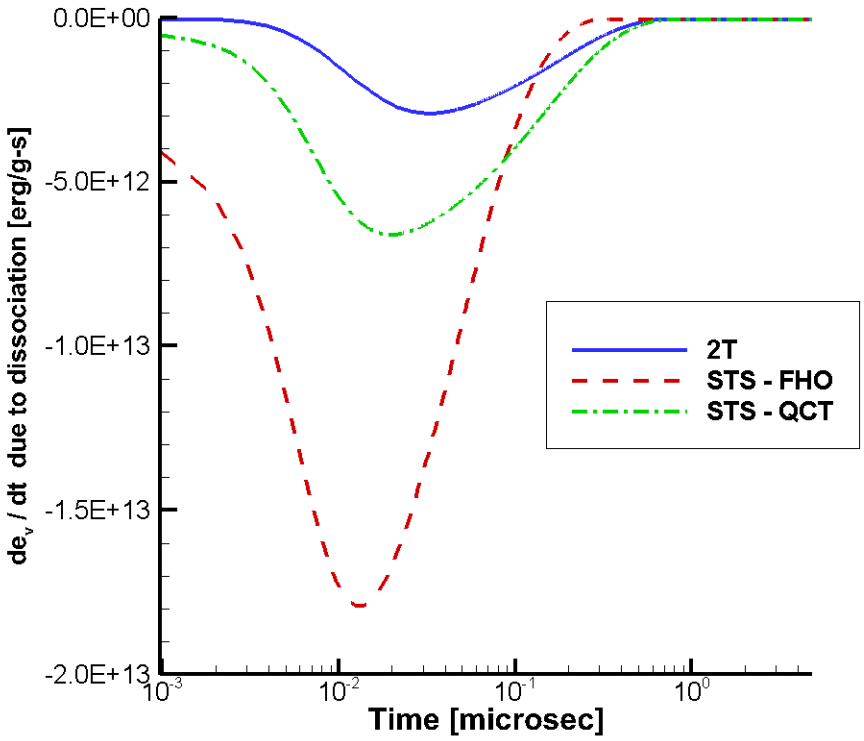

Figure 3.9: Rates of vibrational energy lost through dissociation (Test Case 2)

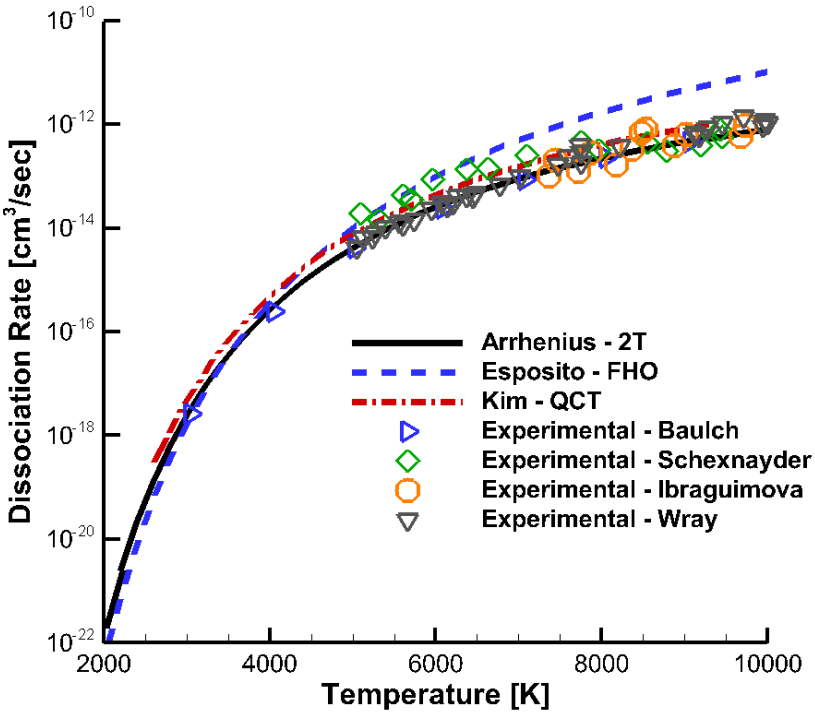

Figure 3.10: QSS dissociation rate as a function of temperature for O_2-Ar with experimental data sets

behavior for Test Case 2 is driven primarily by the differences in the bound-free rate behavior of the models. Figure 3.10 also compares the models with several experimental data sets.20-25 There is a variation in the experimental data sets of a factor of 2-5. The 2T (Arrhenius) and QCT (Kim) models agree with the experimental data sets over the entire range. The FHO (Esposito) agrees with the data up to 6000 K, and then deviates at higher temperature. This deviation suggests that the temperature correction factor applied to the Esposito rates does not properly capture the temperature dependent behavior.

3.2.4 Detailed State-to-State Rate Comparison

The previous section has shown that the models have different vibrational-translational transfer behavior. This section aims to compare the state-to-state (STS) rate behavior

of the models and the sensitivity to the macroscopic flow behavior that has previously been discussed. The focus of the investigation will be on the STS models (STS-FHO and STS-QCT). However, STS rates are also shown for the 2T model for reference. The STS rates for the 2T model are obtained by applying the underlying assumptions of the model and the consequential rate relations. Namely, the assumptions that directly lead to the rate relations are harmonic oscillator energy levels and only single quantum transitions occur. Specific rate relations can be found in Ref. [20].

The STS rate space is three-dimensional in the sense that there is a rate for each independent initial state and final state pair. Figures 3.11 through 3.14 compare the net STS rates for the QCT and FHO models at 5,000K and 10,000K, respectively. These net rates of each vibrational state are weighted by the equilibrium population fraction for the relevant states (see Eq. 3.1).

$$(k_i) = \frac{1}{Q_{total}} \sum_j \left(Q_j k_{j\to i} - Q_i k_{i\to j}\right) \tag{3.1}$$

This weighted net STS rate aims to capture the behavior differences of the models relative to how it will affect the macroscale solution. The macroscale solution will be determined by the STS rates and the populations of each state. Two versions of the FHO model are shown in the figures in order to demonstrate the role of multi-quantum transitions. FHO (5) considers quantum transition up to 5, while FHO (20) considers quantum transition up to 20. Figures 3.11 and 3.12 show that the models agree to around vibrational quantum number 7. At 5,000K, the majority of the vibrational state population is in these low vibrational states. This explains why the models do not show a macroscale difference in the vibrational relaxation for Test Case 1 shown previously. The net STS rate model differences that are shown above vibrational quantum state 7 can essentially be neglected because of the low populations in those states at 5,000K. Additionally, the FHO (5) and FHO (20) models do not deviate until above vibrational state 20. This shows that multi-quantum transitions beyond

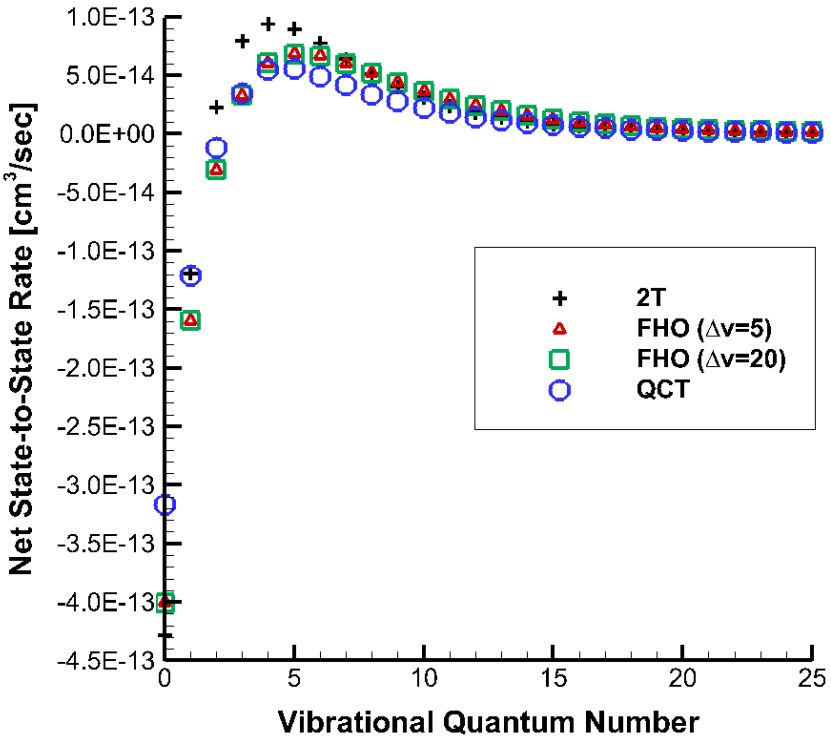

Figure 3.11: Net STS rate comparison at 5,000K for O_2-Ar: v = 0-30

5 are almost non-existent at this temperature. Figures 3.13 and 3.14 show the net STS rates for 10,000K and illustrates the higher temperature behavior. The differences between the models occur at lower vibrational quantum numbers. These net STS rate differences support the behavior differences shown in Test Case 2 (Figure 3.8). The FHO and QCT models show fundamentally different profile shapes for the net STS rate. This difference in STS behavior helps to explain the differences shown immediately after the shock passage in Test Case 2 (Figure 3.8) since net STS rate profile shape differences will change the ladder-climbing process that occurs in this region.

Another consideration in the discussion of modeling fidelity is the sensitivity of the macroscale flow behavior to STS rate model differences. A sensitivity study is conducted for O_2-Ar in which a perturbation factor of 1.5 is applied to the STS rate

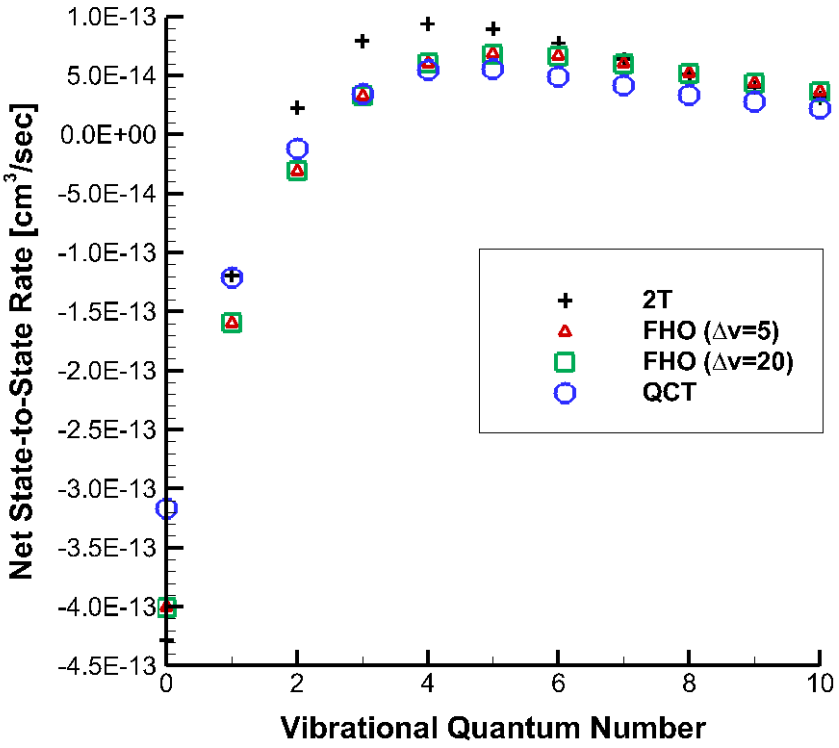

Figure 3.12: Net STS rate comparison at 5,000K for O_2-Ar: v = 0-10

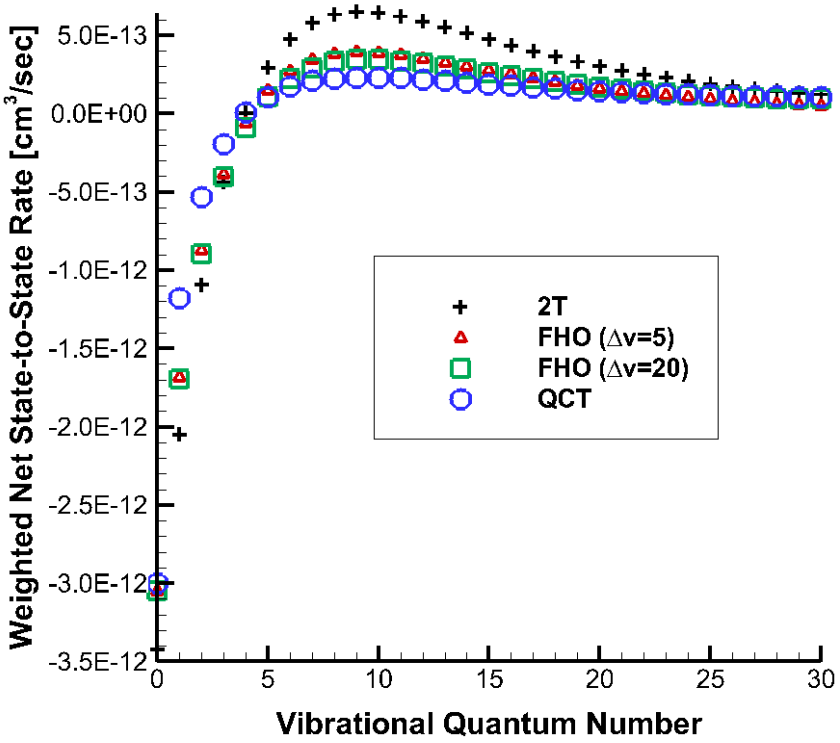

Figure 3.13: Net STS rate comparison at 10,000K for O_2-Ar: v = 0-30

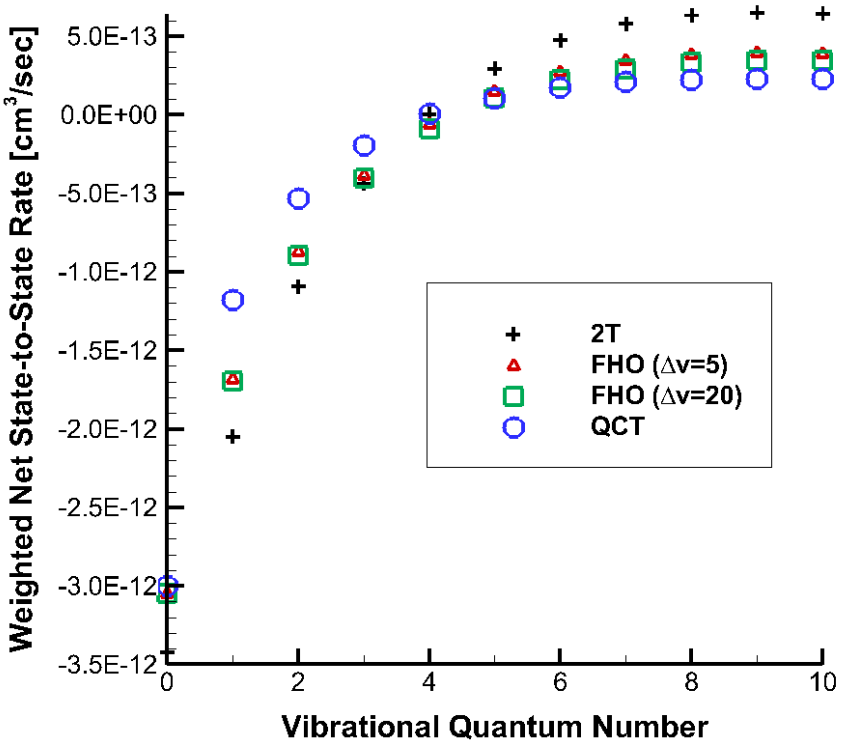

Figure 3.14: Net STS rate comparison at 10,000K for O_2-Ar: v = 0-10

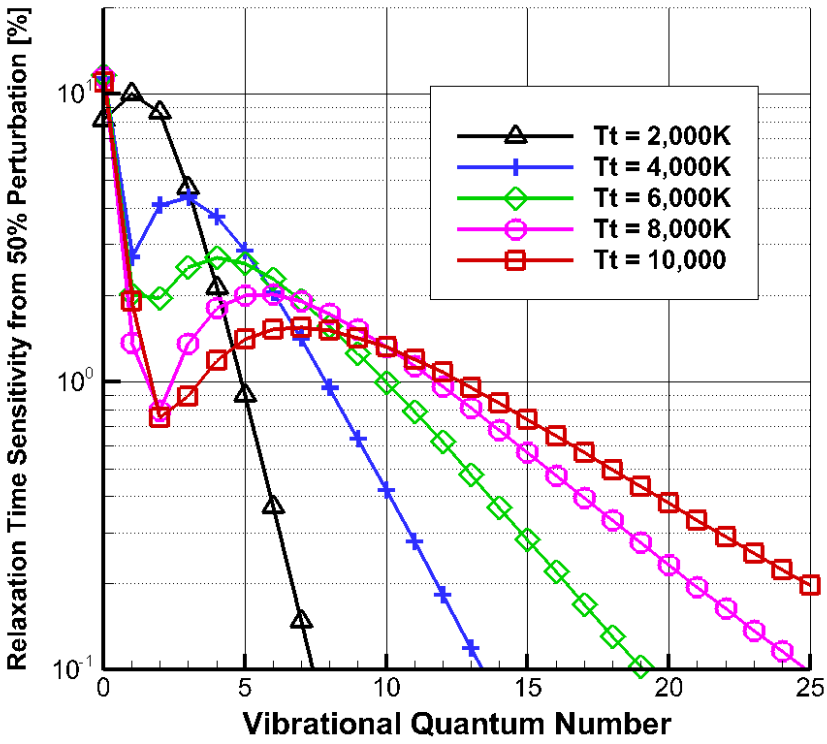

Figure 3.15: Macroscale time to equilibrium sensitivity due to a STS rate perturbation of 50% for O_2-Ar

(a 50% increase in the STS rate magnitude) for each vibrational state independently, and the resulting change in macroscale behavior is evaluated. For this study, the time to equilibrium is the metric used to characterize macroscale behavior. The time to equilibrium is defined as the time for the vibrational temperature to reach 99% of the equilibrium value. The relaxation process is simulated using a master equation analysis for a highly dilute mixture (1% O_2 / 99% Ar). The initial vibrational population is set as a Boltzmann distribution at a temperature of 300K. The perturbation analysis is evaluated at 5 different temperatures from 2,000K to 10,000K and the STS-FHO (v=20) rates are used as the nominal STS rates. Figure 3.15 shows the results of this sensitivity study for O_2-Ar.

The results show that vibrational state 0 is the most sensitive to this perturbation and is rather uniform across the temperature range. Essentially, a 50% perturbation

increase in the STS rate magnitude (v=0) results in a 10% change in the macroscale behavior. In other words, if there is a 50% error/uncertainty in the v=0 STS rate, it would translate into a 10% error/uncertainty in the macroscale solution accuracy. The sensitivity study shows that as the temperature increases, the macroscale accuracy becomes more sensitive to the higher vibrational states (greater than 10). Additionally, a rapid change in sensitivity is observed around the v=1-2 range. This is due to the fact that the STS rate value crosses through zero in this range. That fact leads to a dip in the sensitivity of the macroscale solution to those vibrational quantum states. These results, in concert with the net STS rate comparisons, begin to give a guideline for modeling fidelity requirements. Further sensitivity studies will aim to provide specific guidelines. For example, if a 1% accuracy is desired for the macroscale flow behavior, the STS rate model will need to capture STS rates to a certain accuracy based on the temperature of the case.

3.3 Summary

In the present chapter, three different levels of fidelity in vibrational nonequilibrium modeling of the O_2-Ar system are investigated. The three levels of fidelity are the two temperature model, a state-resolved master equation with FHO state-to-state rates and Esposito bound-free rates, and a state-resolved master equation employing QCT state-to-state and bound-free rates. The results show that all levels of fidelity are adequate for mild shock conditions (for temperatures less than 4500 K). However, at stronger shock conditions, significant differences are found in the results obtained with lower and higher fidelity modeling. The presented results show that the pure vibrational relaxation behavior is similar for FHO and QCT state-to-state rates. However, the FHO model does not appear to correctly capture the initial behavior immediately after a shock wave. A net STS rate study shows that the QCT and FHO models have a fundamental difference that would explain the behavior im-

mediately after a shock wave. The presented STS rate sensitivity study shows the connection between the STS rates and the macroscale flow behavior. Also, the state-resolved method exhibits approximately an order of magnitude higher computational cost compared to the standard two-temperature approach.

CHAPTER IV

Pure Oxygen Shock Tube Studies

This chapter presents the investigation of O_2-O_2 post normal shock behavior and modeling. First, a background is presented on the unique aspects of the oxygen system for nonequilibrium. Next, the application of the two-temperature model and state-to-state model are presented. Additionally, a modification to the two-temperature model is proposed with the goal of improving the modeling accuracy while staying within the 2T framework. The chapter will then present the details of the experimental measurements and continue by comparing the numerical results with the experimental data. Finally, the chapter will concluded with a summary of the key findings and conclusions.

4.1 Experimental Data Overview

Recently, vibrational temperature behind a shock wave was measured by means of absorption spectroscopy. [35, 36, 33] In these measurements, the attenuation of intensity in the UV region of the Schumann-Runge bands of molecular oxygen was interpreted in terms of absorption coefficient that is a function of translational and vibrational temperatures of a gas mixture. Vibrational temperature profiles were obtained for the range of translational temperatures between 4,000 and 10,400 K at the incident shock velocity between 3.07 and 4.44 km/s. The flow conditions for the

test cases are summarized in Table 4.1 . All flow conditions have a pure O_2 freestream composition. The set of test cases represents a relevant range of conditions that might be experienced by hypersonic vehicles.

Test case	Shock velocity $[km/s]$	P_1 $[Torr]$	T_1 $[K]$	T_2 $[K]$	M_1 –
C1	3.07	2.0	295	5300	9.44
C2	3.95	1.0	295	8620	12.06
C3	4.44	0.8	295	10820	13.55

Table 4.1: Summary of flow conditions investigated[35, 36]

4.2 Results and Comparison

The aim of the present work is the numerical simulation of these experimental conditions using new information on O_2–O collisions that was obtained by means of a QCT study [23, 7]. The results are presented in three subsections. First, variations of the widely used 2T model are investigated. The 2T models adopt new relaxation parameters and global dissociation rates [23]. This approach is compared to the similar model with the rates previously derived for the O_2–O interaction without relying on the QCT and master equation simulations [2]. The second section presents a complete state-resolved simulation of shock wave propagation in pure oxygen. This is performed by employing the QCT rate coefficients for O_2–O interaction and the FHO model for O_2–O_2 collisions. The novelty of the present work is in the comparison of newly generated experimental data with the theoretical model incorporating high-fidelity rate coefficients derived from first principles. Finally, a reduced order model is investigated for accuracy and applicability.

4.2.1 Two-Temperature Model

The results for the 2T model are separated into two sub-sections: VT energy transfer and dissociation, and QSS dissociation rate coefficient. These sub-sections aim to isolate the various aspects of modeling that are investigated.

4.2.1.1 VT energy transfer and dissociation

First, the conventional 2T model (2T-MW/Park) is compared with the newly derived 2T QCT-derived models (2T–HH and 2T–Varandas). The models are also evaluated against the experimental results from Ref. [36].

Figures 4.1 and 4.2 show profiles of temperature and composition for the C1 case. Time begins with the passage of the shock wave. This case corresponds to mild vibrational nonequilibrium with a relatively low post-shock temperature. At these conditions vibrational relaxation occurs much faster than chemical transformation. Hence, the widely used QSS assumption about separation of these two processes is valid. All 2T models predict a similar rate of vibrational relaxation and dissociation. The mild translational temperature leads to a very small amount of atomic oxygen being present during the vibrational relaxation. At the moment of the onset of dissociation the flow contains only 2-3% of atomic oxygen and so the O_2–O_2 collisions largely dominate the vibrational relaxation behavior. Since all 2T models utilize the same MW coefficients for O_2–O_2 collisions, it is expected that they should all have similar behavior. Only slight differences are observed after 1.0μsec due to the start of dissociation, and thus the presence of atomic oxygen. It should be noted that although there are only small amounts of atomic oxygen, the much faster vibrational relaxation rates from the atomic oxygen lead to noticeable differences from the various models. The results from all models predominantly fall within the error bars of the experimental data.

Figures 4.3 and 4.4 show the temperature profiles and the composition evolution

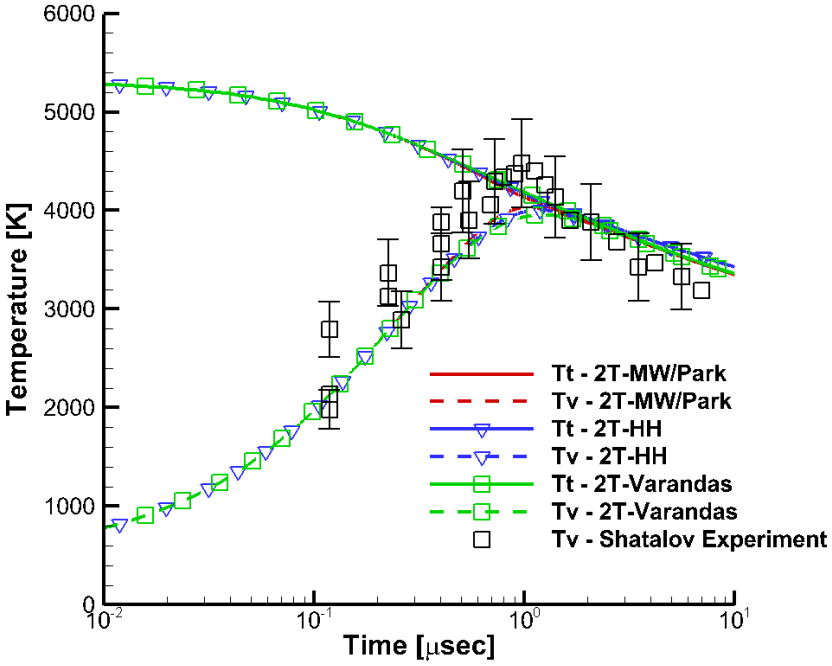

Figure 4.1: Temperature profiles, C1 case

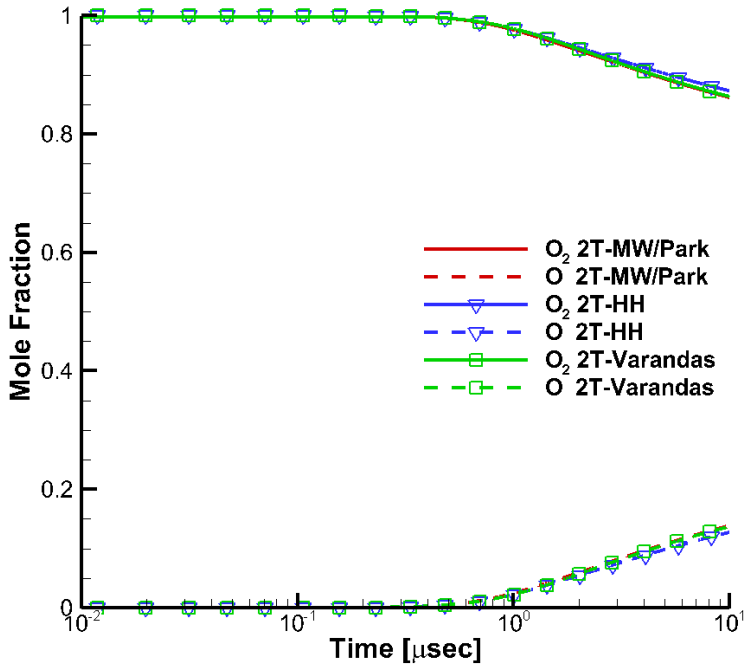

Figure 4.2: Composition profiles, C1 case

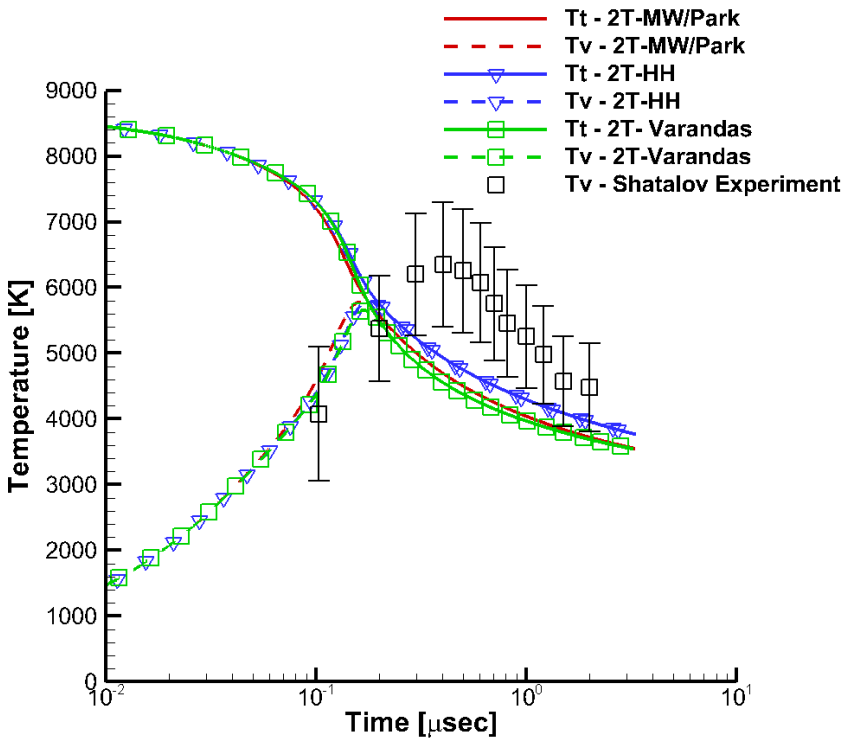

Figure 4.3: Temperature profiles, C2 case

for the slightly stronger, case C2. For this condition, there is dissociation prior to the end of vibrational relaxation. This introduces atomic oxygen in the amount of approximately 10% during vibrational relaxation, and differences are seen in the predictions of the different models. Specifically, after 0.2μsec the behavior differs significantly due to the different dissociation models. The higher fidelity 2T–Varandas model agrees better with the Park model in terms of the dissociation rate, when compared to the 2T–HH model. The first two models predict faster dissociation and, hence, a lower vibrational temperature after 0.2μsec. However, all 2T models underestimate T_v during the phase of active dissociation in the C2 case. One may conclude that the global rates incorporated in their present form in the 2T model need adjustment to match the experimental data.

The C3 case corresponds to the highest degree of nonequilibrium among the studied cases. The temperature and species profiles for the model results for C3 are shown

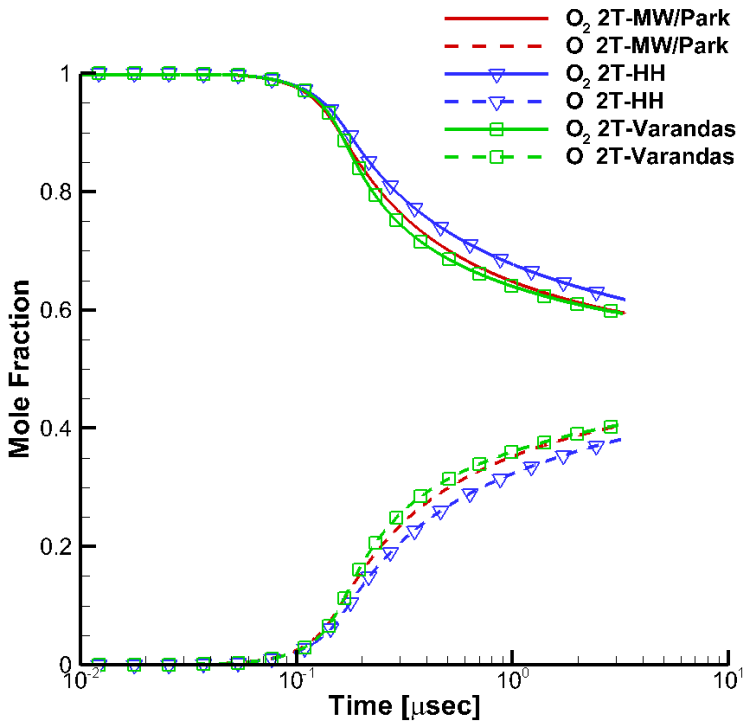

Figure 4.4: Composition profiles, C2 case

in Figures 4.5 and 4.6. All 2T models fail to accurately describe the thermal relaxation behavior. Specifically, the 2T models underestimate the experimental data. The flow contains between 15 and 20% of atomic oxygen at the moment when T and T_v become equal. From the slope of vibrational temperature, one can conclude that the location of $T = T_v$ is captured incorrectly by the 2T models. However, due to large error bars, some theoretical predictions fall within the experimental data. As in the C2 case, the 2T–Park and 2T–Varandas models predict similar rates of dissociation, and the 2T-HH model with the lower fidelity PES gives the slowest dissociation rate.

One may conclude from cases C1-C3 that the new vibrational relaxation time, generated by the QCT analysis of the O_2–O system, has little influence on vibrational temperature during the early phase of relaxation if incorporated in a low fidelity 2T model. This is not entirely surprising, since all experimental runs initially contained only pure diatomic oxygen, and the behavior will be predominately governed by O_2–

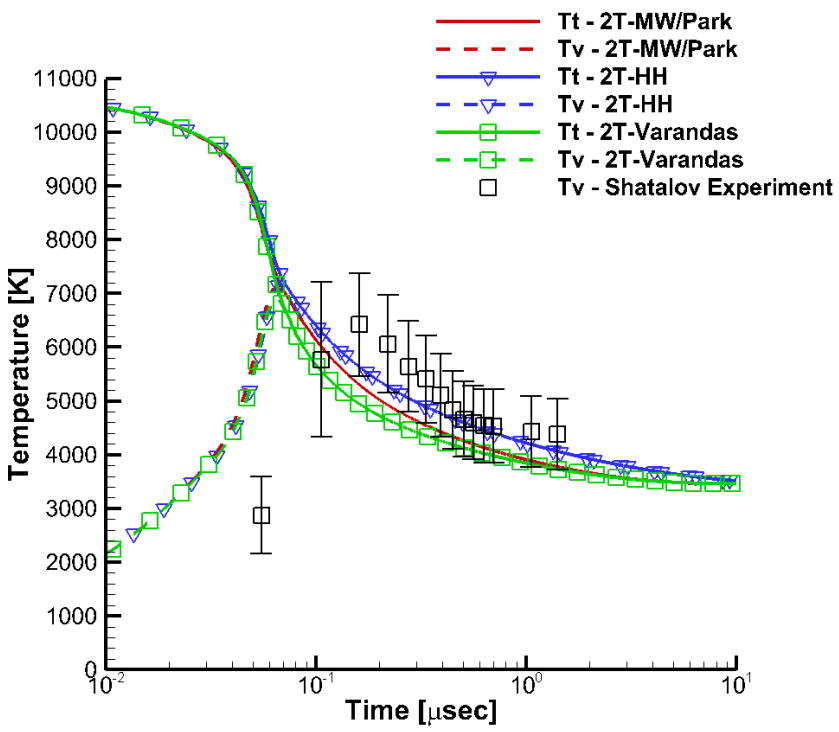

Figure 4.5: Temperature profiles, C3 case

O_2 vibrational relaxation and dissociation rates that remain unmodified. However, the importance of atomic oxygen for vibrational relaxation can be observed after dissociation begins and there is a presence of atomic oxygen. The importance of atomic oxygen is also demonstrated in Ref. [23] for cooling flows even with similar initial composition.

Additionally, it is clear that the utilization of thermal-equilibrium dissociation rate coefficients obtained from the QCT simulations with the Park model of vibration-dissociation coupling underestimate the vibrational temperature during active dissociation. This indicates that the actual, 'effective' dissociation rate should be lower than what is presently used. The following section expands discussion on this matter.

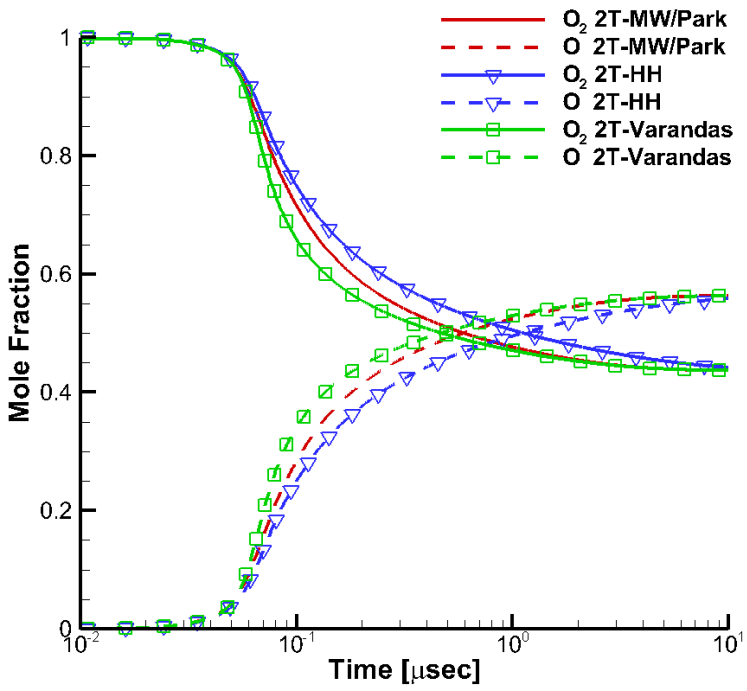

Figure 4.6: Composition profiles, C3 case

4.2.1.2 Temperature-dependent C_{VD} Investigation

Next, the effect of a temperature-dependent C_{VD} factor is investigated. The standard 2T modeling approach utilizes a constant value for C_{VD}. The constant value and temperature-dependent approaches are compared in Figures 4.7 - 4.9.

The results show that there is no accuracy difference between the temperature-dependent approach and the constant value approach for C_{VD}. However, it is suggested that the model be incorporated into current models for its physical accuracy. The approach does not affect the computational expense of the simulation, and provides a more physical representation even if the benefit of the model is not observable in these test cases.

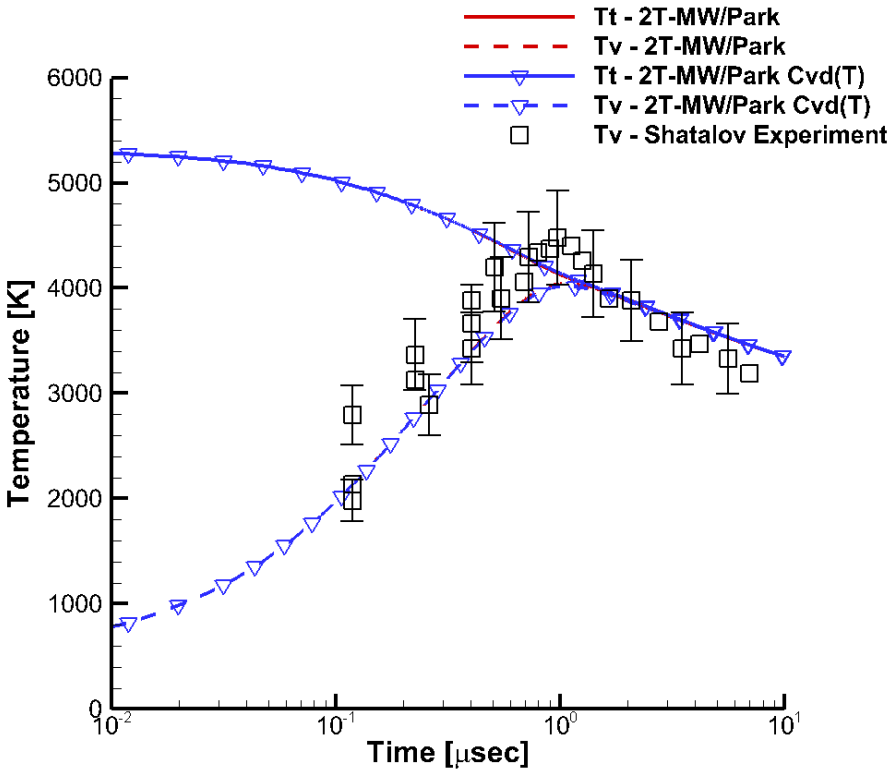

Figure 4.7: Temperature-dependent C_{VD} Influence: Case C1

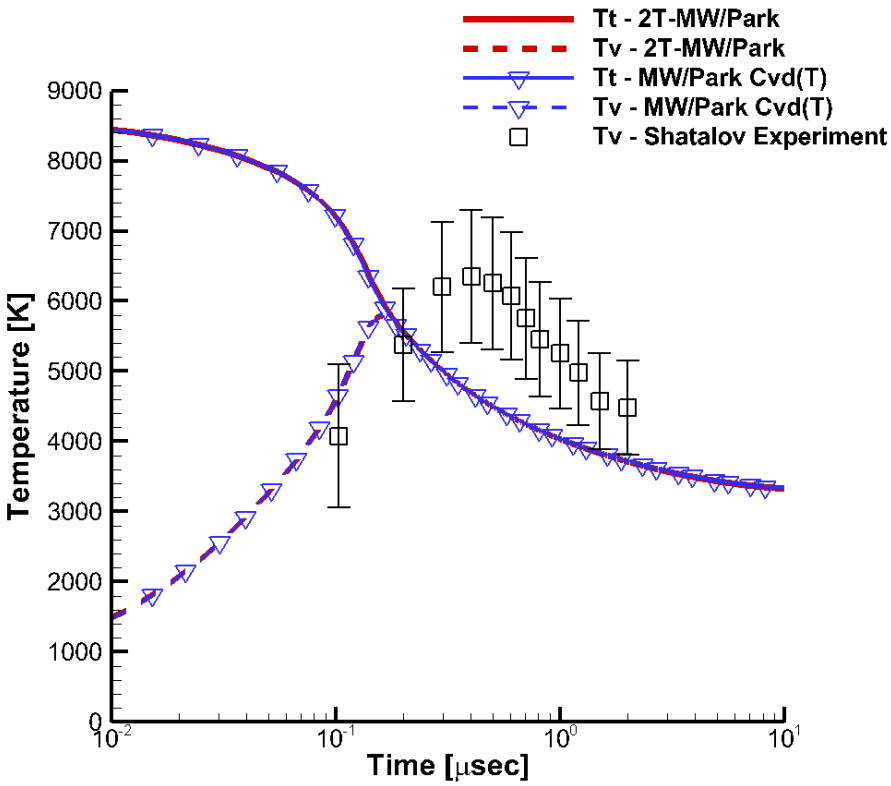

Figure 4.8: Temperature-dependent C_{VD} Influence: Case C2

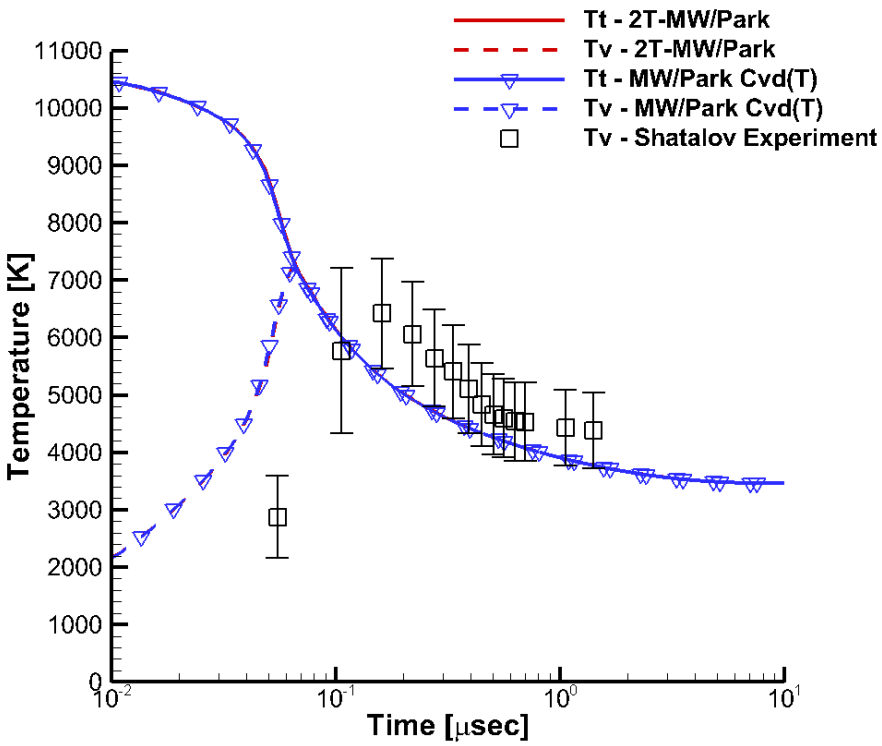

Figure 4.9: Temperature-dependent C_{VD} Influence: Case C3

4.2.1.3 QSS dissociation rate coefficient

As mentioned in the modeling description section, the work of Andrienko and Boyd [7] demonstrated that using the QSS dissociation rate coefficients could be more accurate than the equilibrium rates typically used in the 2T model. Due to the incomplete thermalization of the vibrational ladder, the dissociation rate during the QSS phase is lower than that estimated at thermal equilibrium conditions. The ratio of equilibrium and QSS rate coefficients is approximately 3 according to Park [37], however for O_2–O this ratio is found to increase rapidly at high temperature due to inefficient vibrational relaxation at these conditions. The QSS rate coefficients can be derived from the complete set of bound-bound and bound-free transition rate coefficients by solving the system of master equations with the additional constraint of $\partial n_v/\partial t = 0$.

In the present work, the effect of using the QSS dissociation rate coefficients is investigated for the experimental cases in Ref. [36]. Since the QSS dissociation rate represents the *actual* rate of depletion, no vibration-dissociation coupling, such as Park's model, is necessary.

The MW equation is used for the vibrational relaxation modeling while the two different methodologies for the dissociation rate are compared. It should be noted that the QSS rates are known only for the O_2-O system. Since well verified, high fidelity QCT rates for O_2–O_2 are presently unavailable, the QSS dissociation rate for the O_2–O_2 system is not investigated in the present work. The present work focuses on the newly available QCT rates for O_2–O.

The results for C1 are shown in Figures 4.10 and 4.11. The effect of utilizing the QSS dissociation rates for O_2–O is minimal for this test case. A slight difference in the results can be seen after 2 μsec, once a sufficient atomic number density is present in the flow field. The results are consistent with the fact that the QSS dissociation rate is less than the equilibrium dissociation rate.

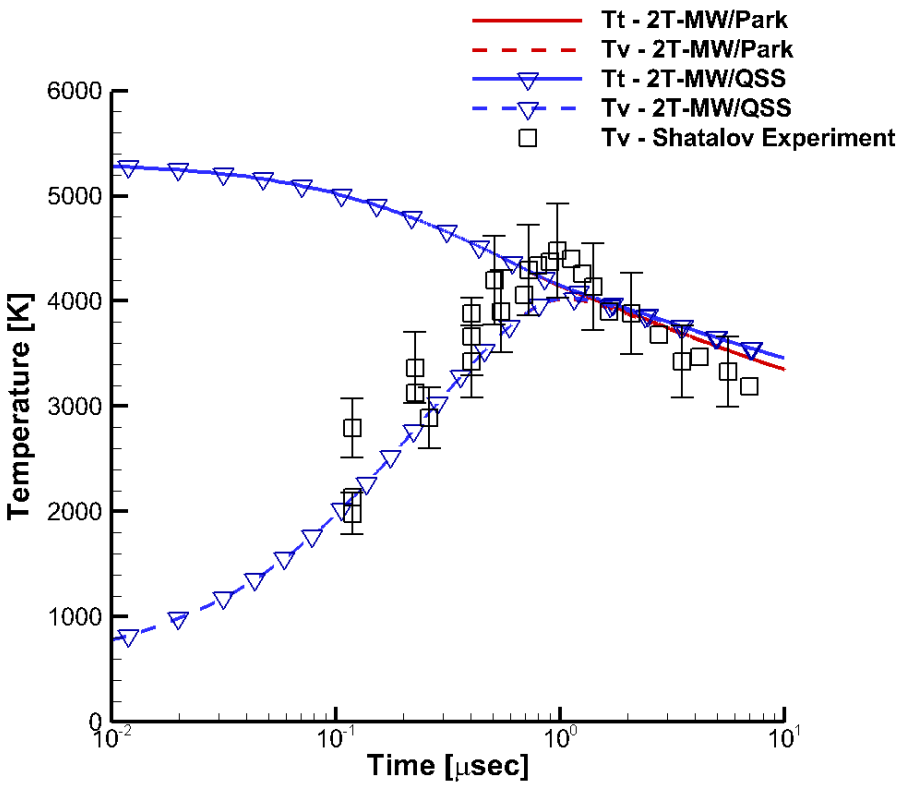

Figure 4.10: Temperature profiles, C1 case

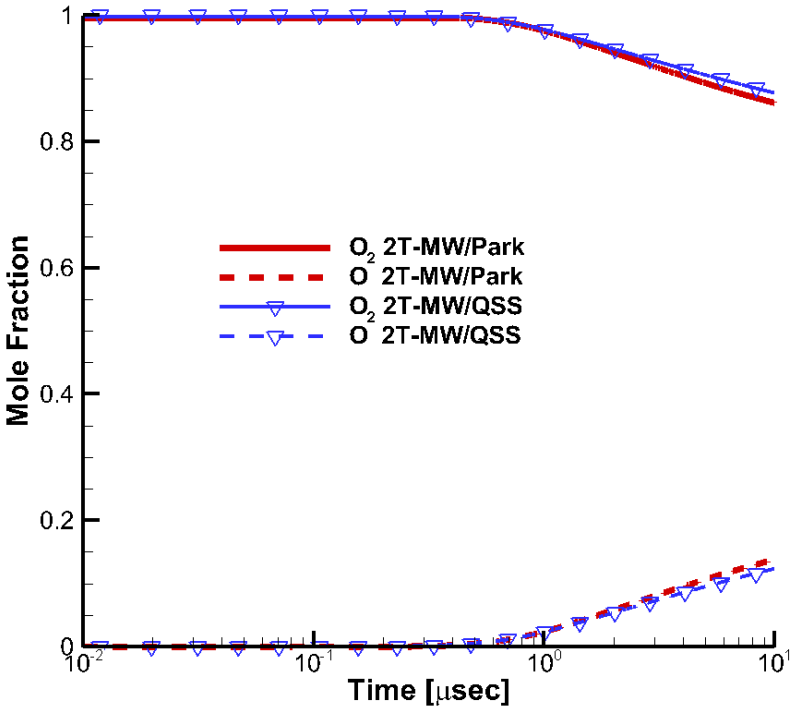

Figure 4.11: Composition profile, C1 case

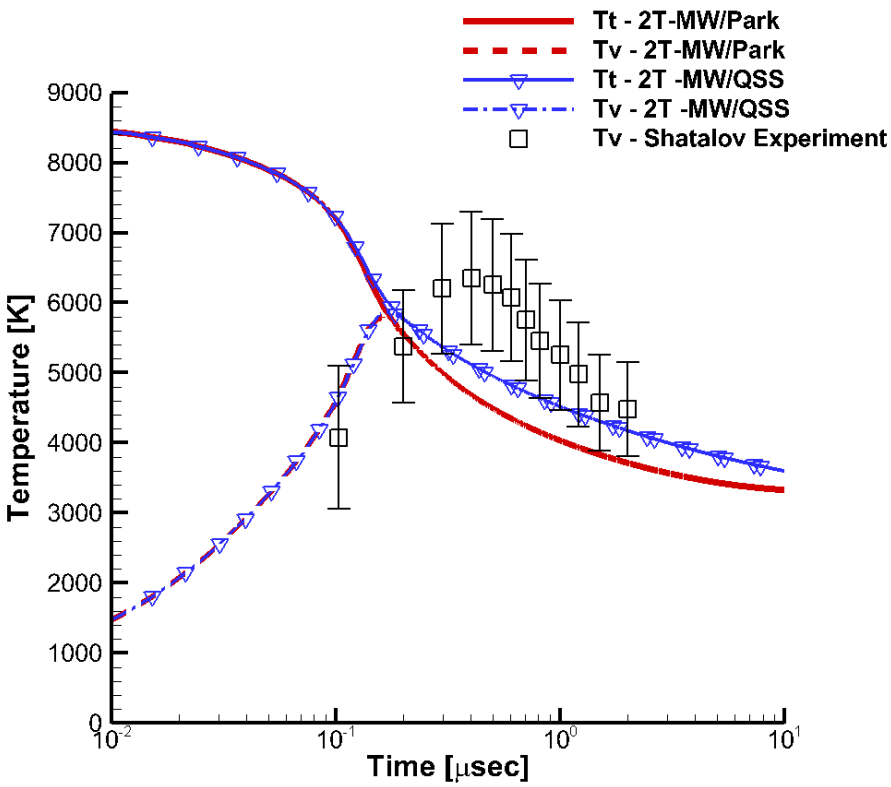

Figure 4.12: Temperature profiles, C2 case

The results for C2 are shown in Figures 4.12 and 4.13. The model with the QSS dissociation rate coefficients incorporated clearly shows the desired increase of vibrational temperature toward better agreement with the experimental data. However, even with the improvement, this QSS model still lies slightly below the error bands of the experimental data. This is due to an incorrect capturing of vibrational relaxation, that follows from the misplacement of the maximum of T_v. Specifically, the 2T models appear to reach the maximum vibrational temperature more quickly than the experimental data, leading to a different profile than the experimental results.

Figures 4.14 and 4.15 show the results for the C3 case. The QSS dissociation rate model achieves better agreement with the experimental results than the conventional 2T–Park model. The QSS approach remains within the experimental error band for the majority of the relaxation process. However, it is clear that neither of 2T models

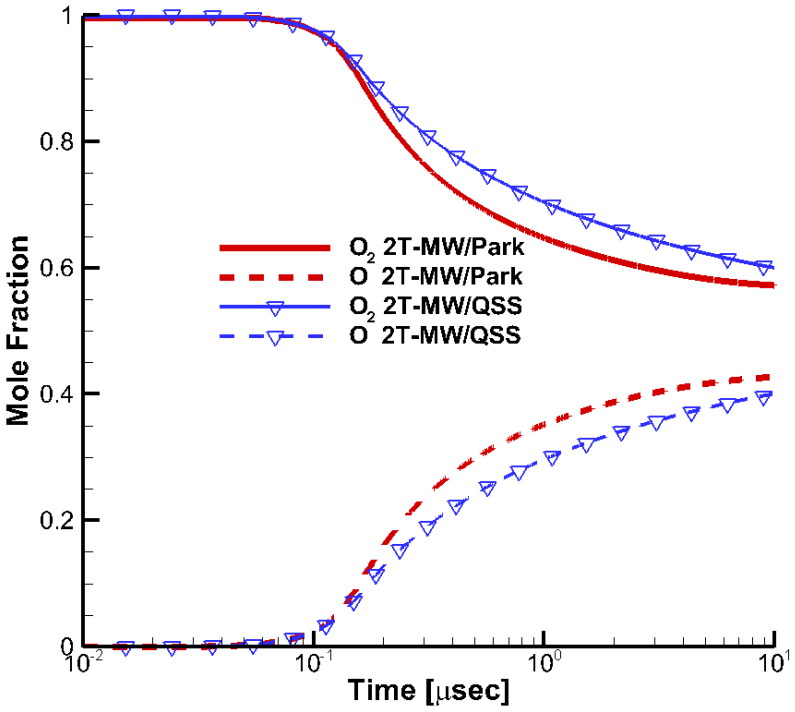

Figure 4.13: Composition profile, C2 case

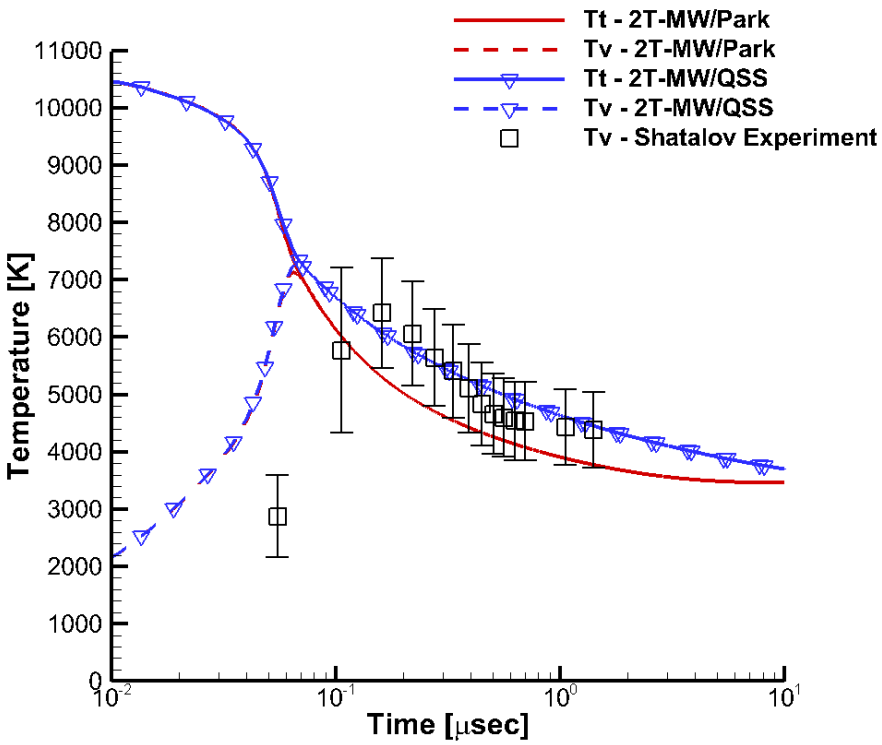

Figure 4.14: Temperature profiles, C3 case

capture the early behavior of thermalization. The vibrational relaxation for the 2T models appears to happen too rapidly at the beginning of the process.

In summary, the QSS dissociation rate coefficients provide better agreement with experimental data for these post normal shock test cases. The QSS dissociation rates described in the presented work for are for the O_2–O system. However, the 2T modeling is still not able to completely capture the behavior observed in the experimental data. Specifically, the 2T models have a difficulty capturing the maximum vibrational temperature and the location of trans-vibrational equilibrium. The following section will present the high fidelity STS results. This will provide additional insight into the deficiencies of the 2T modeling for accurately capturing nonequilibrium behavior.

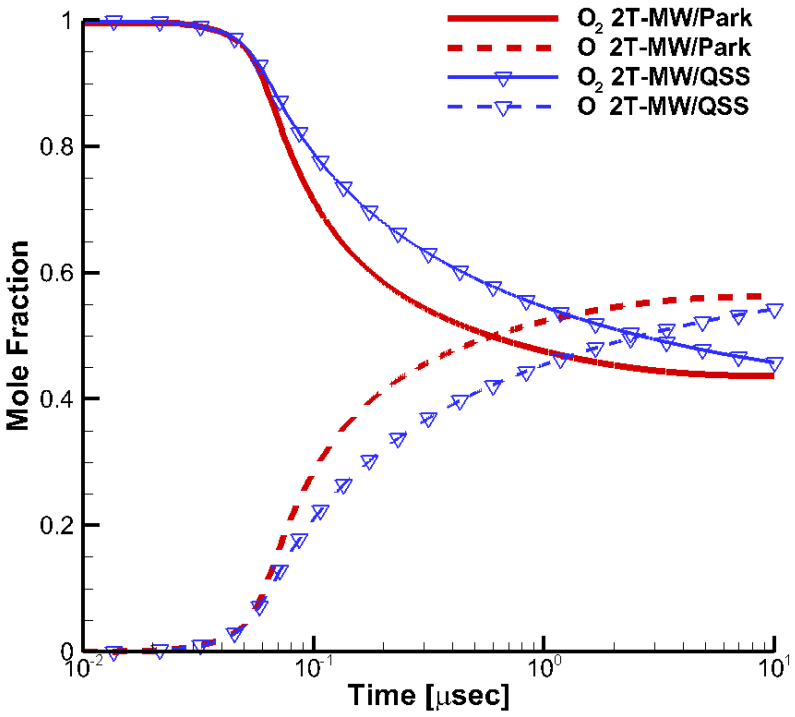

Figure 4.15: Composition profile, C3 case

4.2.2 State-to-State Model

The STS results section is separated into two portions. First, the sensitivity of the repulsive parameter α assumed by the FHO model is investigated to evaluate its influence on the O_2–O_2 STS rate coefficients and consequently on the overall solution. Next, the vibrational temperature and species profiles generated by the STS model are compared with those from the 2T models and the experiments. [35]

4.2.2.1 O_2–O_2 FHO parameter sensitivity

The STS rates utilize the FHO method that assumes the exponential repulsion in the O_2–O_2 system defined by parameter α. In the present work, the test cases using α values of 3.8, 4.0, and 4.2 Angstroms^{-1}. Previous work has shown that the exponential potential parameter is in the range of near 4.0 Angstroms^{-1} [23]. In this section, the O_2–O STS model adopts the QCT rates obtained from the Varandas potential.

Figure 4.16 presents the temperature profiles for the parametric study of α for case C1. As would be expected for the pure O_2 freestream, the α parameter has a strong influence on the solution since the early vibrational-translational behavior is primarily governed by O_2–O_2 collisions. A value of 3.8 has slower relaxation than the solutions obtained with the values of 4.0 Angstroms^{-1} and 4.2 Angstroms^{-1} for the entire relaxation process. After the vibrational temperature reaches a maximum, the results begin to coalesce. The later relaxation behavior is essentially identical between the various values of α. Even with the notable differences in behavior, all of the results fall within the spread of the experimental data.

Figure 4.17 presents the temperature profiles for C2. This case shows a similar influence of α on the temperature results. The faster relaxation due to higher temperatures and the faster introduction of O atoms from dissociation slightly reduce the variation due to α differences when compared to C1.

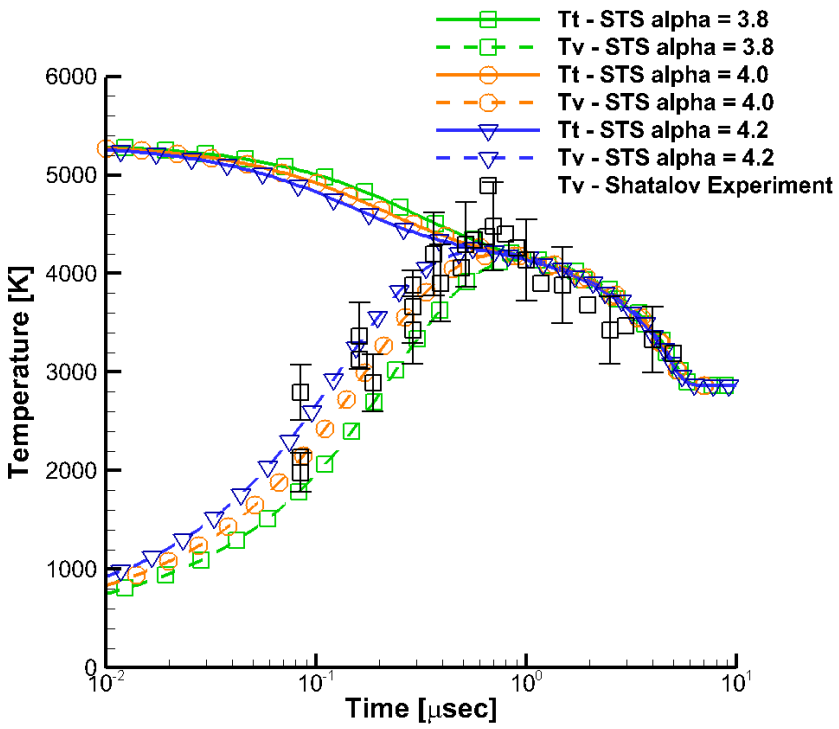

Figure 4.16: Temperature profiles evaluating the effect of α, C1 case

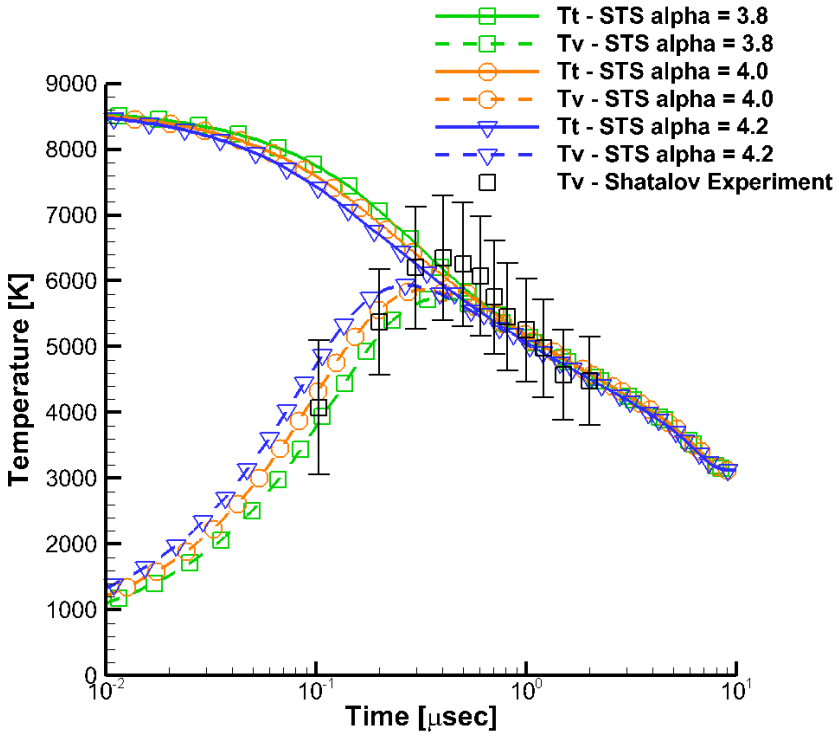

Figure 4.17: Temperature profiles evaluating the effect of α, C2 case

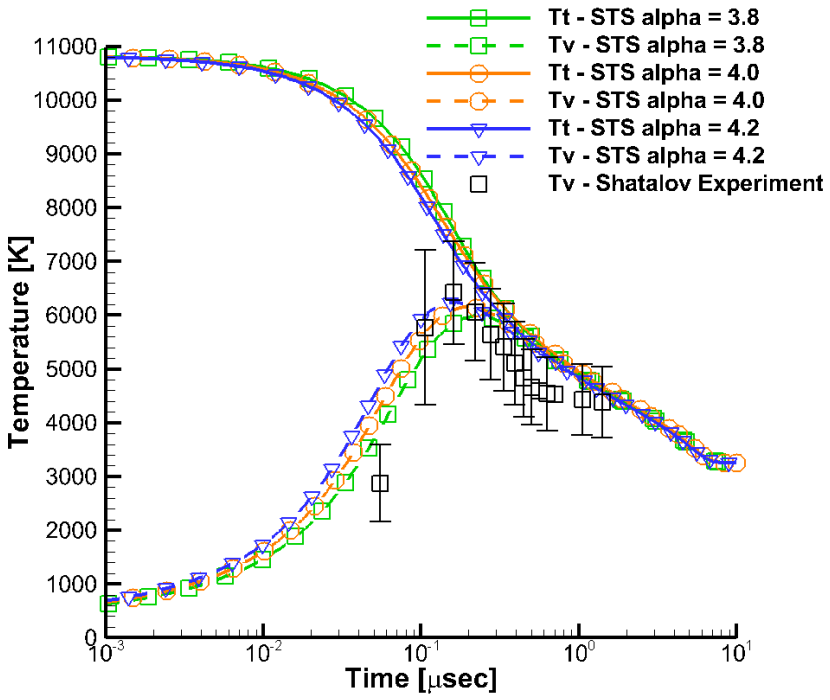

Figure 4.18: Temperature profiles evaluating the effect of α, C3 case

Figure 4.18 presents the C3 temperature profiles. At these elevated translational temperatures, the α influence is slightly mitigated by the quicker introduction of O atoms. All the results miss the first experimental point, but the α value of 3.8 Angstroms^{-1} is closest to capturing the first few experimental points. The application of the FHO rates for this case clearly shows the benefit of the STS model over the 2T model in terms of better agreement of T_v behavior for the early stage of relaxation.

In summary, the different values of α have a pronounced influence on the O_2–O_2 behavior. However, this effect is still smaller than the differences in T_v between the STS and 2T models.

4.2.3 Nonequilibrium Relaxation Influence on the Flow State Variables

The post normal shock test cases have exhibited significant nonequilibrium relaxation behavior. The focus is generally on thermochemical nonequilibrium, but it also

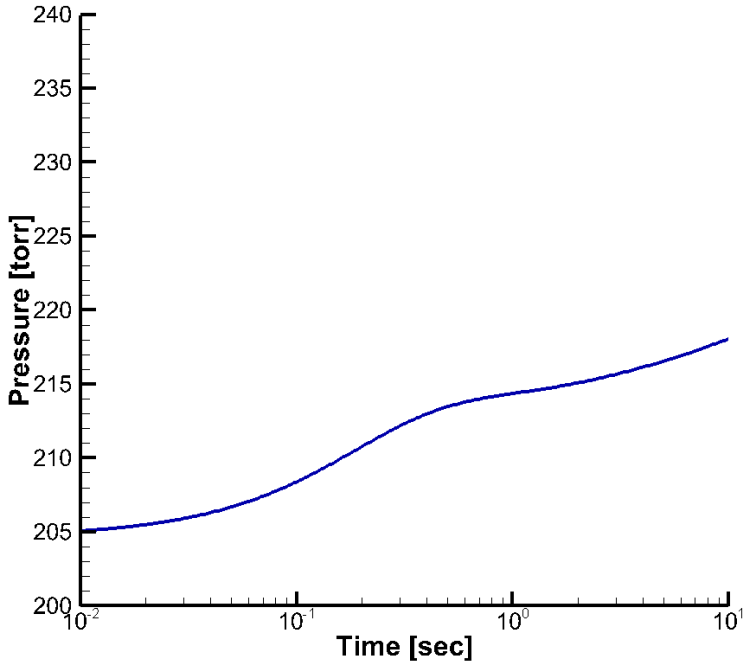

Figure 4.19: Pressure profile during post normal shock relaxation, C1 case

has a strong influence on the standard flow state variables. The pressure, velocity, and density profiles for the three test cases are shown in Figure 4.19 through . These profiles are generated by the STS-QCT Varandas model.

All three cases show the same general behavior for the standard flow variable profiles. The density and pressure rise, while the velocity decreases. This result is expected and somewhat intuitive. First, the reduction in translational temperature due to nonequilibrium relaxation corresponds to the rise in density, and consequently the rise in pressure since it is an isentropic process. The reduction in velocity is a byproduct of the conservation of mass in the flow from the raise in density. These profiles reinforce the importance of nonequilibrium model, not only for thermal protection systems, but also hypersonic flight dynamics. The nonequilibrium behavior can have a 10% influence on the pressure of the flow. This influence can have a large effect on aerodynamic performance and stability of the vehicle.

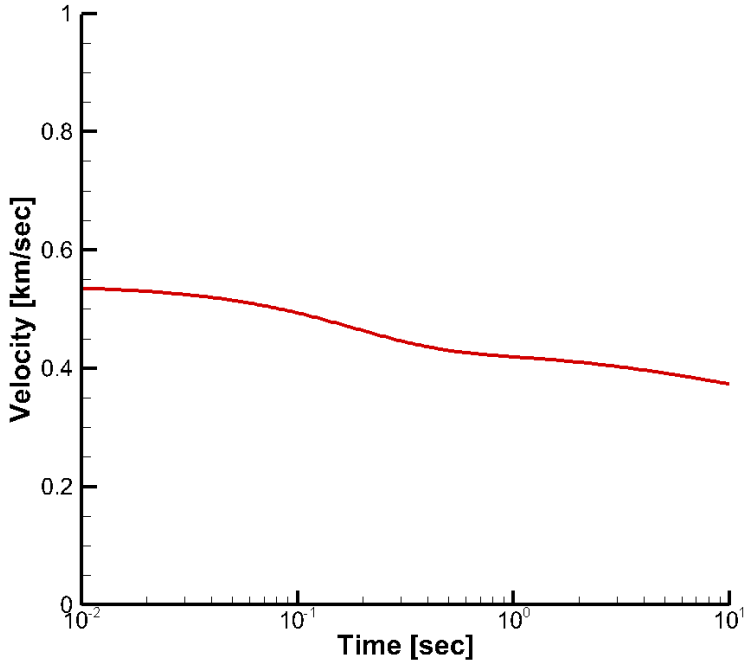

Figure 4.20: Velocity profile during post normal shock relaxation, C1 case

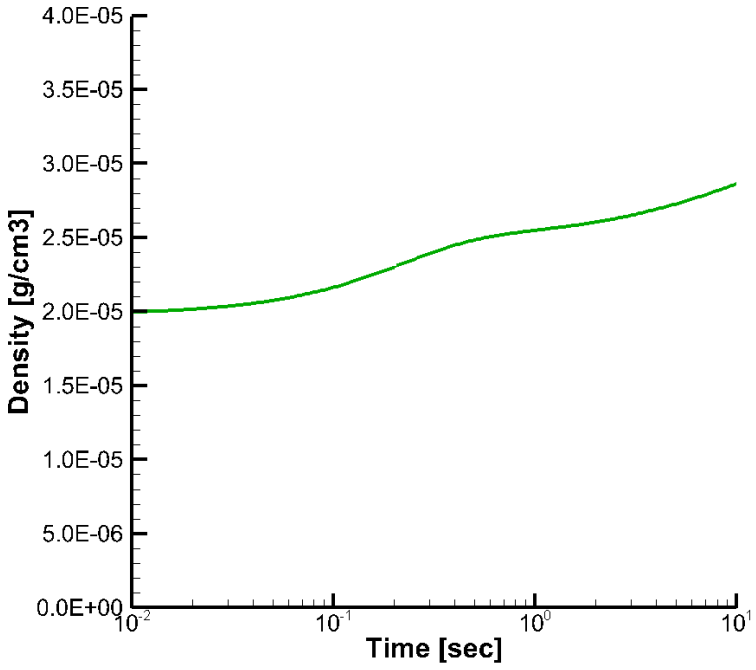

Figure 4.21: Density profile during post normal shock relaxation, C1 case

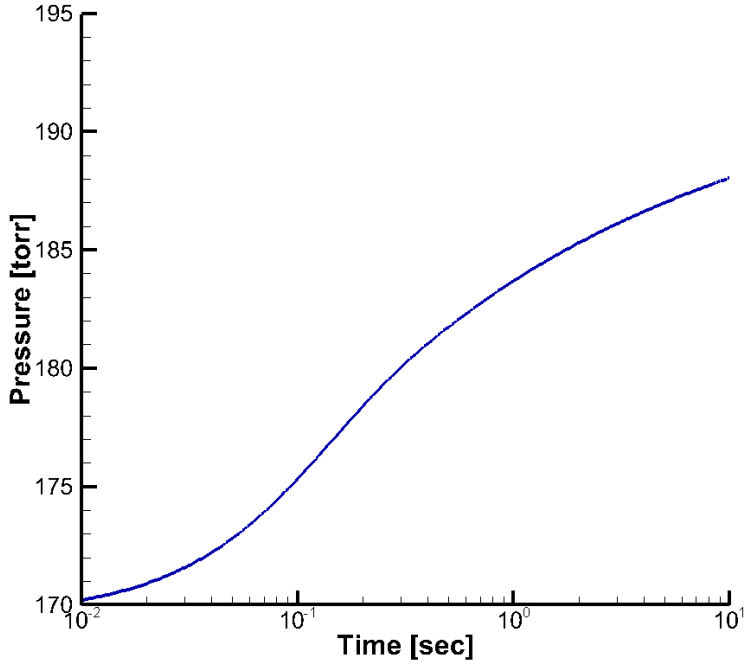

Figure 4.22: Pressure profile during post normal shock relaxation, C2 case

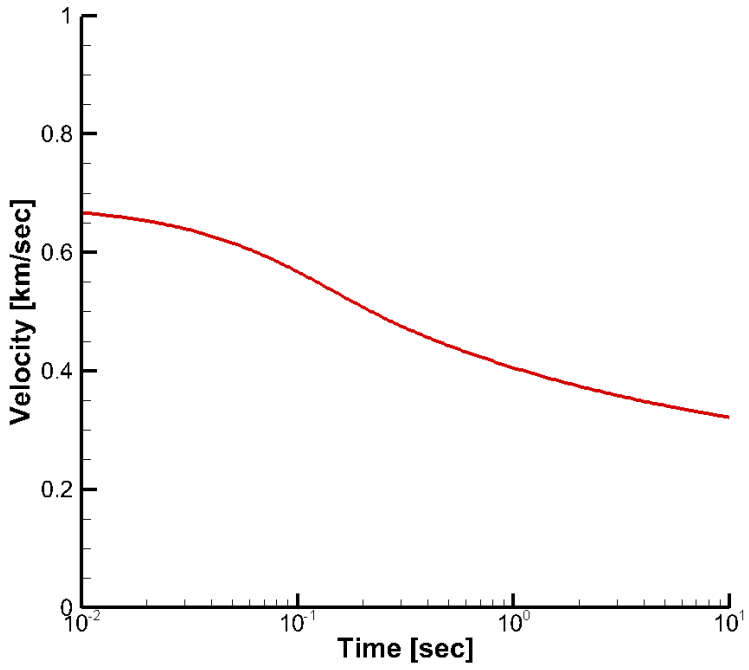

Figure 4.23: Velocity profile during post normal shock relaxation, C2 case

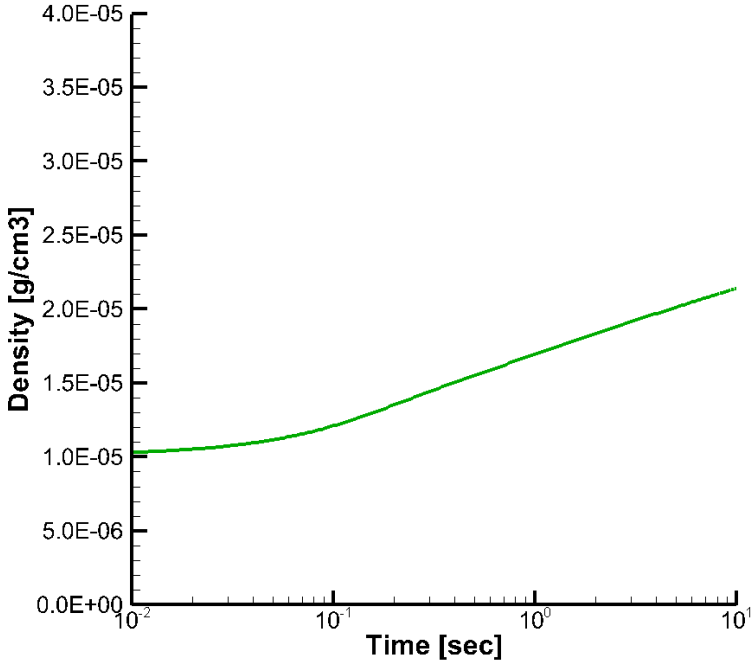

Figure 4.24: Density profile during post normal shock relaxation, C2 case

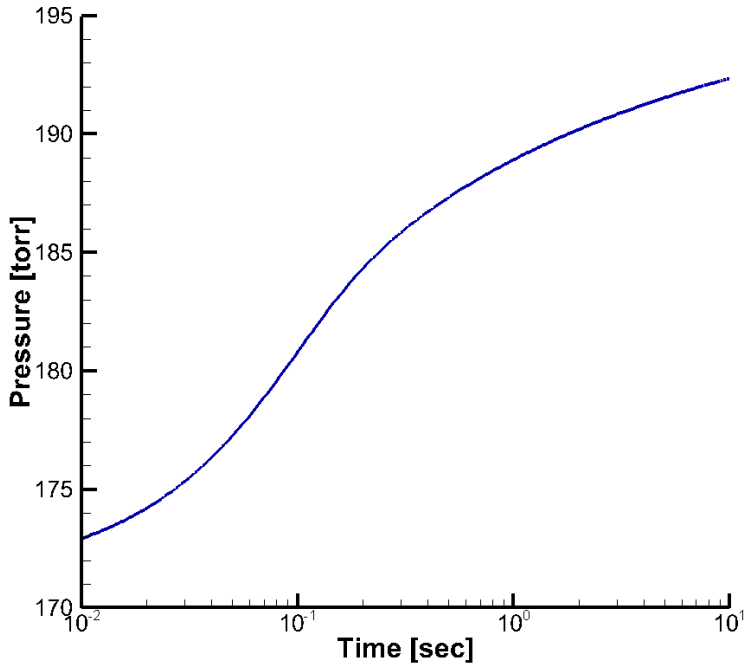

Figure 4.25: Pressure profile during post normal shock relaxation, C3 case

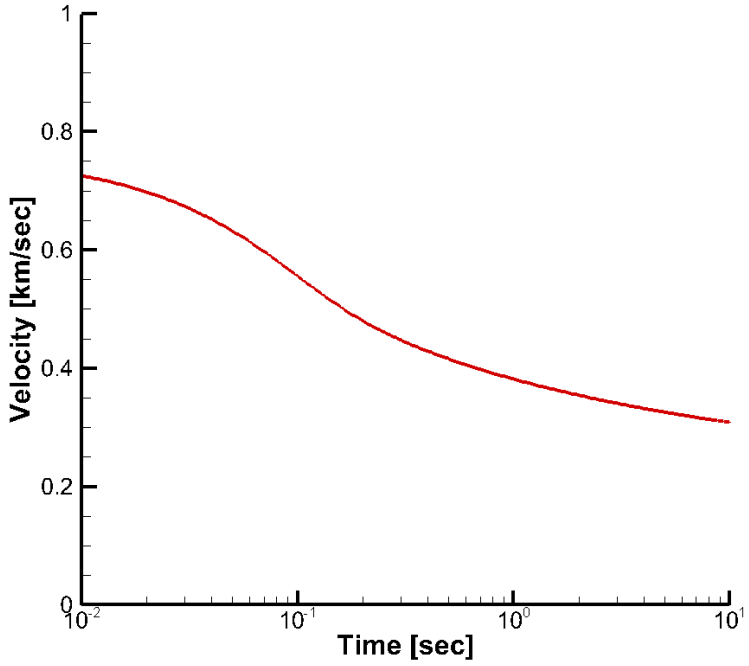

Figure 4.26: Velocity profile during post normal shock relaxation, C3 case

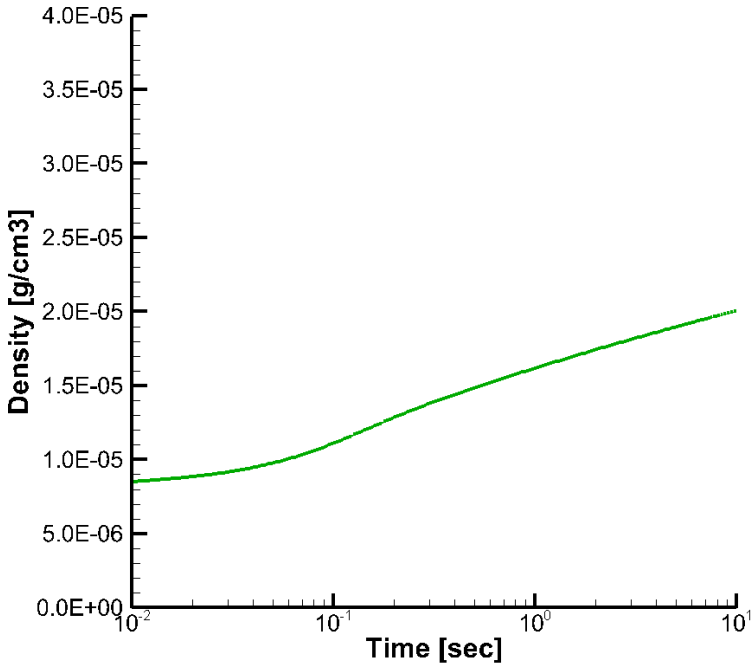

Figure 4.27: Density profile during post normal shock relaxation, C3 case

4.2.3.1 2T and STS models comparison

The results in this section focus on comparing the most current 2T models with the high fidelity, STS modeling approach and with the experimental data. The previous section showed that the QSS dissociation rate coefficients provides better agreement with the experimental data when incorporated in the 2T model. The improved 2T approach used for comparison in this section is the 2T–MW/QSS modeling approach. The STS–QCT Varandas method represents the highest level of fidelity investigated in this study.

Figure 4.28 presents the evolution of temperature for the three modeling approaches for case C1. There is a fundamentally different vibrational temperature profile between the STS and 2T approaches. The most notable differences are in the early vibrational relaxation phase, and also the time at which the maximum vibrational temperature is reached. The STS model relaxes more rapidly than the 2T models and reaches the maximum vibrational temperature first. The VT energy exchange by means of the STS model results in a noticeable difference in the profiles of translational temperature. Another important feature of the STS approach is a much faster convergence of temperature to the equilibrium value, compared to the 2T models. The STS model results do have a subtle overestimation during the dissociation phase. The overestimation can be attributed to the uncertainty in the O_2–O_2 dissociation rate coefficients, especially at a mild condition. Overall, the STS model matches the experimental data well. Figure 4.29 shows the difference in composition evolution for the three models. The rapid thermalization of vibrational and translational temperatures predicted by the STS model corresponds to the active generation of atomic oxygen in the flow, which is known to be much more effective for O_2 dissociation compared to diatomic oxygen [38].

Figures 4.30 and 4.31 present the evolution of the vibrational state population distribution for the STS model. The Boltzmann distributions plotted represent a

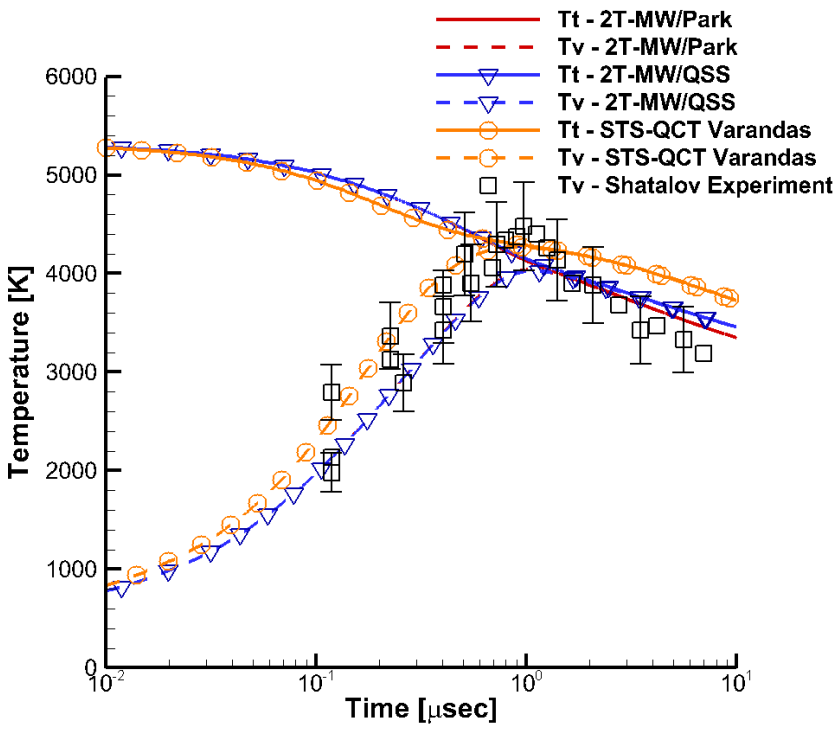

Figure 4.28: Temperature profiles, C1 case

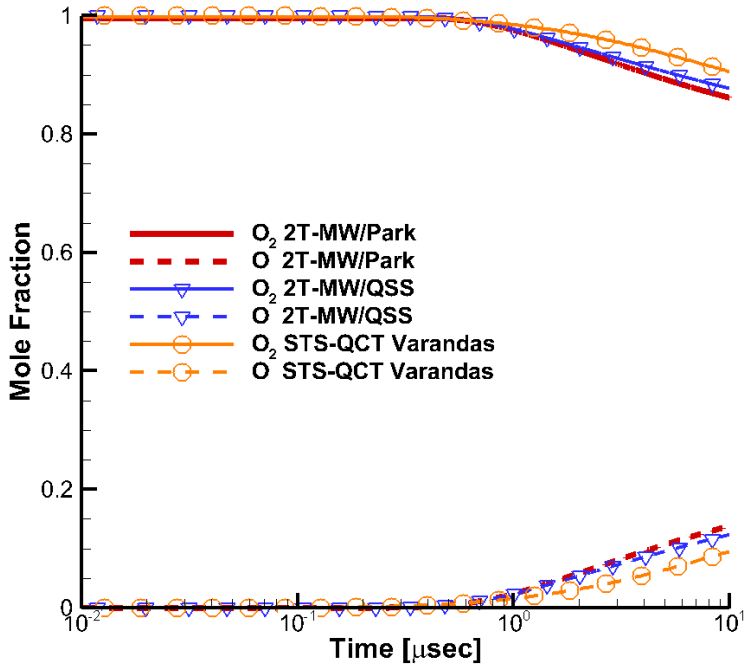

Figure 4.29: Composition profile, C1 case

temperature equivalent distribution for that given time. The first time location (t=0 μsec) represents the vibrational population distribution just before the shock passage. Initially, the flow is in equilibrium and the actual distribution does not deviate from the Boltzmann distribution. Once the shock passes, the distribution strongly deviates from the Boltzmann population prior to the onset of dissociation. The vibrational state population plots show that during the early vibrational relaxation phase, all the states higher than v = 3 are strongly overpopulated. In contrast, the v = 1 state shows a slight underpopulation relative to the Boltzmann distribution. The non-Boltzmann behavior shown in the population distribution during the relaxation process is mainly attributed to the ability of the STS model to account for multi-quantum transitions.

As the relaxation process continues, a change in slope of the population for v = 10, 20, and 40 can be observed in Figure 4.31 around 0.02 μsec. This slope change is an indication that the dissociation process has started and the presence of the oxygen atoms that lead to faster relaxation (O_2–O collisions). The dissociation is dominant in the higher vibrational states (v > 25) and, as the dissociation process increase, causes an underpopulation in these higher vibrational states. This large amount of dissociation from the higher vibrational states results in a smaller amount of energy being removed from the internal modes and a higher vibrational temperature compared to the 2T models. Additionally, the O_2–O collisions dominate the late phase of the chemical thermalization due to the efficient energy transfer of the collision. This attribute is realized in the rapid approach to equilibrium in the late phase (t > 0.2 μsec) when compared to the 2T model that implicitly assumes a Boltzmann distribution.

Figures 4.32 and 4.33 present the evolution of temperature and composition for case C2. The difference in the behavior between the STS and 2T models is more significant, compared to case C1. Unlike the 2T models, the STS approach is capable of describing the correct non-monotonic behavior of vibrational temperature and pre-

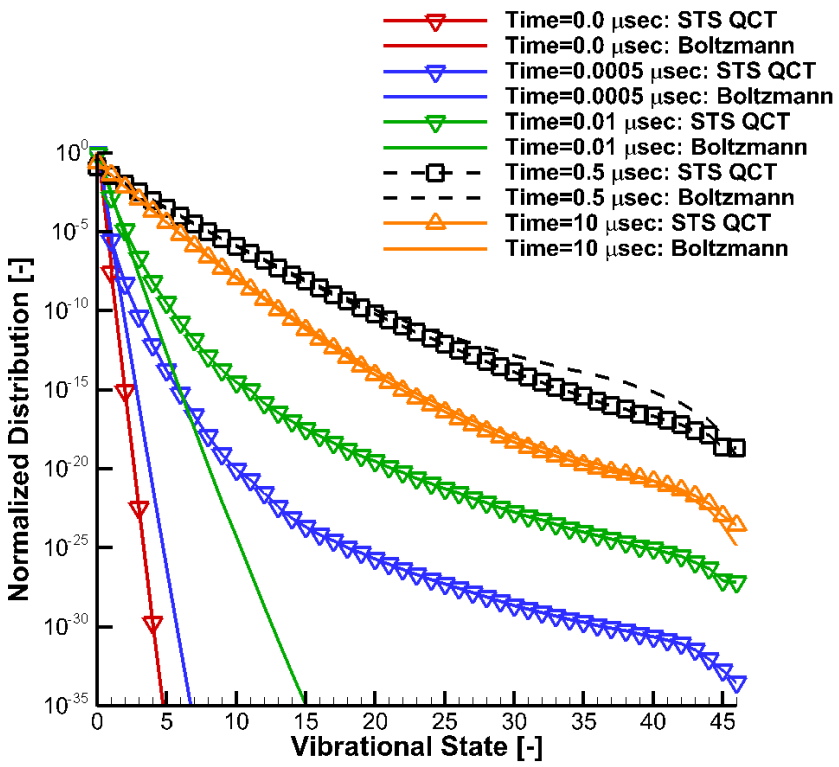

Figure 4.30: Vibrational population distribution evolution, C1 case

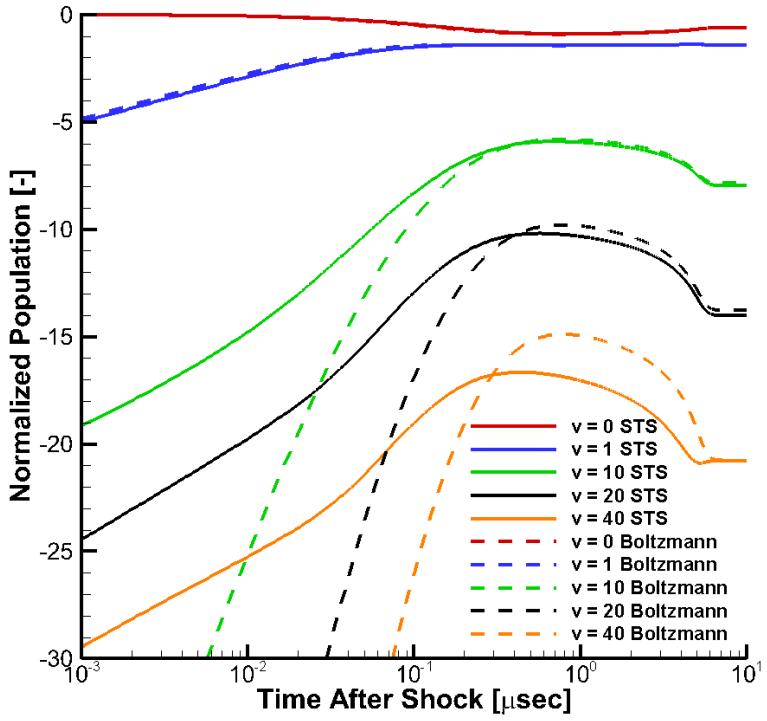

Figure 4.31: Vibrational state population evolution, C1 case

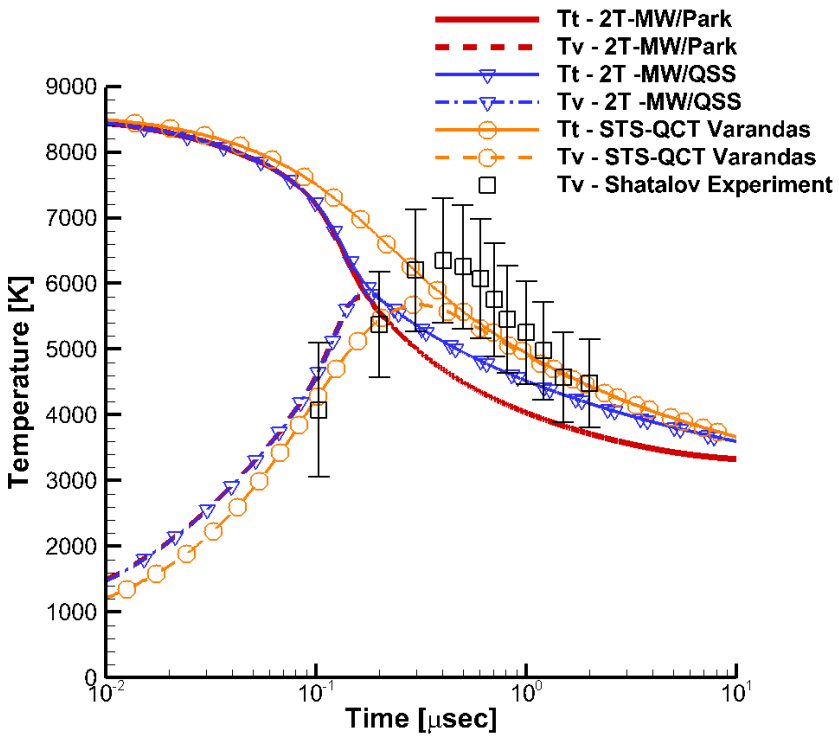

Figure 4.32: Temperature profiles, C2 case

dicts the location of T_v maximum. The STS solution is well within the experimental bars, and one can say that the higher fidelity model clearly shows an improvement over the simple 2T models.

Figures 4.34 and 4.35 present the vibrational population distribution for case C2. The general behavior of the vibrational ladder is quite similar to that for C1. However, two aspects are different. First, the excited states deviate strongly from the equilibrium value compared to the C1 case. Second, the lower vibrational states ($v > 23$) become depleted during active dissociation. This means that at stronger nonequilibrium conditions, the probability density function shifts toward the low-lying states.[7]

The profiles of vibrational temperature and species mole fraction for C3 are given in Figs. 4.36 and 4.37. It is important to note than the STS model allows accurate description of the phase of initial vibrational relaxation and clearly performs better

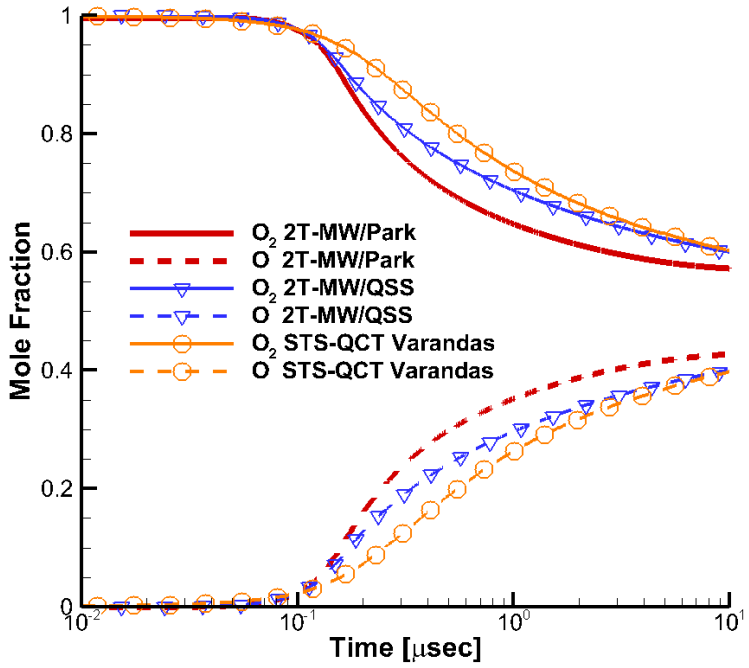

Figure 4.33: Composition profile, C2 case

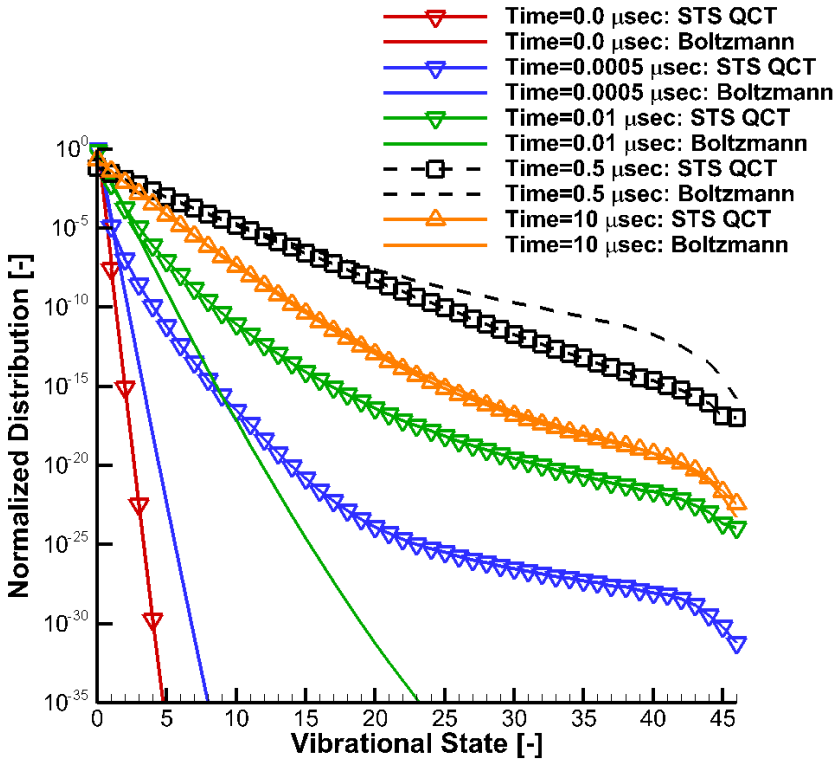

Figure 4.34: Vibrational population distribution evolution, C2 case

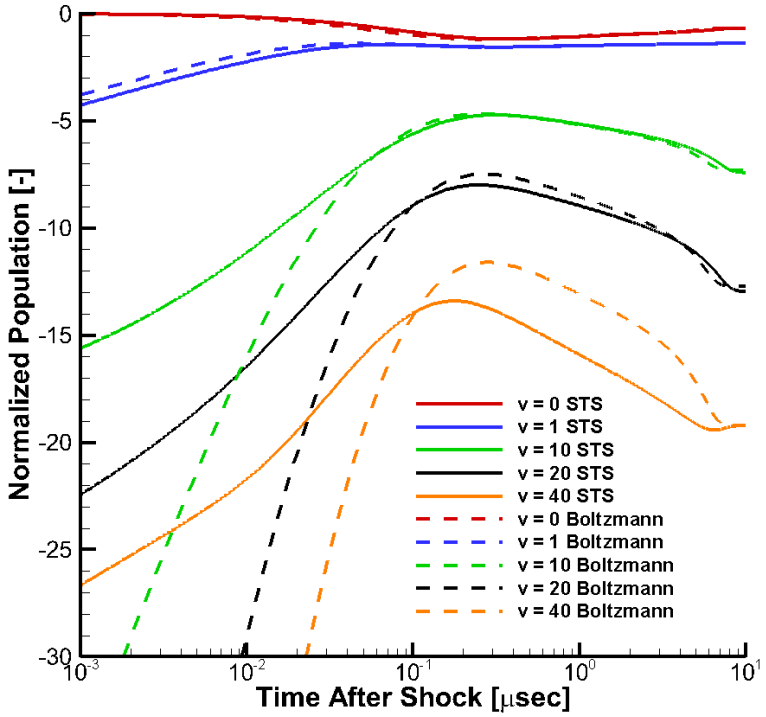

Figure 4.35: Vibrational state population evolution, C2 case

than the 2T model. The location of maximum vibrational temperature and the duration of the dissociation phase is captured by the STS approach too. In other words, the C2 and C3 cases show the superior accuracy of the STS model for describing thermal nonequilibrium flows of oxygen. The profiles of species for the case C3 is similar to that of case C2: the initial rate of atomic oxygen production is lower, however the large slope leads to a faster chemical equilibrium.

The state-resolved population of vibrational ladder for C3 is given in Figures 4.38 and 4.39. Under these conditions, vibrational states with $v > 20$ are noticeably affected by the dissociation process.

A note should be made in reference to the previously investigated 2T model using the QSS dissociation rates. The STS results show that the nonequilibrium behavior of these three cases do not reach a formal QSS condition. The vibrational state population evolutions show clearly that flow nears a QSS condition, but does not fully

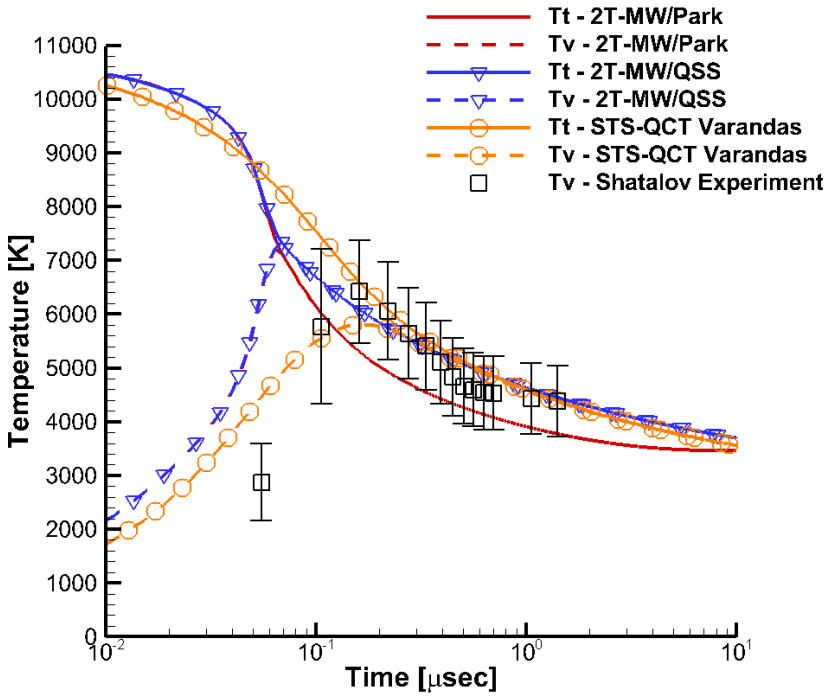

Figure 4.36: Temperature profiles, C3 case

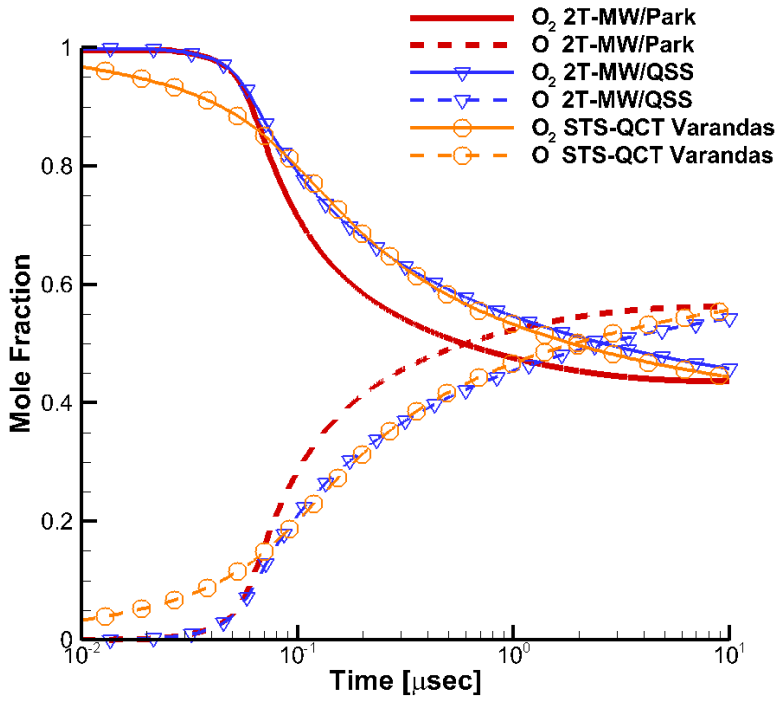

Figure 4.37: Composition profile, C3 case

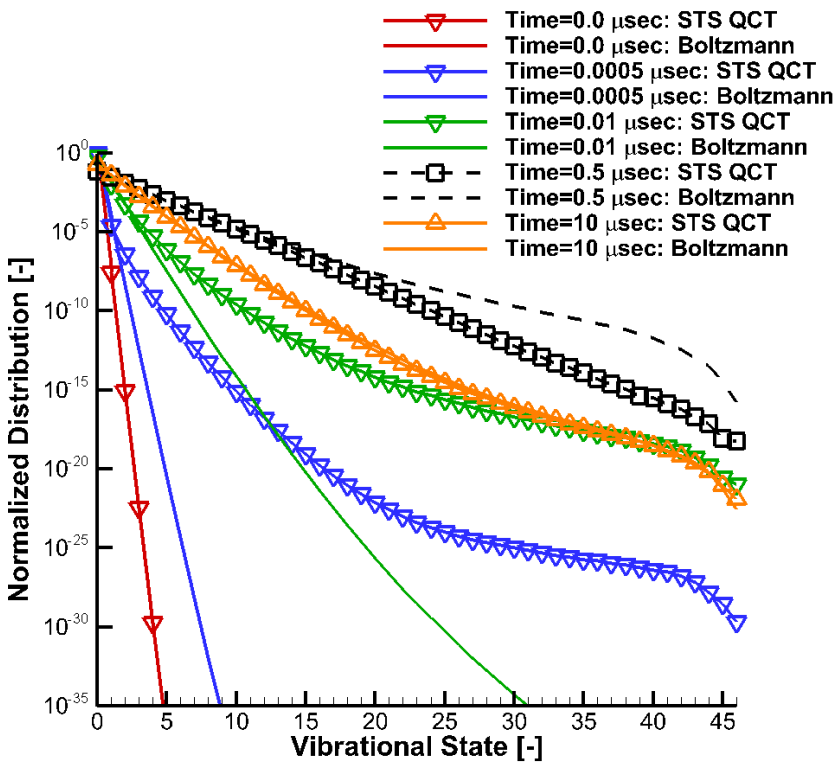

Figure 4.38: Vibrational population distribution evolution, C3 case

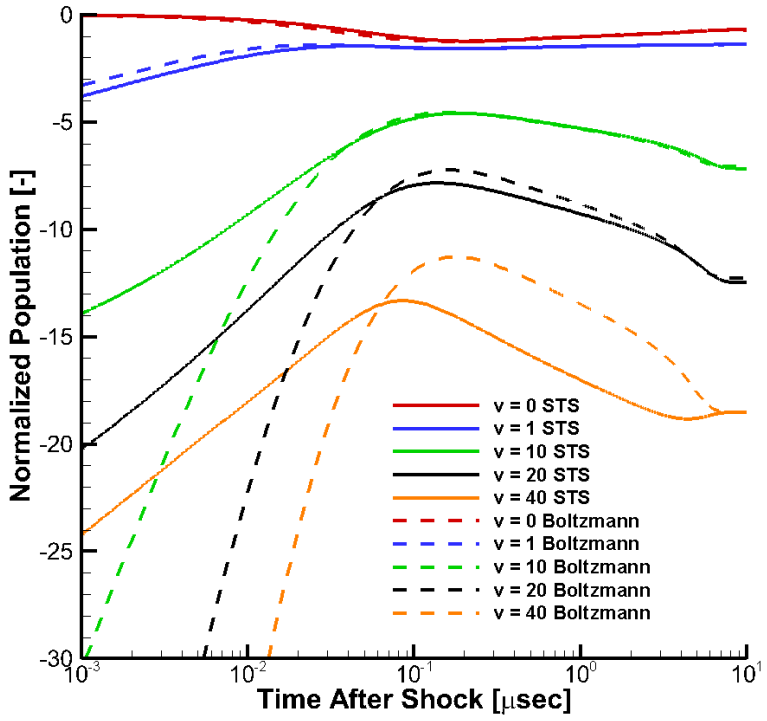

Figure 4.39: Vibrational state population evolution, C3 case

reach it. This observation corroborates the results shown in the 2T results section. The 2T model utilizing the QSS dissociation rates had the best agreement of all the 2T models, but had fundamental differences with the experimental measurements. The fact that the flow never reaches QSS supports the notion that the QSS assumption for dissociation rates is not always valid for practical hypersonic flight conditions.

4.2.4 Reduced Order Model

As previously described, a reduced order model (2T-NENB) is formulated in an attempt to extend the capability of the 2T modeling framework. An additional factor is introduced to allow previously omitted phenomena (non-Boltzmann effects) to be captured in the 2T modeling framework. The model parameters have been developed through an evaluation of the bound-bound and bound-free transition rates from detailed QCT analysis. This section will evaluate the performance of this reduced order model by comparing it to the experimental measurements, the widely used 2T model results, and the STS model results. Ideally, the reduced order model would be able to mimic the behavior of the STS model, thus providing a highly accurate modeling option with a reasonable computational cost.

Figures 4.40 and 4.41 present the evolution of temperature and composition for the two modeling approaches for Case C1. Case C1 is a mild nonequilibrium condition in comparison to C2 and C3. The results show that the STS model produces a fundamentally different result than the 2T models. The restriction of the 2T framework for the 2T-NENB model appears to be a hindrance for replicating the STS behavior. Interestingly, the mild C1 case has the worst performance for the 2T-NENB model. It can be noted that the 2T-NENB model results suggest that it has difficulty with the VT process early (when composition is correct) and has issues with composition later in the analysis.

Figures 4.42 and 4.43 present the evolution of temperature and composition for the

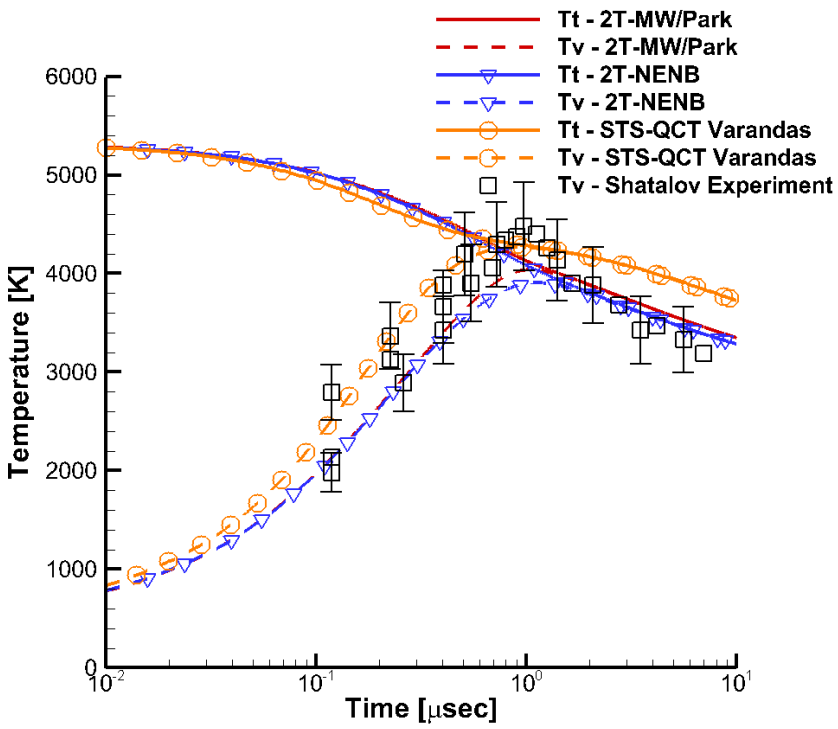

Figure 4.40: Temperature profiles, C1 case

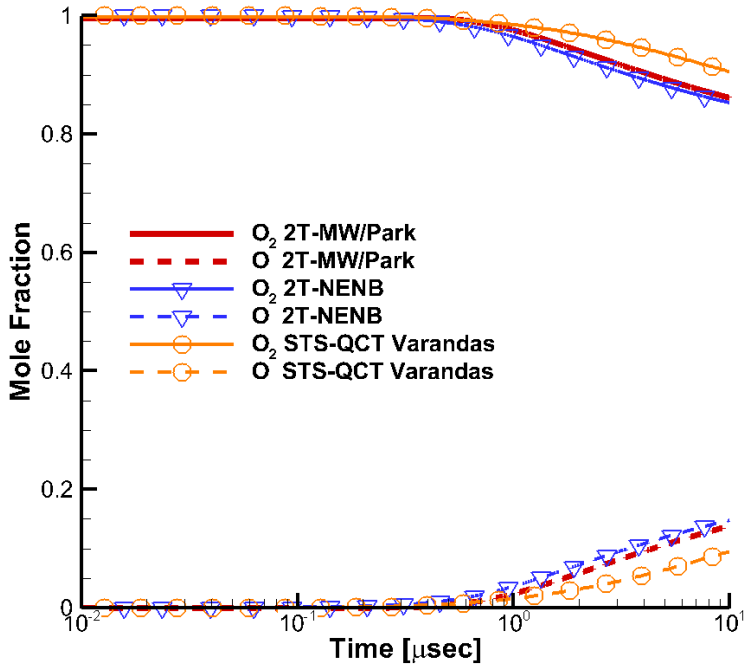

Figure 4.41: Composition profile, C1 case

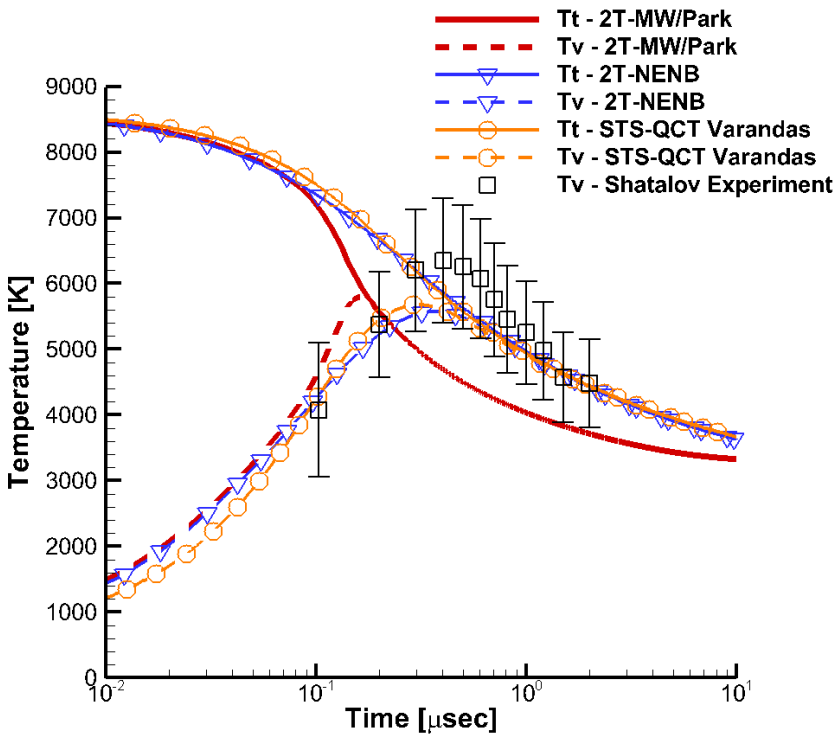

Figure 4.42: Temperature profiles, C2 case

two modeling approaches for Case C2. Once again there is a fundamental difference between the STS behavior and the 2T-MW/Park model. However, the 2T-NENB does well in replicating the STS behavior. Specifically, the composition profile comparison is almost identical. This is highlighting the importance of accounting properly for the nonequilibrium and non-Boltzmann effects that are prominent in the near QSS region. There could be improvement for the VT energy transfer around the peak T_v region.

Figures 4.44 and 4.45 present the evolution of temperature and composition for the three modeling approaches for Case C3. The difference in the behavior between the STS and 2T-MW/Park is significant once again. However, the 2T-NENB is able to capture most of the behavior observed in the STS analysis. It is not as precise as C2, but does retain the major features present in the STS results.

The shock tube flow comparisons show a distinct and fundamental difference be-

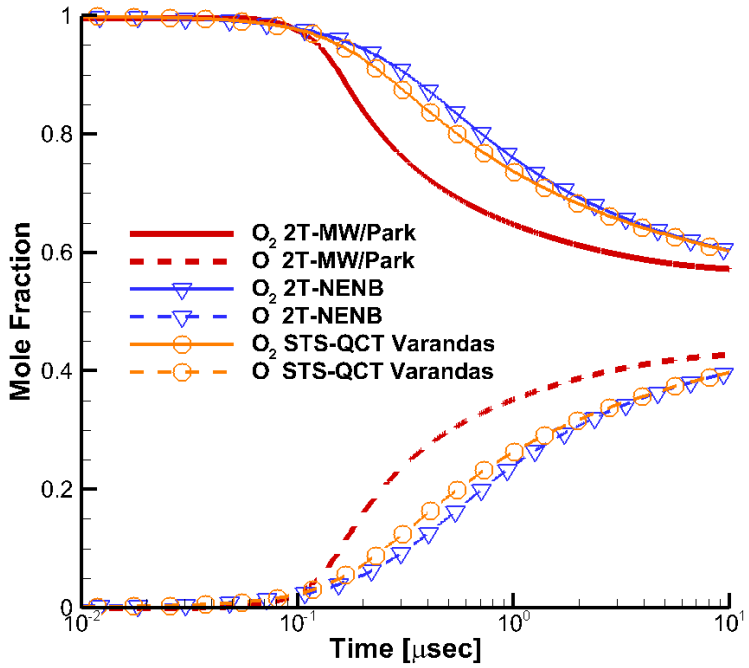

Figure 4.43: Composition profile, C2 case

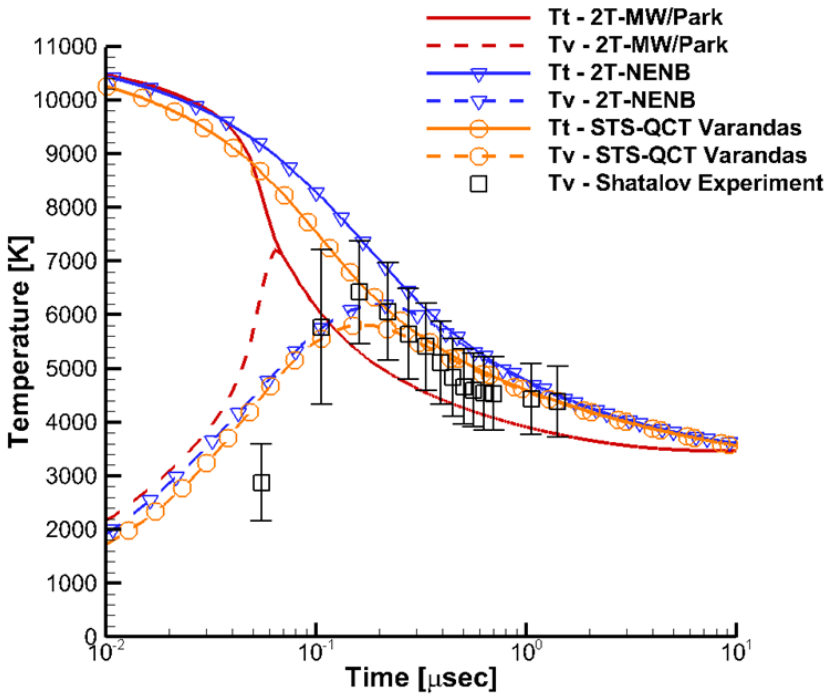

Figure 4.44: Temperature profiles, C3 case

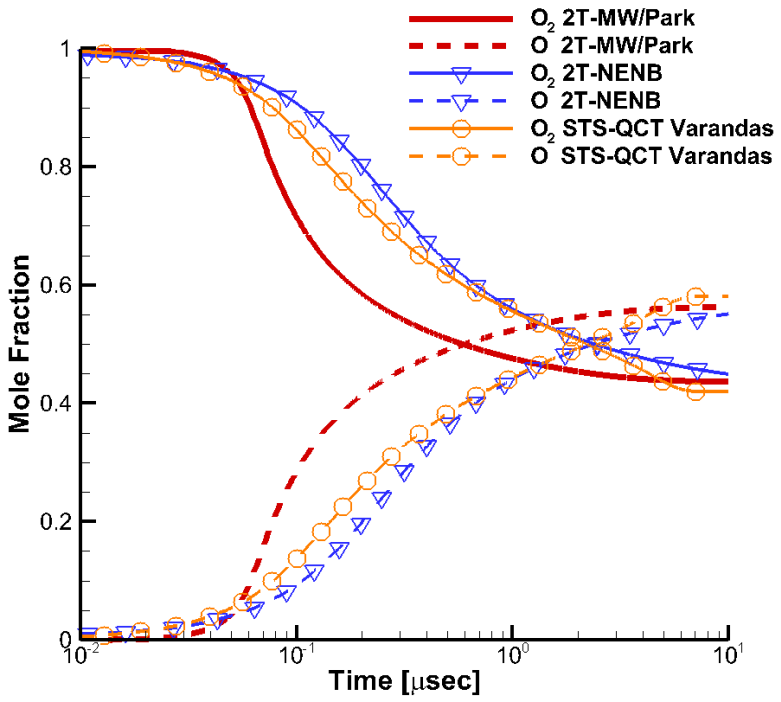

Figure 4.45: Composition profile, C3 case

tween the STS and 2T-MW/Park modeling results. The 2T-NENB model shows promise as a computationally inexpensive alternative to the high fidelity, STS model.

4.3 Summary

This chapter described the experimental data for a set of post normal shock measurements. The experiments correspond to hypersonic flight conditions ranging from mild nonequilibrium to strong nonequilibrium behavior. The measurements were used to evaluate various aspects of the numerical modeling.

The vibrational relaxation times and dissociation rates derived by different methods were compared. The widely used MW vibrational relaxation time and Park dissociation rates were compared with newly available, QCT based vibrational relaxation times and dissociation rates. The QCT-based vibrational relaxation times and dissociation rates provided a slightly better agreement with the experimental

measurements. Additionally, QSS dissociation rates provided the best 2T modeling agreement with the experimental data. However, all the 2T modeling results displayed a fundamentally different temperature profile than the experimental measurements. This was particularly evident in the stronger nonequilibrium cases.

In addition to the vibrational relaxation rates and dissociation rates, the vibrational energy loss due to dissociation is the final major piece of the 2T model. A study

In general, the STS modeling results agree better with the experimental measurements than the 2T modeling results. The STS modeling is able to capture non-Boltzmann behavior present in the relaxation and dissociation process. The non-Boltzmann behavior has a significant effect on the relaxation process for the stronger nonequilibrium cases. Specifically, the vibrational population distribution has an overpopulated tail relative to a Boltzmann distribution early in the relaxation process. Once the dissociation begins to become significant, the population tail becomes depleted and is underpopulated relative to a Boltzmann distribution.

Finally, the reduced order model developed in this thesis (2T-NENB) compared favorably with the experimental measurements and STS results. The reduced order model is limited by the 2T framework that it was constrained to during development. Some behavior in the experiments was only able to be captured by the STS analysis. However, the reduced order model was able to mimic most of the behavior observed in the STS results, and thus shows promise as a computationally inexpensive modeling option to obtain accurate nonequilibrium behavior.

CHAPTER V

Double-Cone Investigation

This chapter of the dissertation presents an overview of the CFD code used to perform multi-dimensional, nonequilibrium flow simulations. First, a description of the standard version of LeMANS is presented. LeMANS has two-temperature modeling capability for nonequilibrium. Next, LeMANS has been modified through the work in this dissertation to perform state-to-state, nonequilibrium simulations.

5.1 LeMANS CFD Flow Solver

CFD numerical simulations are performed using the finite volume code LeMANS that has been developed at the University of Michigan for simulating hypersonic reacting flows. LeMANS is a multi-dimensional, parallel code that solves the Navier-Stokes equations on unstructured grids with second-order spatial accuracy. The flow is modeled assuming that the continuum assumption is valid and that the fluid is Newtonian. Thermo-chemical nonequilibrium effects are model using the multi-temperature model for thermal nonequilibrium and reaction rates in the mass conservation account for chemical reactions. In this approach, there is a translational temperature, T_t, and a different vibrational temperature, T_v. The other energy modes are assumed to be in equilibrium with either the translational or vibrational temperature. For example, the rotational mode is assumed to be in equilibrium with the translational mode

(i.e. $T_r = T_t$). The rotational temperature can be accounted for separately in the LeMANS framework, however, the presented work will limit the nonequilibrium modeling to only two temperatures. Turbulence is modeled using the 0-equation algebraic Baldwin-Lomax turbulence model. This turbulence model is appropriate for well behaved, attached flows. The presented work is assumed to be laminar. The full details of LeMANS can be found in Ref.[39]. The governing equations solved by LeMANS for flows with thermal nonequilibrium and finite-rate chemistry are written below,

$$\frac{\partial \rho_s}{\partial t} + \nabla \cdot (\rho_s \mathbf{u} + \mathbf{J_s}) = \dot{\omega}_s \tag{5.1}$$

$$\frac{\partial \rho \mathbf{u}}{\partial t} + \nabla \cdot \left(\rho \mathbf{u}\mathbf{u} + P\bar{\bar{I}} - \bar{\bar{\tau}} \right) = 0 \tag{5.2}$$

$$\frac{\partial E}{\partial t} + \nabla \cdot \left((E+P)\,\mathbf{u} - \bar{\bar{\tau}} \cdot \mathbf{u} + (\mathbf{q_t} + \mathbf{q_r} + \mathbf{q_{ve}}) + \sum_s (\mathbf{J_s} h_s) \right) = 0 \tag{5.3}$$

$$\frac{\partial E_{ve}}{\partial t} + \nabla \cdot \left(E_{ve}\mathbf{u} + \mathbf{q_{ve}} + \sum_s (\mathbf{J_s} e_{ve,s}) \right) = \dot{\omega}_{ve} \tag{5.4}$$

where ρ_s is the density of species s, $\mathbf{u}$ is the bulk velocity, P is the pressure, $\bar{\bar{I}}$ is the identity matrix, h_s is the species enthalpy, and $\mathbf{J_s}$ is the diffusion flux for species s modeled using a modified for of Fick's law. E and E_{ve} are the total and vibrational-electron-electronic energies per unit volume of mixture, while $e_{ve,s}$ is the vibrational-electron-electronic energy per unit mass. $\dot{\omega}_s$ is the mass source term that corresponds to dissociation and recombination. $\dot{\omega}_{ve}$ is the vibrational energy source term that corresponds to vibrational relaxation and dissociation.

5.2 State-to-State CFD Modeling

LeMANS has been modified to also include STS modeling of the vibrational energy mode. A master equation system is solved along with the flow equations. The equations below highlight the additional relations required to perform the vibrational

energy STS simulation,

$$\frac{\partial \rho_v}{\partial t} + \nabla \cdot (\rho_v \mathbf{u}) = \dot{\omega}_v \quad v = 0, 1, 2... \tag{5.5}$$

$$\dot{\omega}_v = \frac{1}{M} \sum_{v'} \left[k_{VT} \left(v' \rightarrow v \right) \rho_{v'} \rho - k_{VT} \left(v \rightarrow v' \right) \rho_v \rho \right] \tag{5.6}$$

$$\rho = \sum_{v=0}^{v'} \rho_v \tag{5.7}$$

$$e_{vib} = \sum_{v=0}^{v'} \frac{\rho_v}{\rho} \epsilon_v \tag{5.8}$$

where ρ_v is the density of the vibrational level v, $\mathbf{u}$ is the bulk velocity, k_{VT} is the STS rate coefficient, and ρ is the bulk density.

The inclusion of the STS modeling increases the computational time of the analysis substantially. Inherently, there are more equations to solve (47 vibrational states). Also, the system of STS equations is very stiff and requires a conservative choice in time step. The computational cost of the STS modeling calculation is 40 times the cost of the nominal 2T calculation. Others in hypersonic research have worked to improve the computational efficiency of the STS CFD method through various solver methods[40, 41] including operator splitting (e.g. Strang splitting). More work in this area is needed to reduce the computational expense of this type of simulation. The presented work utilizes a 2T model converged solution as the initial condition for the STS analysis (assumed Boltzmann distributions). This significantly reduces the computational time, but the solution time is still around 15 times that of the nominal 2T calculation.

5.3 Experimental Setup

The double cone experimental data was obtained from the CUBRC LENS-XX expansion tunnel[42]. The focus of the work presented in this paper is on Run 87.

Test Case	Total Enthalpy $[\frac{MJ}{kg}]$	Mach Number	Velocity $[\ \frac{m}{s}\ ]$	P [Pa]	T_t	T_v	C_{O_2}	C_O
Run 87	9.9	8.1	4,019	165	626	712	0.9245	0.0755

Table 5.1: Summary of flow conditions for Run 87[42]

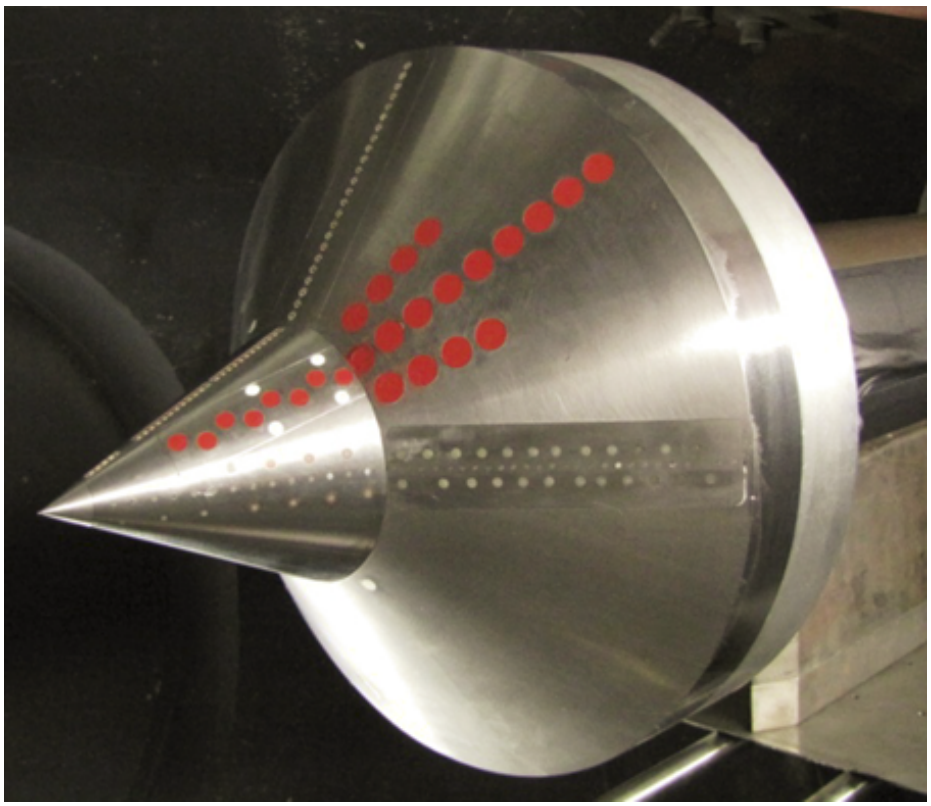

Figure 5.1: Double-cone data points

The freestream flow conditions for Run 87 are shown in Table 5.1 .

Run 87 is a double-cone configuration. Pressure and heat transfer data was acquired at many points along the model surface. No flow field measurements were taken so only the experimental surface data will be used for model comparison. A picture and diagram[42] of the double-cone configuration are shown in Figures 5.1 and 5.2, respectively.

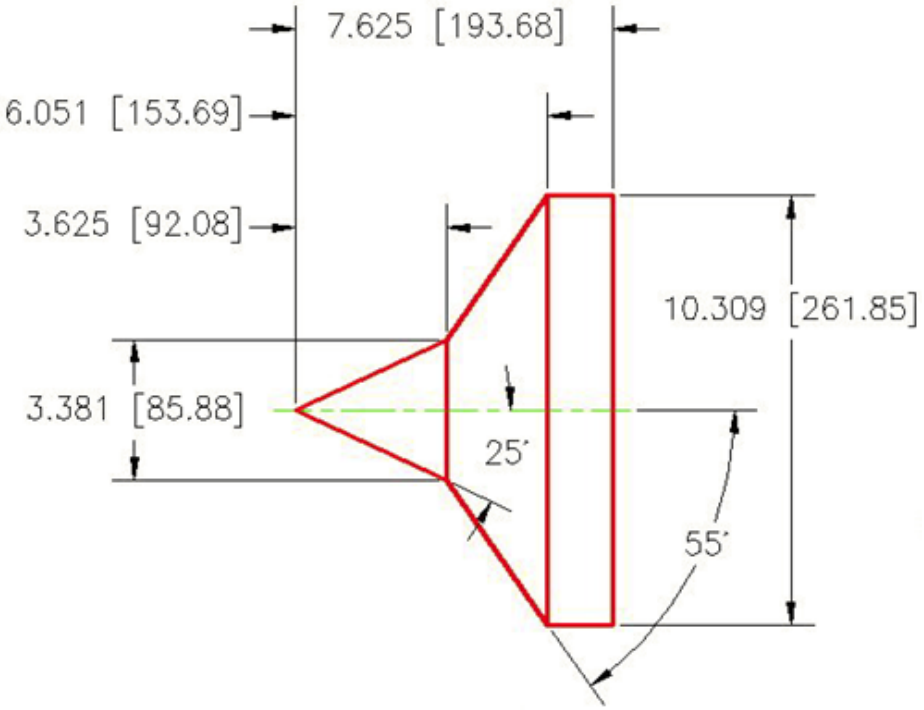

Figure 5.2: Double-cone dimensions

5.4 Results and Comparison

The CFD results shown are from an axisymmetric grid consisting of 250,000 cells. A grid resolution study was performed to ensure grid independence. Specifically, a coarse grid containing 125,000 cells and a refined grid containing 500,000 cells were used to ensure that the solution was not grid dependent. The grid used for the results presented is shown in Figure 5.3.

The experiments were designed to have laminar flow so the CFD model assumes that the flow is laminar. Figure 5.4 presents the pressure contours for the nominal flow field of Run 87 using the standard 2T model. The flow field contains complex flow features near the double-cone transition. There is shock and boundary layer interaction along with flow separation.

Figure 5.5 shows the translational temperature contours for the 2T-MW/Park model. Figure 5.6 shows the vibrational temperature contours. The translational

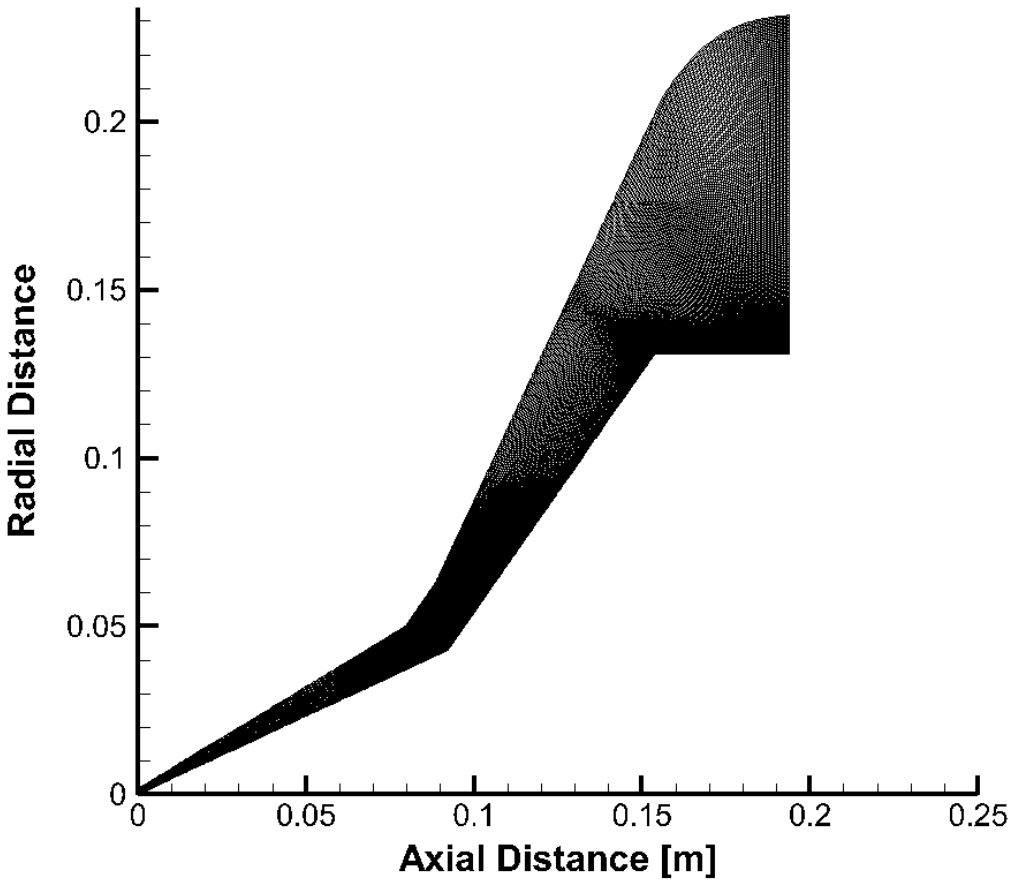

Figure 5.3: CFD Grid: 250,000 cells

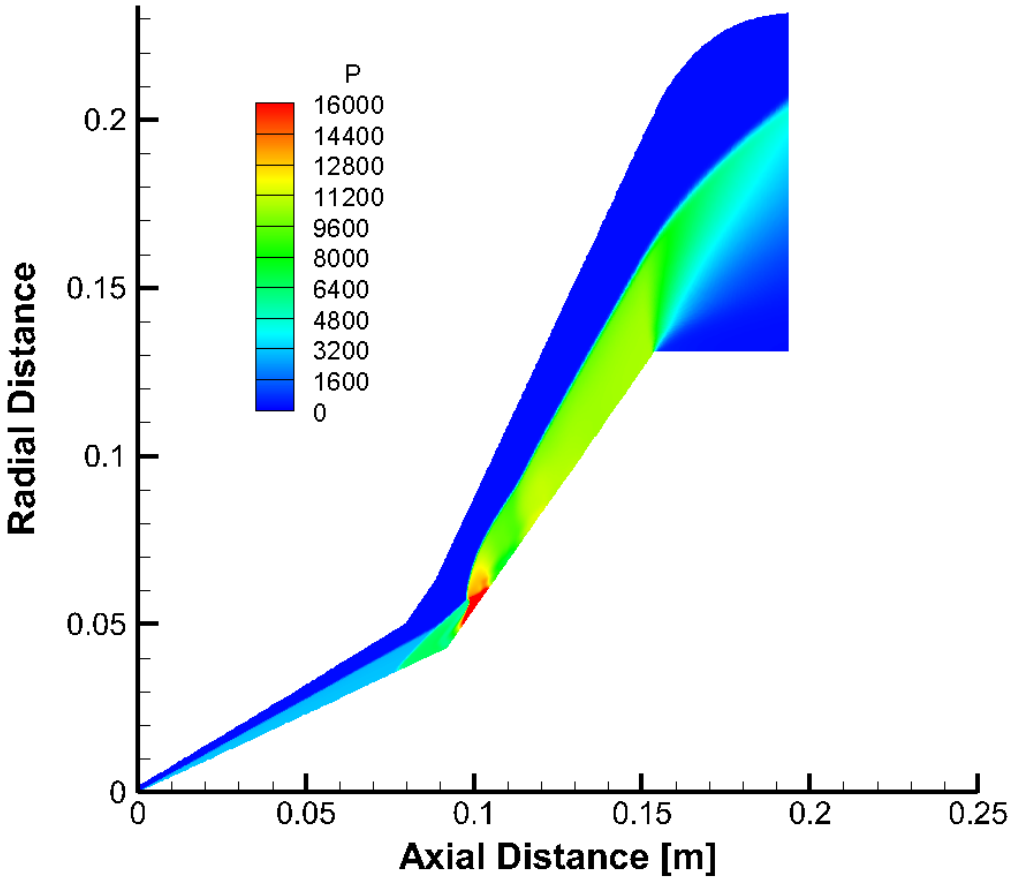

Figure 5.4: Pressure contour plot for nominal conditions

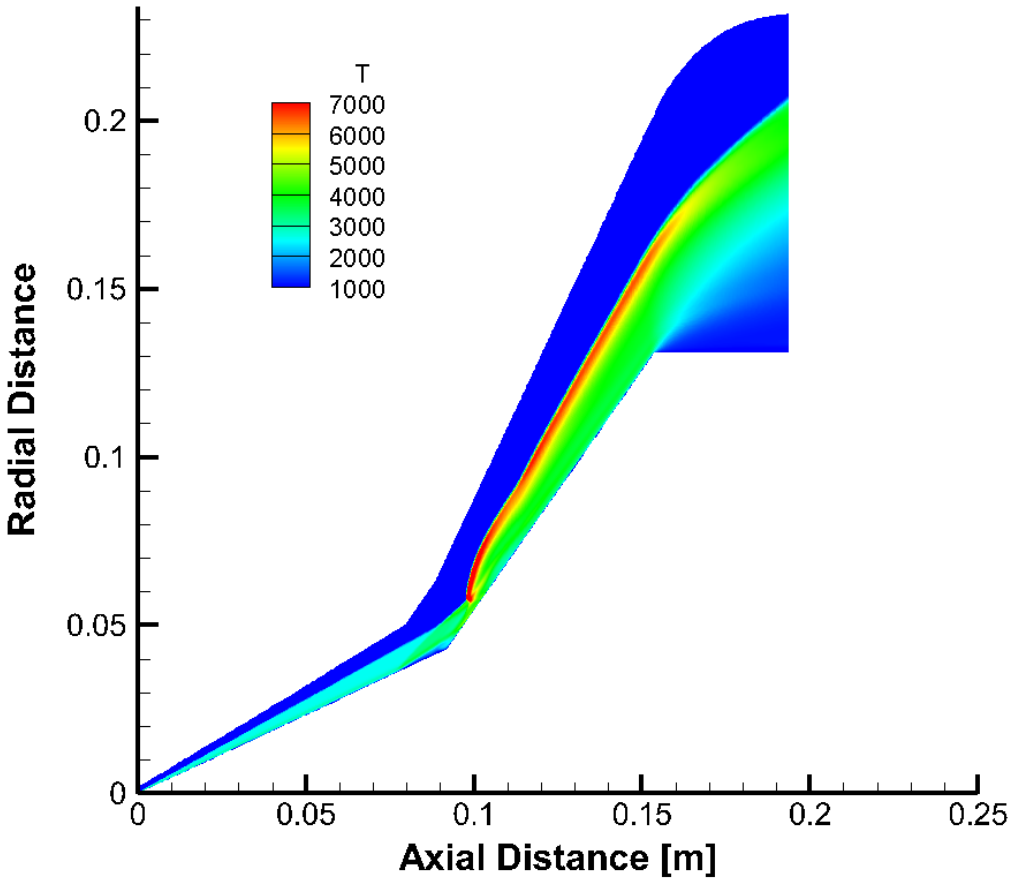

Figure 5.5: Translational temperature contour plot for nominal conditions

and vibrational temperature plots demonstrate the nonequilibrium behavior that is present in the flow field, particularly, in the second (upper) oblique shock region. The translational temperature rises quickly across the shock wave and then vibrational-translational energy transfer acts to bring the two energy modes into equilibrium downstream of the shock.

The contour plots are not able to show the differences between the different models and no experimental data was collected in the flow field. The model comparisons will be made on the double cone surface quantities. Figures 5.7 and 5.7 present

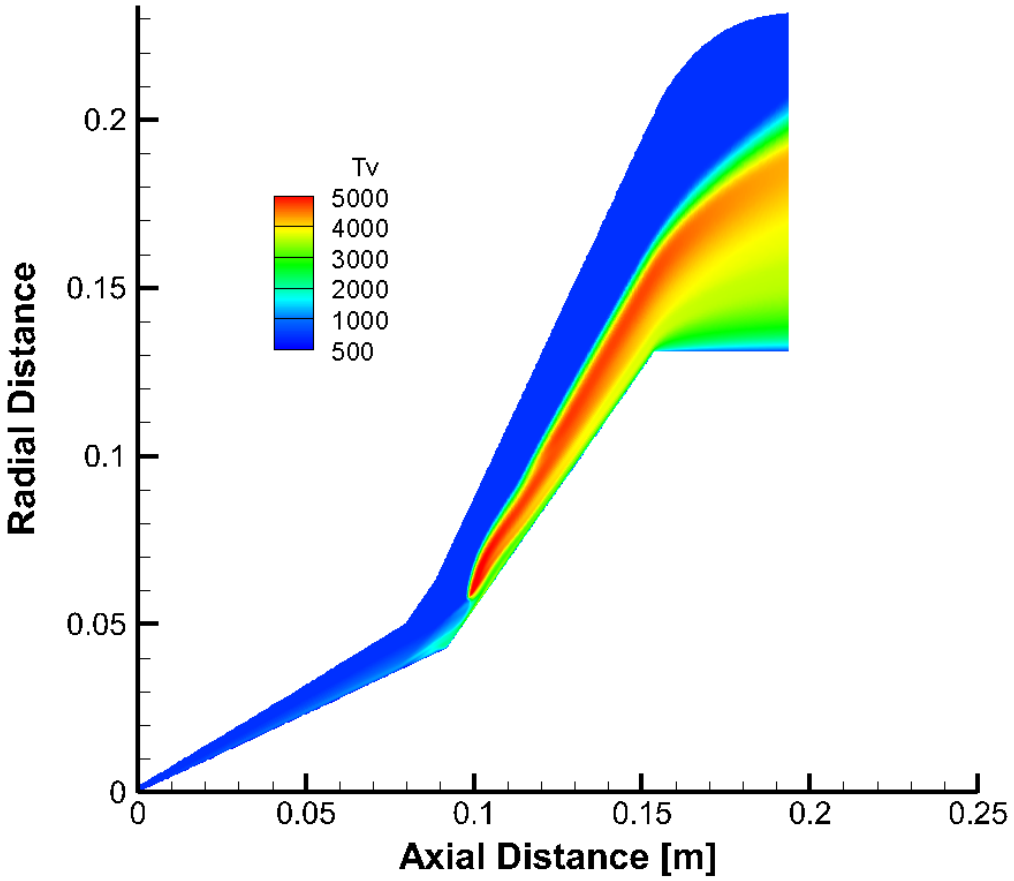

Figure 5.6: Vibrational Temperature contour plot for nominal conditions

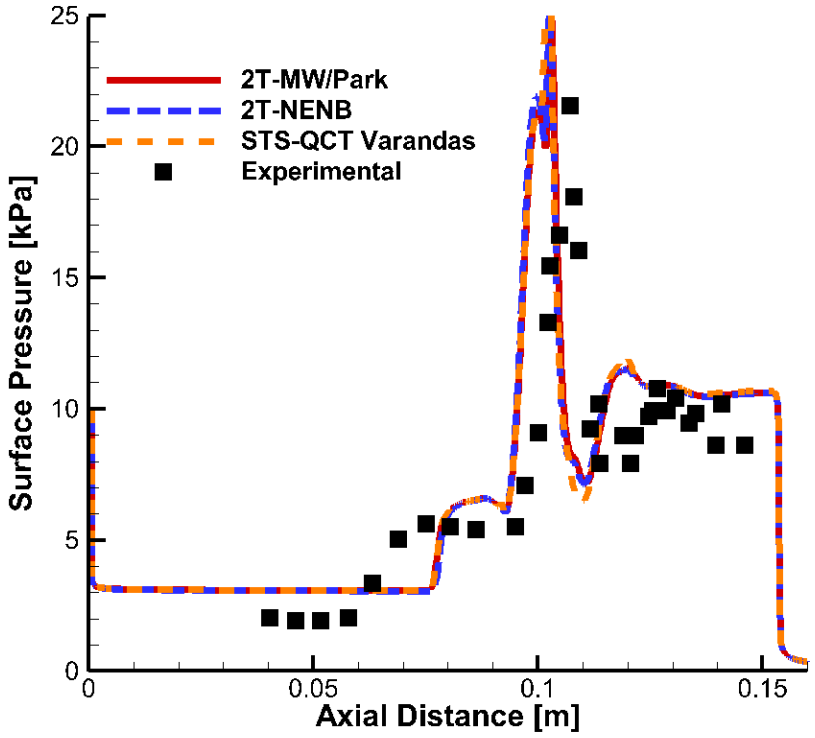

Figure 5.7: Pressure distribution on double cone body

the pressure and heat transfer distributions for the three modeling types and the experimental data. The differences in the models are almost indistinguishable for surface quantities. All of the models possess the same features as the experimental data, however they do not capture all the features accurately. For example, the experimental data shows a sharp drop in heat transfer around an axial distance of 0.065. The models have this feature but it does not occur until an axial distance of 0.80. Given the similarity in the results presented, further work is needed to understand the differences between the CFD results and experimental data. Near wall modeling and freestream conditions are potential areas for future investigations.

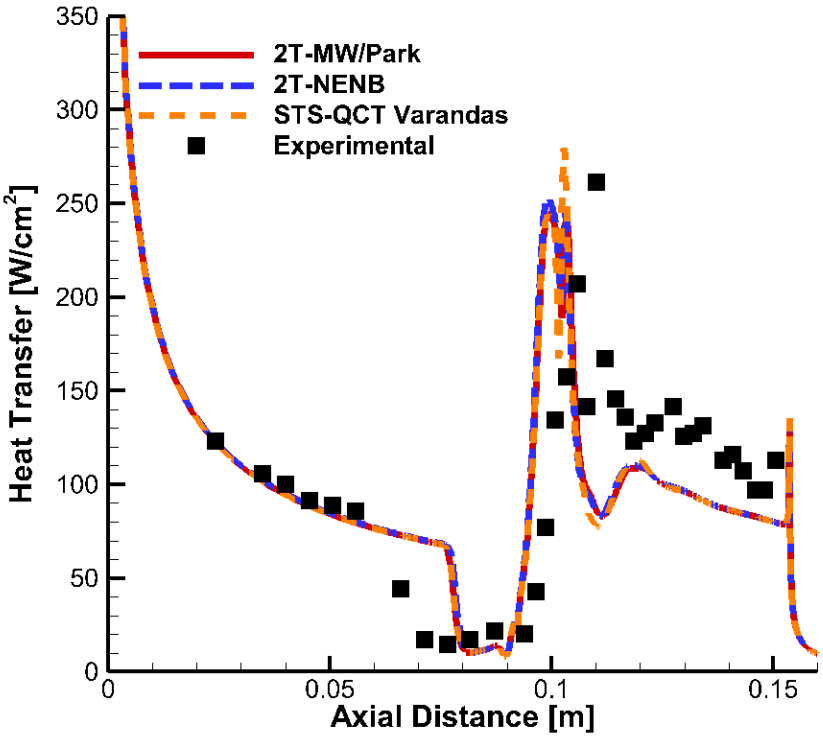

Figure 5.8: Heat transfer distribution on double cone body

5.5 Summary

In the present chapter, the CFD tool, LeMANS, have been described and the addition of STS modeling capability are presented. Additionally, the numerical results from the CFD analysis are compared with double-cone experimental data. The simulation demonstrates the substantial increase in computational cost for STS simulation. Also, the results show that the inclusion of STS modeling does not capture the behavior observed in the experimental data. Further investigation of these 2D flows will be needed to understand any additional modeling effects that could be at play.

CHAPTER VI

Summary and Conclusions

6.1 Summary

Vibrational thermochemical nonequilibrium modeling is a critical aspect of hypersonic vehicle design. Namely, computationally efficient, reduced order models that accurately capture the relevant physics are required due to the current computational hardware capability and high computational cost of the high fidelity, state-to-state (STS) modeling. The two-temperature (2T) model is the state of the art thermochemical nonequilibrium model for hypersonic design work. The 2T model is powerful, but it does have its shortcomings. The 2T model is not able to capture some nonequilibrium and non-Boltzmann behavior. The presented work extends the understanding of these aspects for oxygen containing flows. Detailed STS, master equation analysis is used to evaluate the limitations of the 2T model and to suggest a modification to capture additional effects of nonequilibrium and non-Boltzmann behavior that is present in the detailed analysis. Quasi-classical trajectory (QCT) and forced harmonic oscillator (FHO) rates were used for the O_2-O and O_2-O_2 systems, respectively.

The STS analysis allowed for the development of high fidelity macroscopic vibrational-translational (VT) transfer rates and total dissociation rates under nonequilibrium and non-Boltzmann conditions. This level of detail about rates is difficult, if not impossible, to capture through experimental study using shock tubes. The detailed

information of these nonequilibrium and non-Boltzmann effects allowed for development of the 2T-NENB model. Overall, the total dissociation rates are influenced more by these factors than the VT energy transfer. This is reflected in the model details. Specifically, the VT energy transfer adopted the QCT based function for the relaxation parameter. The 2T model already accounts properly for nonequilibrium and required only a small modification factor for non-Boltzmann effects in the 2T-NENB variant. The total dissociation rate utilizes a linear combination of translational and vibrational temperatures as a control temperature to account properly for nonequilibrium effects. Additionally, a scale parameter is introduced to account for non-Boltzmann effects.

In addition to the vibrational relaxation and dissociation rates, the vibrational energy loss due dissociation was evaluated. The widely used 2T model assumes that this energy is a constant value that takes the form of a fraction of the dissociation energy. The model generally assumes 0.45 of the dissociation energy. The STS rates allowed for a temperature dependent form of the vibrational energy loss to be studied. The temperature dependent form showed no appreciable change in the shock tube investigation simulations. The investigation focused on oxygen compositions for flow conditions that are representative of those that will be experienced by sustained flight, hypersonic vehicles. This is a notable finding since the vibrational energy loss due to dissociation is one of the main aspects of the 2T modeling approach.

Shock tube flow and double cone experimental data were used to evaluate the models for accuracy. The shock tube results show that the 2T-NENB model is able to improve on the deficiencies observed in the standard 2T model. The simple modification terms are able to account for nonequilibrium more precisely and account for the impact of non-Boltzmann distributions. The double cone analyses show some discrepancies between the various models and the experimental surface data. This difference suggests that further investigation is needed in the near wall behavior of

nonequilibrium CFD and perhaps the determination of the freestream conditions of the experiments.

One of the main motivations for this work was to reduce the design margin associated with the nonequilibrium modeling uncertainty. Through the use of STS modeling and a proposed modification to the 2T model, the agreement between the simulation results and experimental data has been improved, and qualitatively the uncertainty associated with the nonequilibrium modeling of oxygen has been reduced.

6.2 Unique Contributions

The work presented in this dissertation advances the understanding of thermochemical nonequilibrium modeling for oxygen flows. The work captures a large range of fidelity for thermochemical, nonequilibrium modeling. The investigation of the various models allows assessment of fidelity requirements and allows reduced order model development. The list below summarizes the contributions of the work presented in this dissertation.

- Comprehensive evaluation of 2T and STS nonequilibrium modeling approaches for oxygen flows.
- High fidelity STS analysis was performed for an oxygen flow with newly available rates from QCT analysis.
- 2T and STS results were compared to experimental measurements for oxygen flows to assess modeling accuracy across a range of hypersonic conditions.
- A modification to the 2T model, based on detailed STS rate information, was developed to have the computational cost of the 2T model while having accuracy similar to the STS analysis.

- A 3D, finite volume CFD solver with STS modeling capability was developed and can be used as a testbed for numerical method improvements or for performance comparisons to future reduced order models.

6.3 Future Work

Future work should focus on reducing computation cost of accurate nonequilibrium simulations. First, numerical methods can be improved for the STS CFD simulations. The STS system of master equations is very stiff compared to the system of flow equations. This provides an opportunity to decouple the portions of the overall system and solve them by different methods in order to reduce the computational expense. Previous work [41] has utilized Strang operator splitting to separate the flow and master equation portions of the system. This method does split operations, however, it is a general splitting methodology. It would be worth pursuing a more specific methodology that takes advantage of the specific physics of nonequilibrium flow. For example, the time spent on each operation could be weighted by the ratio of time scales between flow and thermochemical behavior. This would make the solution scheme as efficient as possible. Second, a formal uncertainty quantification (UQ) study should be conducted for a number of the modeling aspects. Specifically, UQ for the STS rates, 2T model coefficients, and experimental conditions would be informative. The results would help direct the focus of future work in simulation and experimentation, and the results could guide any reduce-order model developments. Third, the STS work in this thesis is utilizing all energy states when modeling the vibrational mode. The large number of equations (45) that result from this lead to the high computational cost of the STS CFD simulations. The thesis work has shown that there is a universal-like behavior in the evolution of the vibrational population distribution with the over and under populated tail behavior. This universal-like behavior would lend itself well to a reduced order representation of the vibrational

population distribution. The representation would need to have enough degrees of freedom to mimic the behavior observed in the distribution evolutions in this thesis work. It appears that potentially a representation with 5 degrees of freedom could do a good job. Other research groups such as [30] have made similar attempts. However, most attempts have used a representation that is general (in the sense of capturing any possible distribution). The suggestion from this thesis work would be to limit the representation capability to distribution shapes that occur in under practical flow conditions. This could limit the application of the method, however it has great potential to reduce the computational cost for hypersonic vehicle design work. Next, the reduced order model presented in this dissertation was restricted to being a simple modification within the standard, 2T modeling framework. The modification performed well and shows promise, but there is an opportunity to make the method more general and better performing by introducing more complexity to better represent the detailed physics in the thermochemical behavior. Fourth, there is a need for more high quality experimental data. Specifically, there is almost no experimental data for stronger nonequilibrium conditions containing oxygen. New data would allow further refinement of numerical models and push our understand of the limitations of the models. Finally, a natural extension of the work presented in this thesis is to apply the methodology to different species pairs. Pairs such as $O_2 - N$, $O_2 - N_2$, and $O_2 - NO$ would complete the understanding of the major interacting pairs for the two main constituents of air. Additionally, the work for oxygen should be extended into the two low-lying electronically excited states of oxygen. The work presented has neglected these electronically excited states, however, they will be present in the stronger hypersonic flight conditions. Further work will be needed to understand the influence they will have.

APPENDICES

APPENDIX A

Vibrational Energy Levels

Vibrational Level / Varandas Energy / Dunham Expansion Energy

0 786.0234 787.38

1 2343.573 2343.76

2 3881.3038 3876.57

3 5398.5964 5386.03

4 6894.8782 6872.33

5 8369.5118 8335.65

6 9822.0457 9776.10

7 11251.754 11193.80

8 12658.072 12588.81

9 14040.4352 13961.17

10 15398.3596 15310.90

11 16731.2 16637.96

12 18038.3111 17942.32

13 19319.2091 19223.89

14 20573.1679 20482.55

15 21799.7037 21718.17

16 22998.2518 22930.57

17 24168.0058 24119.55

18 25308.4816 25284.86

19 26419.0341 26426.26

20 27498.9373 27543.43

21 28547.546 28636.06

22 29564.2148 29703.79

23 30548.1374 30746.23

24 31498.6683 31762.96

25 32414.9205 32753.54

26 33296.168 33717.48

27 34141.6041 34654.28

28 34950.3419 35563.40

29 35721.3326 36444.26

30 36453.8504 37296.26

31 37146.6854 38118.78

32 37798.8698 38911.14

33 38409.2744 39672.67

34 38976.5281 40402.62

35 39499.5822 41100.26

36 39976.9044 41764.79

37 40407.0429

38 40788.6264

39 41119.9613

40 41399.6763

41 41626.4003

42 41799.6494

43 41920.3914

44 41993.5464

45 42029.6803

46 42042.9885

BIBLIOGRAPHY

BIBLIOGRAPHY

[1] Michael S Holden, Timothy P Wadhams, and Matthew MacLean. A review of experimental studies with the double cone and hollow cylinder/flare configurations in the lens hypervelocity tunnels and comparisons with navier-stokes and dsmc computations. 48th AIAA Aerospace Sciences Meeting, AIAA paper 2010-1281, Jan 2010.

[2] Chul Park. *Nonequilibrium hypersonic aerothermodynamics*. Wiley, 1989.

[3] Roger C Millikan and Donald R White. Systematics of vibrational relaxation. *Journal of Chemical Physics*, 39(12):3209–3213, 1963.

[4] JE Breen, RB Quy, and GP Glass. Vibrational relaxation of O_2 in the presence of atomic oxygen. *Journal of Chemical Physics*, 59(1):556–557, 1973.

[5] John H Kiefer and Robert W Lutz. The effect of oxygen atoms on the vibrational relaxation of oxygen. In *Symposium (International) on Combustion*, volume 11, pages 67–76. Elsevier, 1967.

[6] Chul Park. Review of chemical-kinetic problems of future nasa missions: I - earth entries. *Journal of Thermophysics and Heat Transfer*, 7(3):385–398, 1993.

[7] D A Andrienko and I A Boyd. Rovibrational energy transfer and dissociation in O_2-O collisions. *Journal of Chemical Physics*, 144:104301, 2016.

[8] Marco Panesi, Richard L Jaffe, David W Schwenke, and Thierry E Magin. Rovibrational internal energy transfer and dissociation of $N_2(^1\Sigma_g^+)$- $N(^4S_u)$ system in hypersonic flows. *Journal of Chemical Physics*, 138(4):044312, 2013.

[9] Paolo Valentini, Thomas E Schwartzentruber, Jason D Bender, Ioannis Nompelis, and Graham V Candler. Direct simulation of rovibrational excitation and dissociation in molecular nitrogen using an ab initio potential energy surface. 45th AIAA Thermophysics Conference, AIAA Paper 2015-474, June, 2015.

[10] Marat Kulakhmetov, Michael Gallis, and Alina Alexeenko. Effect of O_2+O *ab initio* and morse additive pairwise potentials on dissociation and relaxation rates for nonequilibrium flow calculations. *Physics of Fluids (1994-present)*, 27(8):087104, 2015.

[11] Jae Gang Kim and Iain D Boyd. State-resolved master equation analysis of thermochemical nonequilibrium of nitrogen. *Chemical Physics*, 415:237–246, 2013.

[12] M Capitelli, G Colonna, and F Esposito. On the coupling of vibrational relaxation with the dissociation-recombination kinetics: From dynamics to aerospace applications. *The Journal of Physical Chemistry A*, 108(41):8930–8934, 2004.

[13] EV Kustova, EA Nagnibeda, and AH Chauvin. State-to-state nonequilibrium reaction rates. *Chemical Physics*, 248(2):221–232, 1999.

[14] Bellucci V. Colonna G. Capitelli M. Armenise I. Giordano, D. and C. Bruno. Vibrational relaxing flow of n2 past an infinite cylinder. *Journal of Thermophysics and Heat Transfer*, 11(1):27–35, 1997.

[15] Tuttafesta M. Capitelli M. Colonna, G. and D. Giordano. Non-arrhenius no formation rate in one-dimensional nozzle airflow. *Journal of Thermophysics and Heat Transfer*, 13(3):372–375, 1999.

[16] Pietanza L. Colonna, G. and G. d'Ammando. Self-consistent collisional-radiative model for hydrogen atoms: atom-atom interaction and radiation transport. *Chemical Physics*, 398:37–45, 2012.

[17] Igor V Adamovich, Sergey O MacHeret, J William Rich, and Charles E Treanor. Vibrational energy transfer rates using a forced harmonic oscillator model. *Journal of Thermophysics and Heat Transfer*, 12(1):57–65, 1998.

[18] Kevin Neitzel, Jae Gang Kim, and Iain D Boyd. Nonequilibrium modeling of oxygen in reflected shock tube flows. *AIAA Paper*, 2961:2014, 2014.

[19] Donald G Truhlar and James T Muckerman. Reactive scattering cross sections iii: quasiclassical and semiclassical methods. In *Atom-Molecule Collision Theory*, pages 505–566. Springer, 1979.

[20] C. Vincenti. W., Kruger. *Introduction to Physical Gas Dynamicse*. Wiley, 1967.

[21] Fabrizio Esposito and Mario Capitelli. The relaxation of vibrationally excited O_2 molecules by atomic oxygen. *Chemical Physics Letters*, 443(4):222–226, 2007.

[22] F Esposito, M Capitelli, and C Gorse. Quasi-classical dynamics and vibrational kinetics of $N+N_2(v)$ system. *Chemical Physics*, 257(2):193–202, 2000.

[23] Daniil A Andrienko and Iain D Boyd. High fidelity modeling of thermal relaxation and dissociation of oxygen. *Physics of Fluids (1994-present)*, 27(11):116101, 2015.

[24] Derek Steele, Ellis R Lippincott, and Joseph T Vanderslice. Comparative study of empirical internuclear potential functions. *Reviews of Modern Physics*, 34(2):239, 1962.

[25] A.J.C. Varandas and A.A.C.C. Pais. A realistic double many-body expansion (DMBE) potential energy surface for ground-state O_3 from a multiproperty fit to ab initio calculations, and to experimental spectroscopic, inelastic scattering,

and kinetic isotope thermal rate data. *Molecular Physics*, 65(4):843–860, Nov 1988.

[26] Daniil A Andrienko and Iain D Boyd. Master equation study of vibrational and rotational relaxation of oxygen. 45th AIAA Thermophysics Conference, AIAA Paper 2015-3252, June, 2015.

[27] MH Bortner. A review of rate constants of selected reactions of interest in re-entry flow fields in the atmosphere. tech. Technical report, Note 484, Nat. Bur. Standards, US Dep. Com, 1969.

[28] Kevin Neitzel, Jae Gang Kim, and Iain D Boyd. Nonequilibrium modeling of oxygen in reflected shock tube flows. In *11th AIAA/ASME Joint Thermophysics and Heat Transfer Conference*. AIAA paper 2014-2961, June 2014.

[29] Kevin Neitzel, D. Andrienko, and Iain D Boyd. Modeling fidelity for oxygen nonequilibrium thermochemistry in reflected shock tube flows. In *46th AIAA Thermophysics Conference*. AIAA paper 2015-2509, June 2015.

[30] Lino da Silva M. Lopez, B. Non-boltzmann analysis of hypersonic air re-entry flows. In *11th AIAA/ASME Joint Thermophysics and Heat Transfer Conference*. AIAA paper 2014-2961, June 2014.

[31] K. Fujita. Influences of molecular rotation on vibrational kinetics and dissociation of n2. In *48th AIAA Aerospace Sciences Meeting*. AIAA paper 2010-1568, January 2010.

[32] K. Owen. Measurements of vibrational relaxation and dissociation of oxygen with laser absorption spectroscopy with applications for energy transfer in nonequilibrium air. *Master's Thesis*, 2014.

[33] Kuznetsova LA Bykova, NG. Study of the absorption characteristics of molecular oxygen in the schumann-runge system at high temperatures: I. calculations of absorption spectra. *Optics and Spectroscopy*, 105(5):668–673, 2008.

[34] C. Park. Two-temperature interpretation of dissociation rate data for n2 and o2. *AIAA Aerospace Sciences Meeting*, AIAA-88-0458, 1988.

[35] LB Ibraguimova, AL Sergievskaya, V Yu Levashov, OP Shatalov, Yu V Tunik, and IE Zabelinskii. Investigation of oxygen dissociation and vibrational relaxation at temperatures 4000–10 800 k. *Journal of Chemical Physics*, 139(3):034317, 2013.

[36] LB Ibraguimova, AL Sergievskaya, and OP Shatalov. Dissociation rate constants for oxygen at temperatures up to 11000 K. *Fluid Dynamics*, 48(4):550–555, 2013.

[37] Chul Park. Hypersonic aerothermodynamics. *International Journal of Aeronautical and Space Sciences*, 14(1):1–10, 2013.

[38] NA Generalov and SA Losev. Vibrational exitation and decomposition of molecular oxygen and carbon dioxide behind shock waves. *Journal of Quantum Spectroscopy and Radiative Transfer*, 6:101–125, 1966.

[39] L. Scalabrin. Numerical simulation of weakly ionized hypersonic flow over reentry capsules. In *Ph.D. Thesis*. University of Michigan, 2007.

[40] Josyula E. Burt, J. Assessment of vibrational nonequilibrium for state resolved simulation of a hypersonic flow. *54th AIAA Aerospace Sciences Meeting*, AIAA Paper 2016-0737, 2016.

[41] Josyula E. Vedula, P. Numerical simulation of hypersonic blunt body and nozzle flows using master equation. *10th AIAA/ASME Joint Thermophysics and Heat Transfer Conference*, AIAA Paper 2010-4331, 2010.

[42] Wadhams T. MacLean M. Dufrene A. Holden, M. Measurements of real gas effects on regions of laminar shock wave/boundary layer interaction in hypervelocity flows for blind code validation studies, AIAA Paper 2013-2837, June 2013.